4D STUDY OF THORACIC CANCER RADIATION TREATMENT

APPROVED BY SUPERVISORY COMMITTEE

Geoffrey Zhang, Ph.D.

Homayoun Hamidian, Ph.D.

Roderick McColl, Ph.D.

Peter Antich, Ph.D.

DEDICATION

I would first like to thank my committee members for their time and their help on various aspects of this research project. Thank you, Dr. Geoffrey Zhang, my advisor, for keeping me on track and for always being there whenever I needed your help. Thank you, Dr. Peter Antich**,** Director of UTSW's BME and RDS Graduate Program, for giving me the great opportunity to be one of the members of the Graduate Program in Radiological Sciences. Thank you, Dr. Roderick McColl, for providing a lot of useful advice relating to image processing fields. And thank you, Dr. Homayoun Hamidian**,** for helping me understand more about radiation physics relating to this project – you are a great teacher.

I would like to offer thanks to everyone else who contributed significantly to this project. Thank you, Dr. Ken Forster, for recruiting me into the Radiation Oncology Department and helping me gain a better understanding of the medical physics field. Thank you, Dr. Tomas Guerrero, for coming up with the idea for some of this dissertation research projects and for constantly striving to make it better. Thank you, Dr. Choy Hake, Chairman of the Radiation Oncology Department, for providing financial support throughout my training. Thank you, Dr. Xiaolin Tu, for all of your encouragement. Thank you, Dr. Frederick Hager, who guided and taught me throughout all of my clinical work. Thanks to Dr. Kwangyoul Park, for all of your help throughout my research and clinical work.

I would also like to thank my classmates and friends, Gang Ren, Peiying Liu, and Yao Ding for all of your help throughout school and in daily life. Your friendship and kindness have truly enriched my life. Last, but not least, I would like to thank my parents for all of your love and support.

4D STUDY OF THORACIC CANCER RADIATION TREATMENT

by

TZUNG-CHI HUANG

DISSERTATION

Presented to the Faculty of the Graduate School of Biomedical Sciences

The University of Texas Southwestern Medical Center at Dallas

In Partial Fulfillment of the Requirements

For the Degree of

DOCTOR OF PHILOSOPHY

The University of Texas Southwestern Medical Center at Dallas

Dallas, Texas

May, 2007

4D STUDY OF THORACIC CANCER RADIATION TREATMENT

Tzung-Chi Huang, Ph.D.

The University of Texas Southwestern Medical Center at Dallas, 2007

Supervising Professor: Geoffrey Zhang, Ph.D.

Respiratory motion causes an added uncertainty in the radiation treatment of thoracic malignancies due to an increase in the normal tissue irradiated and an uncertainty in the radiation coverage of the tumor. This results in a potential increase in complications from treatment and may be insufficient to ensure coverage of the tumor. Reduction of the volume of normal tissue irradiation while maintaining tumor coverage is used to accomplish this goal. The application of 4D CT imaging to radiotherapy treatment planning is an active area of research with the goal to reduce the required normal tissue irradiation and improve the tumor coverage. Deformable image registration holds the key to link the information of two images at various phases. The major purpose of this study is to develop and validate the optical flow method (OFM), a method of deformable image registration by which the image content properties are utilized to generate a displacement vector between each voxel in the reference image to the target image for registration. With OFM, we were able to develop and validate an automated method for intrathoracic motion estimation from breath-hold and 4-D computed tomography imaging;

demonstrate the path integration of a four-dimensional dose distribution onto the 3-D anatomy; develop an automated target delineation technique; and to develop and implement a method to quantify tumor response and normal tissue damage by comparison of pre- and post-treatment and 18F-FDG-PET scans, all of which constitute meaningful applications and represent substantial progress in radiation treatment.

TABLE OF CONTENTS

LIST OF FIGURES

LIST OF TABLES

LIST OF ABBREVIATIONS

3D	Three-dimensional
4D	Four-dimensional
AP	Anterior-Posterior
BH	Breath-hold
CT	Computed Tomography
CTV	Clinical Tumour Volume
DLCO	Diffusion length for carbon monoxide
DRR	Digitally Reconstructed Radiograph
DVH	Dose-Volume Histogram
FB	Free Breathing
FDG	Fluro-deoxy Glucose
FI	Fourier Interpolation
FWTM	Full-Width at Tenth Maximum
GE	Gastro-Esophageal
GTV	Gross Tumour Volume
ICRU	International Commission on Radiation Units
IMRT	Intensity-Modulated Radiation Therapy
ITV	Internal Target Volume
MI	Mutual Information
NCAT	NURBS-Based Cardiac-Torso
NSCLC	Non-Small-Cell Lung Cancer
NURBS	Non-Uniform Rational B-splines
OFM	Optical Flow Method
PA	Posterior- Anterior
PET	Positron Emission Tomography
PFT	Pulmonary Function Testing
QA	Quality Assurance
RMS	Root Mean Square
ROI	Region Of Interest

RPC	Radiological Physics Center
SI	Superior-Inferior
SPECT	Single Photon Emission Computed Tomography
SUV	Standard Uptake Value
TLD	Thermo-Luminescent Dosimetry
TPS	Thin Plate Spline
XRT	Radiation Therapy

1. Introduction

1.1 Overview

The goals of advances in radiation therapy techniques include reduced normal-tissue toxicity and increased tumor control. Improvements in radiation delivery techniques enable clinicians to achieve these goals. According to the The International Commission on Radiation Units (ICRU) and measurements Report 50 (ICRU 1993) and the Supplement Report 62 (ICRU 1999) describe the current recommendation for incorporation of tumour motion into radiation therapy planning. Briefly, the gross tumour volume (GTV) is tumor that is visually apparent on imaging studies; the clinical tumour volume (CTV) is the GTV plus a margin for local microscopic spread of malignant cells; and the internal target volume (ITV) is the CTV plus a margin for intraorgan motion, such as respiratory motion. Incorporating thoracic tumor motion into the planning process requires acquisition and tumor delineation on multiple image volumes.

Measuring intrathoracic tumor motion for ITV determination via imaging techniques has become a new focus of study [1-8]. Four-dimensional (4D) computed tomography (CT) imaging, which is still in development, will generate eight or more CT image volumes to represent the tumor throughout the respiratory cycle [9]. Manual delineation of each of these CT image volumes is laborious and presents a risk of error. Significant inter-observer and intra-observer variations in tumor CT segmentation have been observed [10, 11] when manual segmentation is applied repeatedly to the same subject CT image set. Finally, tumor-surface delineation does not provide a point-to-point correspondence between tumor volume elements at

expiration and at inspiration. Instead, only an approximation of the boundary of the tumour is obtained with manual delineation techniques. The bounding box provides a minimal description of surface shape changes and does not track the actual tumour surface or volume elements.

Radiological imaging is used in almost every step of radiation treatment, including pre-treatment staging, radiotherapy treatment planning, and post-treatment restaging or follow-up evaluations. Each image depicts unique spatial or functional information including malignancy position, treatment volume, radiation dose distribution, residual tumor resulting following treatment, and spatial distribution of radiological-evident complications, which are all meaningful references for physicians. However, no reliable quantitative means of linking such information between imaging sessions and between imaging modalities are available. Accessing the correlative spatial and biological information contained in the staging imaging study is valuable for tumor localization during treatment planning. An accurate automated registration process is needed that will reduce variability in patient setup, scanners, and image acquisition parameters.

The goal of deformable image registration is to find a point-to-point voxel correspondence between two given images. This desired correspondence should describe the location of each voxel in the first image relative to the second image. The optical flow method (OFM) [12] finds such a correspondence by computing a displacement field describing the apparent motion depicted in the two images. In its presented study, 3D OFM registers the full-resolution CT image volumes allowing anatomic structures to be mapped between CT volumes.

A new computed tomography (CT) imaging technology is emerging that acquires a CT movie sequence of the chest to capture respiratory motion. This process is referred to as 4D CT. This new CT imaging results in a 3D movie loop representing

the motion of one inhale/exhale breath cycle. 4D CT imaging may produce 8 or 16 image volumes. Physicians are required to manually delineate the tumor and normal structures (such as the heart and spinal cord) on each of the separate image volumes, greatly increasing the clinician workload and risk of error. Utilization of the 4D CT image set for radiotherapy treatment planning requires calculation of the radiation dose for each of the 8 to 16 image volumes. However, there is currently no reliable means of mapping the significant contours delineated by the physician to another image volume and of adding the individual doses into a single tissue dose estimate.

One advantage of OFM is that the image content properties are used to generate a displacement vector between each voxel in the reference image to the target image. The displacement vector map obtained for each voxel in a CT image volume is used to map delineated tumors or organs from one CT image volume to the next on a point-by-point basis. The boundary of the mapped tumor or organ volumes represents the new tumor or organ contour on the target CT images. Alternatively, the surface points of tumor or organs can be mapped. This paradigm can be applied to pairs of breath-hold (BH) CT image volumes or potentially to a complete 4D CT image set equally well. With OFM methodology, the tumor or organ target is manually delineated on a reference CT image volume, and both the surface and contained volume are mapped to the additional CT volumes. The collection of displacement vectors for the surface or volume represents the motion of the tumor or organs.

In addition, an automated deformable image registration method is needed that will register each of the multiple image volumes without user intervention. In the present study, the integration of imaging studies that cancer patients currently receive coupled with deformable image registration techniques allows for the extraction of new information relevant to the individual patient and to our understanding of cancer treatment. One advantage is that patient information can be retrieved retroactively

from existing imaging databases and this method can be applied and new questions addressed. These same techniques, once developed, can be applied to the development of 4D radiation treatment planning.

This study seeks to develop a new method not only to estimate the inside body motion in CT image during the respiration, but also to assess tumor response to therapy by looking inside the tumor to identify those regions that appear to shrink less and may represent the sites of local failure. Deformable image registration holds the key for the use of multiple CT image volumes acquired across time, to represent breathing or a series of pre- and post-treatment imaging. Integration of the many imaging studies that lung cancer patients receive before, during, and after cancer treatment with deformable image registration will improve tumor targeting while minimizing clinically significant damage to normal tissues. We seek to develop the techniques, methodology, and software to use 4D radiological imaging data effectively in lung cancer treatment and follow-up.

1.2 Objectives

The goal of the research presented in this dissertation is to investigate the use of three dimension deformable image registration as a basis for radiation treatment. We implement the 3D deformable image registration tool based on optical flow method (OFM). The optical flow method can be used to study the elastic image mapping, radiation dose mapping across the CT image, image registration and image segmentation which will potentially provide a substantial contribution to improve radiation treatment today. We hypothesize that 3D OFM will provide the reliable quantitative means of linking such information between imaging sessions and between imaging modalities. We believe that that this deformable image registration method will provide a powerful tool for use in registration studies in medical image

research, especially for respiratory motion. Lung tumor control in radiation treatment can be improved and treatment complications can be reduced by fixing precise tumor position and integrating obtainable information from different imaging modalities with deformable image registration. In the first part of this study, we will develop the 3D deformable image registration tool based on OFM. Then we will test the hypothesis by using NURBS-based cardiac-torso (NCAT) digital phantom, physical measurements and other deformable image models. The following specific objectives for this work were established:

Aim 1: To implement and demonstrate 3D deformable image registration, 3D optical flow algorithm. This provides an accurate image registration tool which is able to connect images acquired at different time (phases), (e.g., 4D CT). For validation purposes, the 3D OFM performance was applied to phantom and computer generated cases (digital phantom) where the exact tumor motion was known for comparison.

Aim 2: To develop an automated target delineation technique (for tumor or organs). This technique will provide an excellent tool for drawing and mapping the contour automatically for physician and dosimetrist. It will help physician and dosimetrist minimize error and reduce clinical work loads.

Aim 3: To develop a novel technique to estimate tumor and organ motion. We provide a means to measure intrathoracic tumor motion from inspiration/expiration breath-hold (BH) CT image sets, mapping the physician-drawn tumor contours from inhalation to the exhalation CT image set, automated target delineation technique.

Aim 4: To develop a method for quantifying tumor response and normal tissue damage by comparison of pre- and post-treatment and 18F-FDG-PET scans. We will employ deformable image registration to correlate the radiotherapy treatment planning dose distribution with the post-treatment PET/CT image volume, which will

facilitate investigations of treatment complications, disease persistence, and disease recurrence.

Aim 5: To develop a technique for radiation dose mapping and estimation. This provides a way to estimate the dose distribution in different phases by registering the 4D CT imaging. The way to calculate 4D dose accumulation will be accomplished through image registration by OFM.

1.3 Organization

The work completed toward accomplishing each of the specific aims in this dissertation is presented as follows. Chapter 2 begins by describing the primary method – optical flow method (OFM) -- and several simulation tools that we use to validate OFM in this dissertation such as NURBS-based cardiac-torso (NCAT) digital phantom, thin-plate spline (TPS) image wrapping method and Radiological Physics Center (RPC) thoracic phantom. Chapter 2 also describes the cost functions, including mutual information (MI), correlation coefficient and root mean square (RMS) error used for validation purposes.

In chapter 3, we demonstrate the path integration of a four-dimensional (4-D) dose distribution onto the 3-D anatomy. Materials and Methods: A computer-generated 4-D thoracic phantom with a lung tumor was constructed. Eight respiratory phases were generated. A radiotherapy treatment plan was applied to all phases resulting in a 4-D dose distribution. An elastic image registration algorithm was used to determine the vector displacement between all of the image elements and the end expiration phase. The path-integrated tissue dose distribution and each component dose distribution were compared with the planned dose distribution. Results: Numerical path integration was performed to calculate the tissue dose distribution. Loss of tumor coverage was the predominant effect observed with tumor

motion in this study. The loss was asymmetric and dependent on the tumor trajectory. Conclusion: The elastic image registration allowed an accurate path integration through a 4-D data set to produce an accurate 3-D tissue dose estimate.

Chapter 4 will focus on demonstration through measurements that optical flow method (OFM) is accurate and practical in 4D dose calculations. Dose deliveries to phantoms that were in motion were compared with OF calculations. The dose distribution in a thoracic phantom recorded by film reasonably agreed with the 3D OF calculation. Agreement was also achieved between the point-dose measurements by an ion-chamber and OF calculations.

In chapter 5, we demonstrate proof-of-concept for the use of deformable image registration to align the radiotherapy treatment-planning dose distribution with the post-treatment PET/CT image volume. Three cases in which the patients had thoracic malignancies are presented. Each patient had CT-based treatment planning for radiotherapy and restaging fluro-deoxy glucose (FDG)-PET/CT imaging 4 to 6 weeks after completion of treatment. The treatment planning or radiation therapy (XRT) CT was registered with the CT images from the PET/CT resulting in a deformation matrix to link the planned radiotherapy dose with the restaging CT and PET images. The dose distribution from the treatment plan was mapped onto the restaging PET/CT using the deformation map. Areas of pneumonitis and recurrence were identified radiographically on both the FDG PET and the CT restaging images. Local dose and standard uptake values for pneumonitis and recurrence were studied.

Chapter 6 describes the use of semi-automated segmentation of CT images. A few high curvature points were manually drawn on a CT slice. Fourier interpolation was then used to complete the contour. Consequently, OF -- a deformable image registration method -- was used to map the original contour to the other slices. This technique was applied successfully to contour anatomical structures and tumors.

Chapters 7 and 8 include organ and tumor contours mapping for real patient CT data sets, and for a thoracic phantom in which the displacement for each voxel is known. In addition, an automated method for intrathoracic tumor motion estimation from breath-hold (BH) CT imaging using 3D OFM is proposed.

2. Methods and Validations

2.1 Optical Flow Theory

Optical flow [12], the vector field, arises from the relative motion between observer and object in the surrounding space. Being demonstrated, optical flow virtually can provide useful information about motion structure of the objects and spatial arrangement. Actually, optical flow algorithms effectively estimate the motion fields. Optical flow is one of the methods used in deformable image registration. This method registers images based on the image content properties and provides outputs of voxel-to-voxel displacement vectors, or velocity matrix.

The optical flow algorithm differs from other methods of image deformable registration by its ease of use and precision in mapping structures of interest. There is no user intervention required to select matching control points and the entire image volume is mapped in one step.

Many different optical flow algorithms have been described in other studies, including intensity gradient based methods, frequency based methods, correlation based methods, etc.

The classical intensity gradient based methods calculate image deformation from the spatial derivatives of image intensities. It requires that the image domain be continuous in space and time (differentiable). Usually, a smoothness constraint is needed to compute optical flow over large regions.

The frequency based methods calculate optical flow in the Fourier domain. One advantage of these methods is that they can calculate motions in images that are difficult for intensity gradient based methods to calculate, such as the motion of

random dot patterns. Typically, frequency based optical flow methods do not have the ability to provide intervals to the calculated velocities. They can only determine whether a velocity is found at a specific location.

The correlation based methods use feature matching to calculate optical flow. These methods may work fine with images of poor signal-to-noise ratio while gradient or frequency based methods may have problems. These methods usually require matching features in images to perform the optical flow calculations. But most features in images are usually easy to mismatch. Thus the accuracy of these methods is usually poorer than the accuracy of gradient and frequency based methods.

For spatiotemporal energy-based methods, translation of the motion in the space-time plane to the frequency plane is completed; and analysis of the location of the maximum energy in frequency planes is then applied to compute the optical flow.

Besides the fundamental methods described above, some optical flow programs use additional techniques to overcome specific problems. For example, all three fundamental methods have problems with occlusion and transparency. Binary line processes have been implemented to model intensity discontinuities, which are classified as multiple motion methods. To improve the accuracy of optical flow calculations, temporal refinement methods have been developed in which the optical flow calculation is performed not only on one pair of images but on the integration over time basis.

2.1.1 Optical Flow Computation

Consistent with most motion estimation algorithms based on image intensities, the basic assumption in this 3D optical flow algorithm is that the intensity of any infinitesimal volume changes little with time, indicating that the material is incompressible. This is expressed mathematically as [12],

$$f\left(x+dx, y+dy, z+dz, t+dt\right) = f\left(x, y, z, t\right) \tag{2.1}$$

where *f(x,y,z,t)* denotes the image intensity at a point *(x,y,z)* at time *t*. Expanding the left hand side in a Taylor series

$$\begin{aligned} & f\left(x+dx, y+dy, z+dz, t+dt\right) \\ & = f\left(x, y, z, t\right) + \\ & \frac{\partial f\left(x, y, z, t\right)}{\partial x} dx + \frac{\partial f\left(x, y, z, t\right)}{\partial y} dy + \frac{\partial f\left(x, y, z, t\right)}{\partial z} dz + \\ & \frac{\partial f\left(x, y, z, t\right)}{\partial t} dt + \text{higher order terms} \end{aligned} \tag{2.2}$$

and substituting equation(2.1) into (2.2) yields the optical flow equation:

$$\frac{\partial f\left(x, y, z, t\right)}{\partial x} v_x + \frac{\partial f\left(x, y, z, t\right)}{\partial y} v_y + \frac{\partial f\left(x, y, z, t\right)}{\partial z} v_z + \frac{\partial f\left(x, y, z, t\right)}{\partial t} = 0 \tag{2.3}$$

where *Vx = dx/dt, Vy = dy/dt, Vz = dz/dt,* are originally defined as the three components of the velocity that describe the spatial change rate of the voxel with respect to time. They are actually the three components of the spatial displacement of the voxel between the two image sets involved in an optical flow calculation. The optical flow calculation determines these three components for each voxel.

To solve equation (2.3) for the three components of the velocity, Horn & Schunck's velocity smoothness constraint [12] is extended to 3D to minimize the Laplacians of the three components:

$$\begin{aligned} & \left(\frac{\partial v_x}{\partial x}\right)^2 + \left(\frac{\partial v_x}{\partial y}\right)^2 + \left(\frac{\partial v_x}{\partial z}\right)^2 + \left(\frac{\partial v_y}{\partial x}\right)^2 + \left(\frac{\partial v_y}{\partial y}\right)^2 + \left(\frac{\partial v_y}{\partial z}\right)^2 + \\ & \left(\frac{\partial v_z}{\partial x}\right)^2 + \left(\frac{\partial v_z}{\partial y}\right)^2 + \left(\frac{\partial v_z}{\partial z}\right)^2 = \varepsilon_s^2 \end{aligned} \tag{2.4}$$

To allow some intensity variation between images, another non-zero term is introduced:

$$\frac{\partial f\left(x, y, z, t\right)}{\partial x} v_x + \frac{\partial f\left(x, y, z, t\right)}{\partial y} v_y + \frac{\partial f\left(x, y, z, t\right)}{\partial z} v_z + \frac{\partial f\left(x, y, z, t\right)}{\partial t} = \varepsilon_{of} \tag{2.5}$$

The weighted contribution of the errors, ε_{of}^2 and ε_s^2, over the image volume, V, is the total error, ε, to be minimized. Thus, to obtain the velocity solution for each voxel, the quantity

$$\varepsilon = \iiint_V \left[\varepsilon_{of}^2 + \alpha^2 \varepsilon_s^2 \right] dx\ dy\ dz \tag{2.6}$$

where α is interpreted as a weighting factor, is minimized through variation. Applying variational calculus, the three velocity components are calculated using three Gauss-Seidel iterations, the equations for which are as follows:

$$\begin{aligned}
v_x^{(n+1)} &= v_x^{(n)} - \frac{\partial f}{\partial x} \frac{\left(v_x^{(n)} \frac{\partial f}{\partial x} + v_y^{(n)} \frac{\partial f}{\partial y} + v_z^{(n)} \frac{\partial f}{\partial z} + \frac{\partial f}{\partial t} \right)}{\alpha^2 + \left(\frac{\partial f}{\partial x} \right)^2 + \left(\frac{\partial f}{\partial y} \right)^2 + \left(\frac{\partial f}{\partial z} \right)^2} \\
v_y^{(n+1)} &= v_y^{(n)} - \frac{\partial f}{\partial y} \frac{\left(v_x^{(n)} \frac{\partial f}{\partial x} + v_y^{(n)} \frac{\partial f}{\partial y} + v_z^{(n)} \frac{\partial f}{\partial z} + \frac{\partial f}{\partial t} \right)}{\alpha^2 + \left(\frac{\partial f}{\partial x} \right)^2 + \left(\frac{\partial f}{\partial y} \right)^2 + \left(\frac{\partial f}{\partial z} \right)^2} \\
v_z^{(n+1)} &= v_z^{(n)} - \frac{\partial f}{\partial z} \frac{\left(v_x^{(n)} \frac{\partial f}{\partial x} + v_y^{(n)} \frac{\partial f}{\partial y} + v_z^{(n)} \frac{\partial f}{\partial z} + \frac{\partial f}{\partial t} \right)}{\alpha^2 + \left(\frac{\partial f}{\partial x} \right)^2 + \left(\frac{\partial f}{\partial y} \right)^2 + \left(\frac{\partial f}{\partial z} \right)^2}
\end{aligned} \tag{2.7}$$

An optical flow calculation requires input of a source image and a target image. The output from the calculation includes the 3D velocity matrix data file equal to each voxel's displacement and an estimated image to assemble the target image.

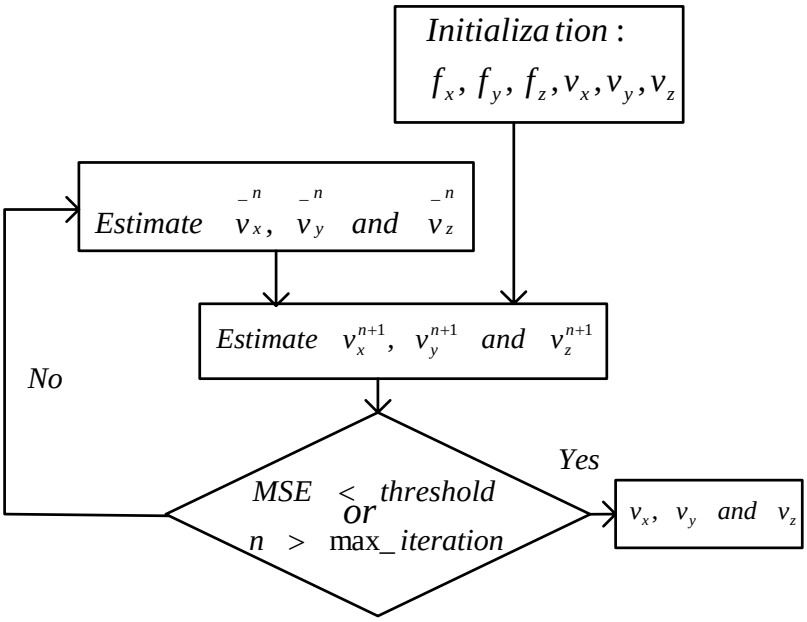

Figure 2.1: The flowchart of basic 3D optical flow method

2.1.2 Iterative-Amendment Feature

The Horn and Schunck method calculates optical flow by iterating the equation in 2.7. However, this original method causes errors in registration if object motion is seriously. Optical flow equations depend on calculating the difference between images and finding the matched images in the next frames. If object movement is large, or if no features overlap between two consecutive images, the Horn and Schunck optical flow method may not produce a reliable velocity flow field.

To correct for this problem, we revised the Horn and Schunck optical flow method with a deformed image, determined by the velocity field estimated from the source image. By this revised method, we could modify features to the covered pattern according to the correct patterns in the next frame. This process would correct some information for motion estimation and help to achieve a suitable velocity field.

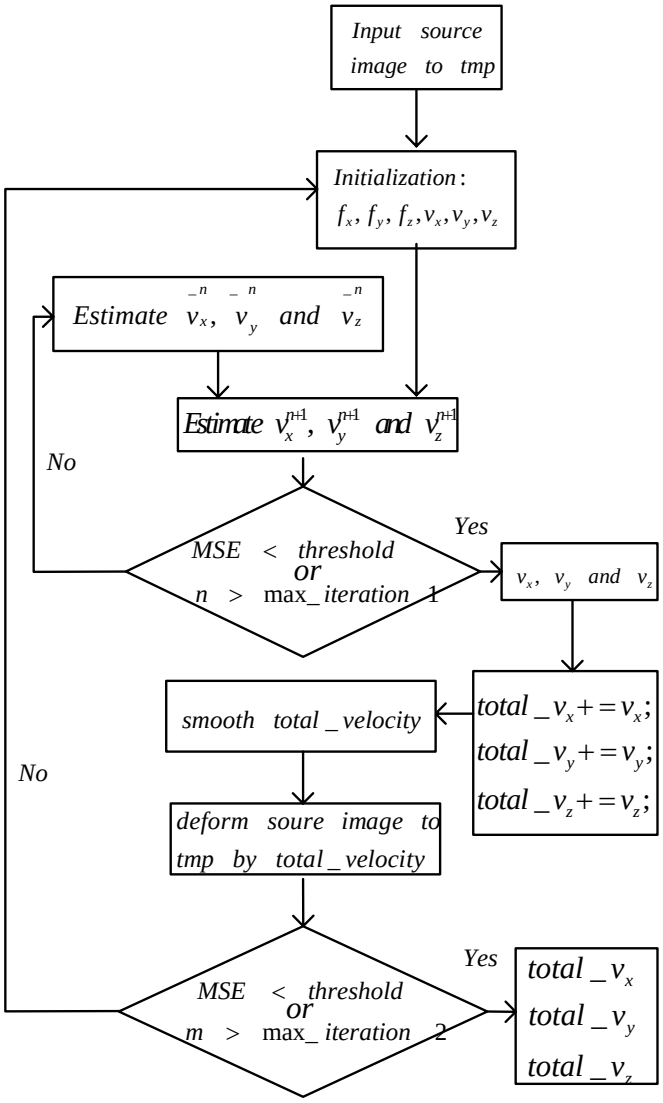

Figure 2.2: The modified flowchart of the 3D optical flow process

2.1.3 Multi-Resolution Feature

Originally, the optical flow method could only handle very small displacements, less than one voxel difference, limiting its applications. This problem was solved by implementing a multi-resolution technique, with larger voxels at lower resolution. The registration starts at a user given resolution level that is a 2 to the *n*th power multiple of the original resolution, and increases hierarchically until the finest resolution is achieved. Figure 2.3 shows the flow chart of the multi-resolution feature.

With the multi-resolution feature, optical flow is more suitable to radiotherapy image registration applications where relatively large image changes may often occur.

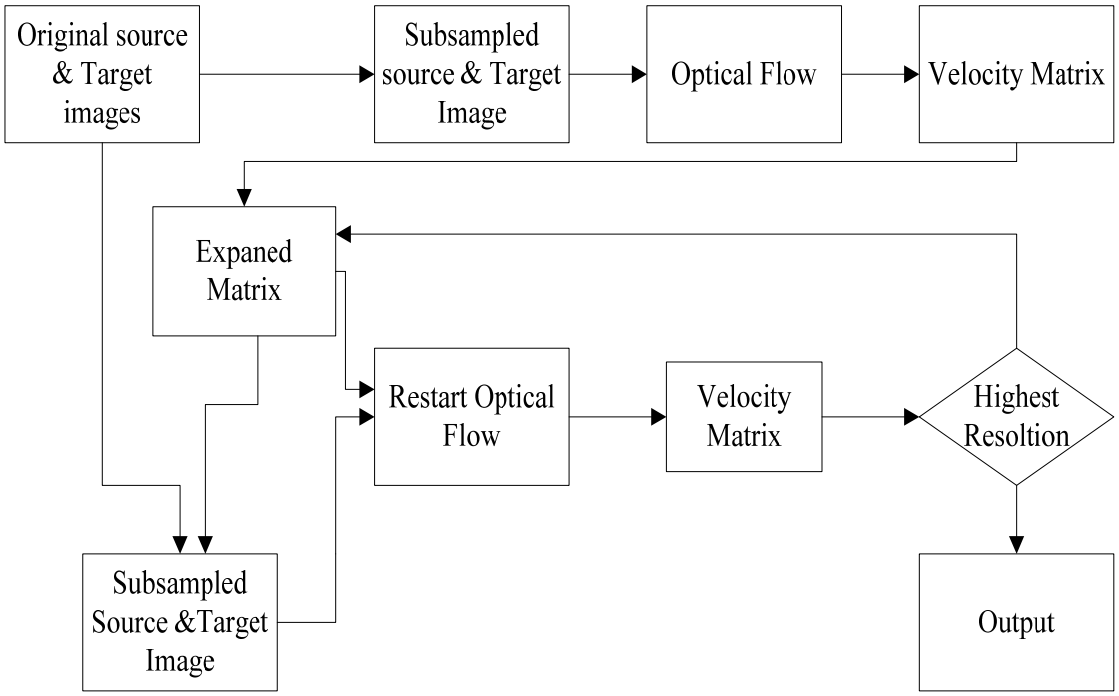

Figure 2.3: Multi-resolution flow chart. In the figure, restart optical flow means starting the registration with the velocity matrix resulted from previous resolution level

2.2 Thin Plate Spline Function

The thin-plate spline (TPS) mapping function can be used to determine a deformation function according to two sets of corresponding control points on the relative images. To apply this function, the matching information of the image spatial distribution can be integrated effectively. In fact, the theorem of TPS is to map the pixel information obtained from image A to another corresponding image B. TPS always matches the corresponding coordinate information exactly, and keeps the entire image's deforming energy to a minimum.

2.2.1 Shape Transformation

A 3D thin-hyper-plate spine algorithm was developed based on our existing 2D version [13, 14] following the outline given by Bookstein [15]. The displacement of the solid volume from the hyper-plane is given by

$$v(x, y, z) = -U(r) = |r| \qquad (1)$$

The function U is a fundamental solution to the tri-harmonic equation of shape for a thin hyper-plate displaced by v(x,y,z) above the (x,y,z)-hyper-plane. The functions U(r) satisfies the equation:

$$\Delta^2 U = \left(\frac{\partial^2}{\partial x^2} + \frac{\partial^2}{\partial y^2} + \frac{\partial^2}{\partial z^2} \right)^2 U \qquad (2)$$

Two sets of coordinates are related through the mapping transformation, where the coefficients are determined by the set of pairs, by the equations:

$$f(x, y, z) = a_1 + a_x x + a_y y + a_z z + \sum_{i=1}^{n} w_i U\left(\left| P_i - (x, y, z) \right| \right) \qquad (3)$$

where $P_i = (x_i, y_i, z_i)$

2.3 NCAT Digital Phantom

The dynamic non-uniform rational b-splines (NURBS)-based cardiac-torso (NCAT) phantom [16] was developed modeling the organ shapes with three-dimensional non-uniform rational b-splines (NURBS) surface using human image data as the basis for the formation of the surfaces. The utility of the NCAT phantom was demonstrated by using it in pilot simulation studies for two different medical imaging modalities, myocardial single photon emission computed tomography (SPECT) and x-ray computed tomography (CT). In fact, the NCAT

phantom can be used to study the development of image acquisition strategies, image processing and reconstruction algorithms and compensation methods. In addition, it can be used to research the effects of anatomical variations and patient motions, such as the beating heart and respiratory motions, on medical images.

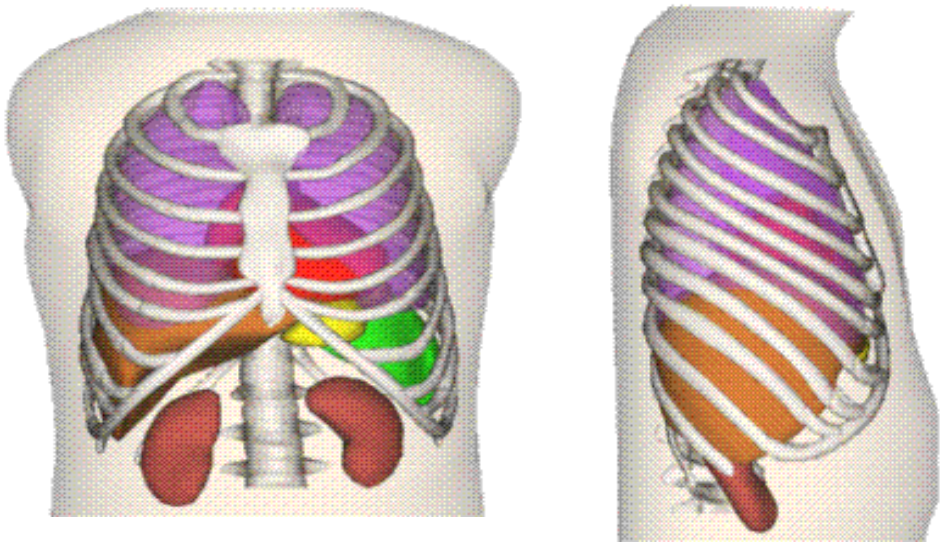

Figure 2.4: NCAT Thoracic Phantom

The 4D NCAT phantom is a computer generated phantom consisting of non-uniform rational b-splines (NURBS) representing a human thorax with realistic anatomy structures modeled from the Visible Human Project dataset. The NCAT software generates a series of simulated CT volume of the thorax at various points of respiration. A voxel-to-voxel map from R^3 to R^3 relates each of the image volumes to the initial reference position. The effects of cardiac and pulmonary motion on imaging and on radiotherapy treatment are readily evaluated with simulations using the NCAT phantom. Both male and female phantoms are available and with modification a tumor can be placed any where in the lungs. A detailed lung geometry with bronchial branching filling the entire lung field is developed. As radiotherapy moves into 4D, this realistic phantom geometry will provide a test frame for developing new

techniques and methods of analysis.

In this study, we use the digital phantom generated from NCAT to calculate the accuracy of dynamic motion estimation by using optical flow method (OFM). As a result of two known velocity matrices from NCAT, we can compare the velocity matrixes estimated by OFM and generated by NCAT.

2.4 Cost Functions

Different cost functions are used to evaluate the quality of optical flow registration in this study. The equation defining the mutual information(MI) index used is given by:

$$MI(U,V) = \sum_{u,v} p_{UV}(u,v) \log \frac{p_{UV}(u,v)}{p_U(u).p_V(v)}$$

where u and v are a pair of features of two objects, of which their marginal probability distributions are $p(u)$, $p(v)$ and joint probability distribution is $p(u,v)$.

The equation defining the correlation coefficient (CC) is:

$$CC = \frac{S_{u,v}}{S_u * S_v} = \frac{\sum_{i=1}^{n} \left(u_i - \bar{u}\right) * \left(v_i - \bar{v}\right)}{\sqrt{\sum_{i=1}^{n} \left(u_i - \bar{u}\right)^2} * \sqrt{\sum_{i=1}^{n} \left(v_i - \bar{v}\right)^2}}$$

where S_u is the standard deviation of object u, S_v is the standard deviation of object v, $S_{u,v}$ is the covariance of object u and v, and r is a correlation coefficient of

u and v with a value between -1 and 1. The RMS error is determined by the following equation:

$$RMS = \sqrt{\frac{\sum_{i=1}^{n}(u_i - v_i)^2}{n}}$$

The CC and RMS errors reflect the linear difference between two images, while mutual information (MI) also includes the non-linear difference in addition to the linear difference. These cost functions evaluate different aspects of registrations.

2.5 Evaluations

2.5.1 Improvements of Adding Iterative and Multi-Resolution Features

In order to increase the accuracy of calculations, iterative solutions of OF were implemented and proven to be effective. A new feature, 3-dimensional multi-resolution registration over coarse-to-fine resolution levels, was implemented for more accurate and efficient OF calculation. In this section we quantitatively analyzed the improvement that the new feature brought to the software for further reference. Since the major barrier to using OF clinically is that OF, and other deformable image registration algorithms, is time consuming in calculation, the recent improvement to our OF software makes an important contribution to clinical practice.

OF calculation, without the multi-resolution feature, usually registers images correctly if differences between the images are small. If the differences are large (> 2 voxels in space), longer computations are required and the risk of errors increases substantially. The multi-resolution approach starts registrations at a coarse resolution level at which the differences are much smaller so that OF can calculate accurately and efficiently. The resulting displacement matrix is then expanded to match the size

of the finer resolution level at which OF continues the registration. The registrations are repeated until the registration for the final resolution level is completed. For CT images, since the slice thickness is usually larger than the slice pixel size, multi-resolution in that direction (z-axis) is usually considered less important. In some particular applications (i.e., treatment evaluation) variations in patient setup result in differences of CT images in the z direction: these values are often larger than those at the slice planes, for which multiple resolution on the z-axis plays a more important role.

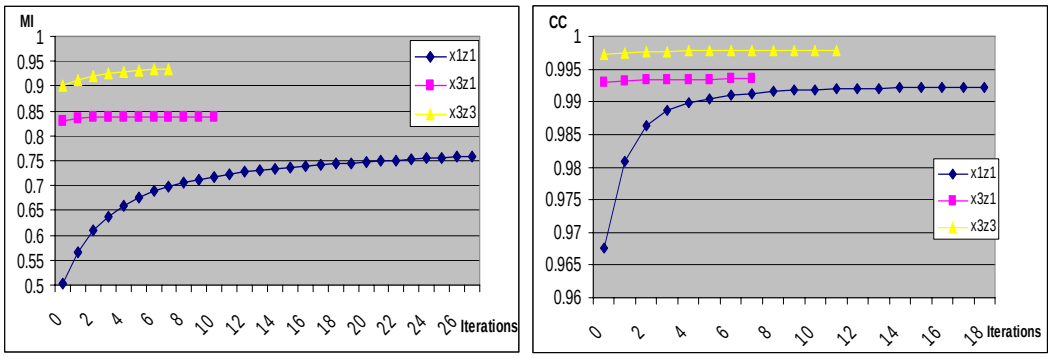

Figure 2.5: 3D multi-resolution curve shows a much better quality. Mutual information was the cost function (left) and CC was used as the cost function (right)

As expected, OF with the 3D multi-resolution feature was 10 times faster in converging accuracy than OF without 3D multi-resolution, and was approximately 2 times faster than 2D multi-resolution. In addition to the temporal benefit, the registration quality was enhanced: 23% better than OF without 3D multi-resolution and 11% better than 2D multi-resolution. MI values were used in evaluating the registration quality. Figure 2.5 shows the comparisons.

2.5.2 Phantom CT Displacement and Validation

A CT image volume of the Radiological Physics Center (RPC) thoracic phantom

[17] was used for validation of the 3D OFM algorithm with known displacements, as shown in figure 2.6. The phantom was displaced 1.2 and 2.4 cm along the *z*-axis producing two target CT volumes. In figure 2.6, the CT image volumes at the origin and at a 2.4 cm displacement are superimposed in coronal and sagittal sections through the tumor. The superior border of the tumor location is indicated by an arrow. The CT voxel sizes were 1 mm × 1 mm × 3 mm. The 3D OFM was applied for both displacements, producing two displacement vector sets. The tumor was outlined, and the displacement of the tumor volume was calculated and compared with the known displacements. The full-width at tenth maximum (FWTM) of the displacement histogram, maximum displacement errors of the 3D OFM calculation and RMS errors were calculated and reported.

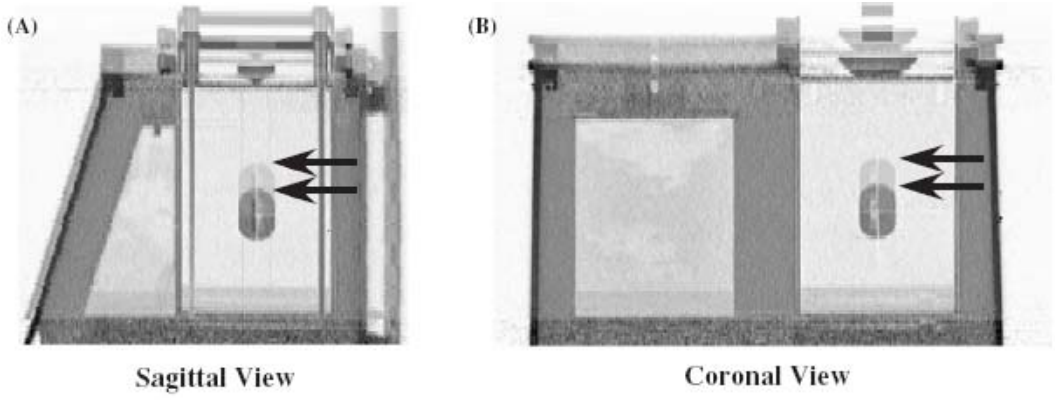

Figure 2.6: (A) Sagittal image of the RPC thoracic phantom shown with double exposure image with the second image displaced 2.4 cm superiorly. Arrow identifies top of simulated tumor on each. (B) Coronal image of the same RPC thoracic phantom shown with double exposure as in (A).

Known displacements of 1.2 and 2.4 cm were applied to the RPC thoracic phantom CT image data. Figure 2.6 shows the 2.4 cm displaced phantom super-imposed over the undisplaced phantom sagittal and coronal sections through the tumor. The superior margins of the tumors are marked by an arrow on the images of both the displaced and undisplaced tumors. The 3D OFM was applied between the

image volumes, and the displacement of each pixel contained in the tumor volume was obtained. A histogram of the displacements is shown in Figure 2.7. The area under each of the two curves equals the tumor volume and is the same for both the 1.2 and 2.4cm displacements. The FWTM of the 1.2 and 2.4cm displacements was 0.008 and 0.006cm, respectively. The maximum error of any single voxel's displacement estimate is 0.11cm or approximately one-third of the *z*-dimension voxel size.

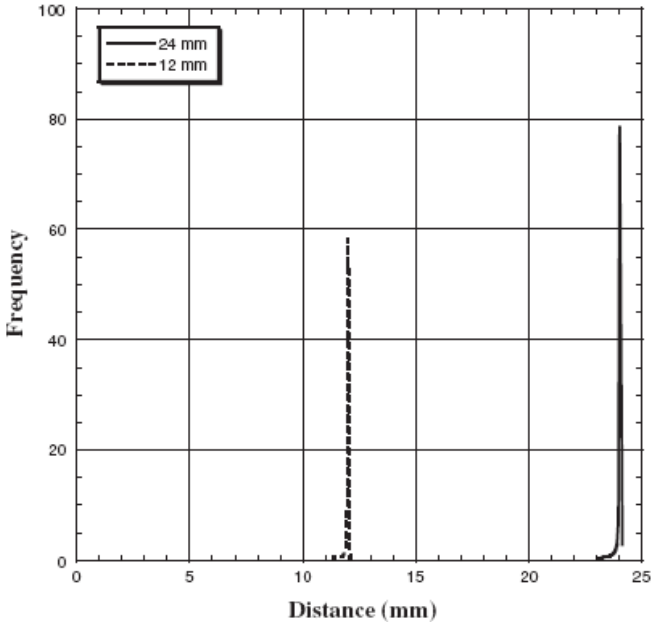

Figure 2.7: Distribution of voxel displacements for simulated tumour with 12 mm and 24 mm superior–inferior displacements.

2.5.3 3D TPS Validation

A previously described thin-plate spline (TPS) algorithm was utilized to generate [13, 15] a fictitious inspiration CT image volume of an entire thorax with a known displacement field from a 3D CT data set. The displacement was modeled from the selection of corresponding points on the measured expiration and inspiration CT image volumes. The expiration CT image set was mapped to the fictitious inspiration image set using 3D OFM. The resulting 3D OFM displacement field was compared

with the known displacement matrix, and the RMS error was calculated. This procedure was performed for one patient with esophageal tumor and for one patient with lung tumor with a displacement of 1.5cm between image sets.

	Oesophagus case	Lung case
X	0.037 mm	0.009 mm
Y	0.009 mm	0.018 mm
Z	0.20 mm	0.036 mm

Table 2.1. The displacement vectors were calculated using 3D OFM between measured expiration CT and TPS generated inspiration CT for an esophagus tumor case and a lung tumor case. The table shows the RMS error of the 3D OFM displacement with respect to the TPS displacement.

A known distortion was applied to the exhalation CT images from one esophageal cancer patient and one lung cancer patient using a 3D TPS algorithm. The process is illustrated in Figure 2.8, where the expiration CT image volume (Figure 2.8A) is deformed following the TPS derived grid (Figure 2.8B) to form the 3D TPS simulated inspiration volume (2.8C). The purpose for the calculation is to produce a pair of image volumes with a known displacement between them. The displacement was modeled from the selection of corresponding points on the exhalation and inhalation CT image volumes. The 3D OFM algorithm was utilized to calculate the displacement between the exhalation scan and the 3D TPS-generated images. The esophagus and lung tumor volumes were manually delineated on the exhalation CT image volume. The resulting displacement of the tumor volume from the exhalation CT to the 3D TPS-generated inhalation CT was found. The displacement was compared with the known displacement between the image volumes. The RMS error for each of the component displacements was calculated from the known 3D TPS displacement field and the 3D OFM derived displacements.

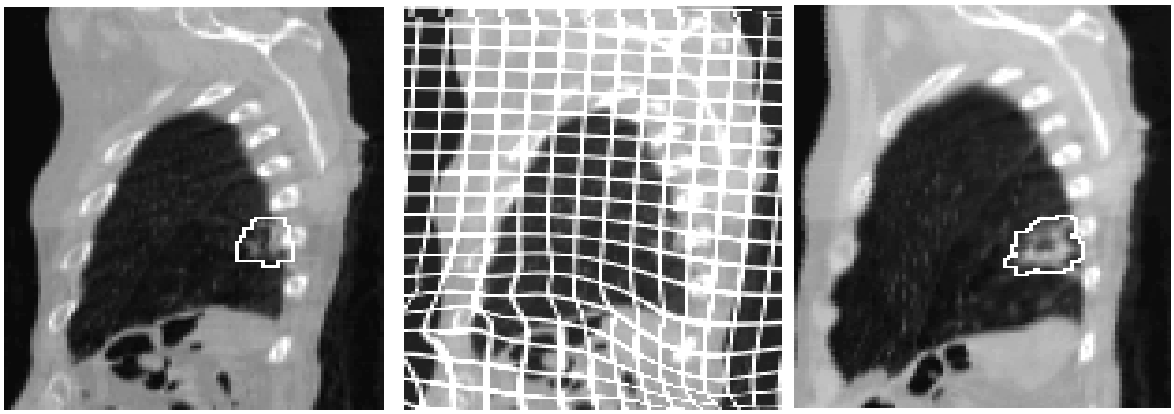

(A) (B) (C)

Figure 2.8: (A) Sagittal expiration CT image of the esophageal tumor with the physician-contoured tumor outline. (B) Same sagittal slice now with the TPS algorithm-calculated deformation grid simulating inspiration CT superimposed. (C) Simulated inspiration CT calculated from the sagittal image in (A) using the deformation grid in (B).

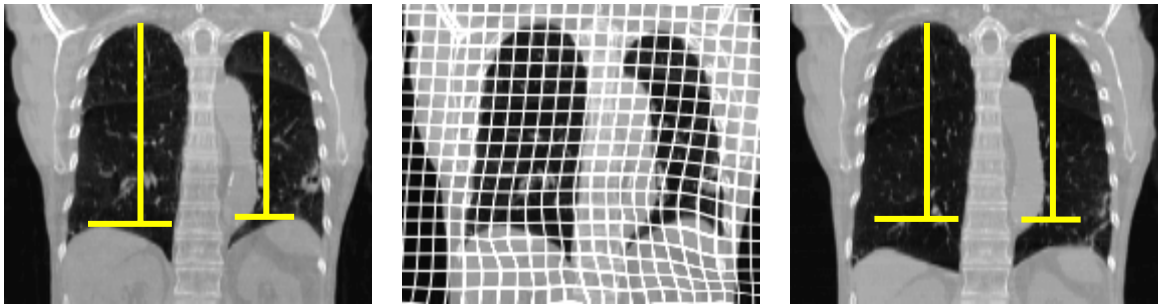

(A) (B) (C)

Figure 2.9: Diaphragm motion (a), tumor distortion and 3D motion (b), and chest wall motion (c).

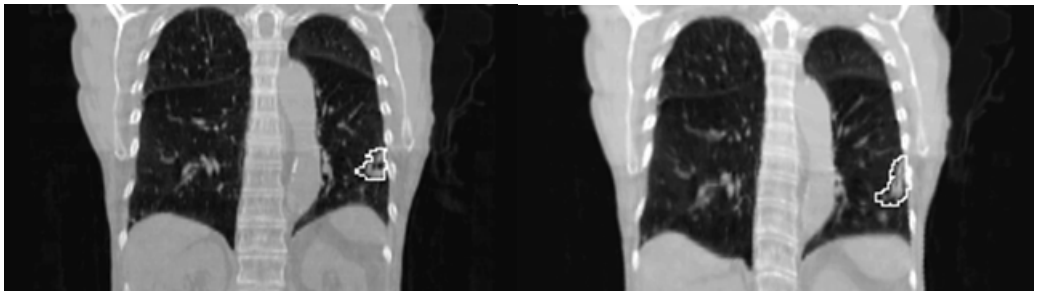

Figure 2.10: The left image shows a coronal view of the expiration CT image volume with the physician drawn tumor contour. The right image is a coronal view of the 3D TPS derived inspiration image volume along with the mapped contour.

The resulting rms errors are shown in Table 2.1 for each component of the displacement and each of the two tumor types evaluated. In all components, the rms error was less than 0.25 mm or one-fourth of the voxel dimension in the transaxial dimensions. The error was largest in the *z*-dimension, where the voxel size was 3 mm.

2.5.4 NCAT Digital Phantom Simulation

An important tool used in this study is the 4D NCAT, a computer generated phantom that simulates a thorax with both respiratory and cardiac motion [16]. However, optical flow has limitation in regions with no local gradients, which is an issue about aperture. The aperture problem [18, 19] is a potential difficulty when utilizing OFM to perform tracking of a uniform tumor model in the simulations. The aperture problem results from one (OFM property) which limits estimation to the component of displacement in the direction of the image intensity gradient. Structures within a volume help to reduce such errors. A uniform tumor with constant pixel intensity would represent a potential difficulty. In this study we will overcome the limitation in accuracy that the aperture problem presents through the introduction of a small modulation of the tumor intensity.

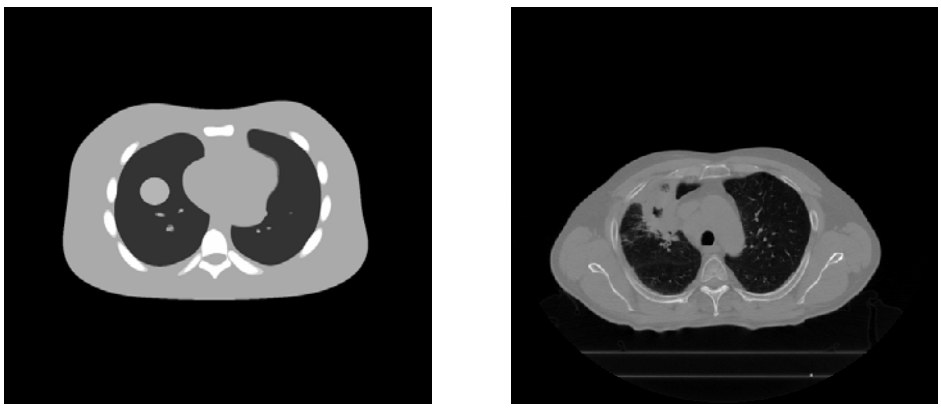

Figure 2.11: NCAT digital Phantom (left) versus reality (right)

The NCAT phantom is modified to generate a simulated lung tumor within a set of simulated 4D CT images with known displacement from reference. A 3D OFM algorithm is applied to estimate the tumor displacement. A series of phantom sets with varying complexity of modulation is generated. The error between the known phantom displacement and the 3D OFM estimation is calculated. The modified 4D NCAT phantom with small amplitude modulation was utilized in this study.

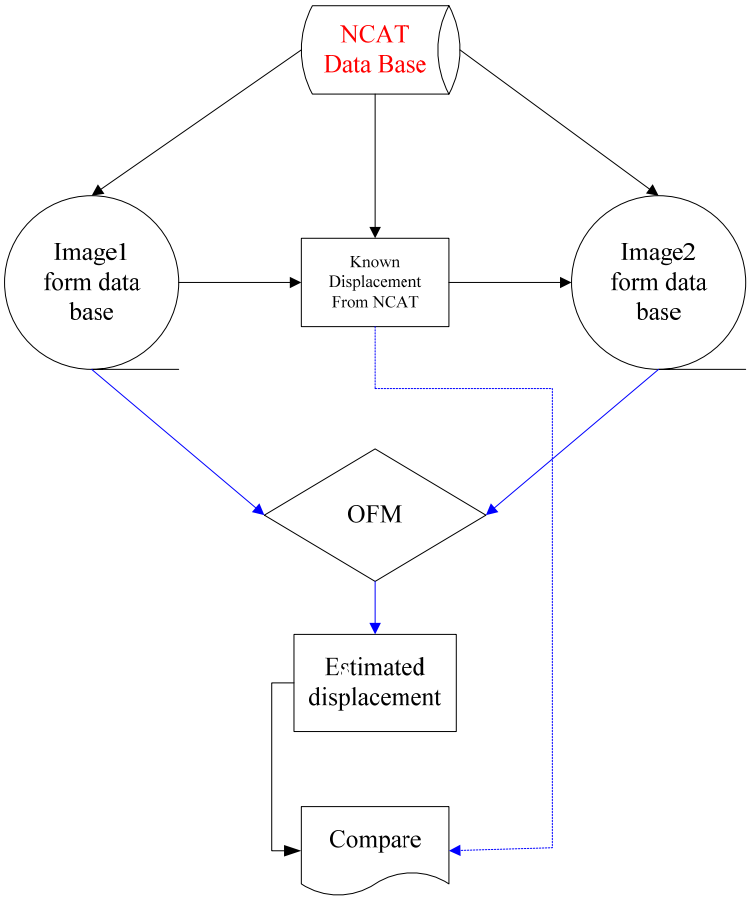

Figure 2.12: Implement flow chart

2.5.4.1 The 4D NCAT Phantom

In this study the NCAT phantom was modified to allow the insertion of tumors within the phantom that move with the surrounding tissue and contain a variable modulation of voxel CT value within the tumor. A series of eight 3D simulated thorax

CT image sets with respiratory motion corresponding to a tidal volume of 900 cc with a 5 cm spherical tumor at the level of the diaphragm were created. Sample output of the NCAT phantom is shown in Figure 2.11. Tumor voxel intensity modulation was varied and the orientation of the modulation is given in Table 2.2. The peak-to-peak intensity modulation was 4 percent.

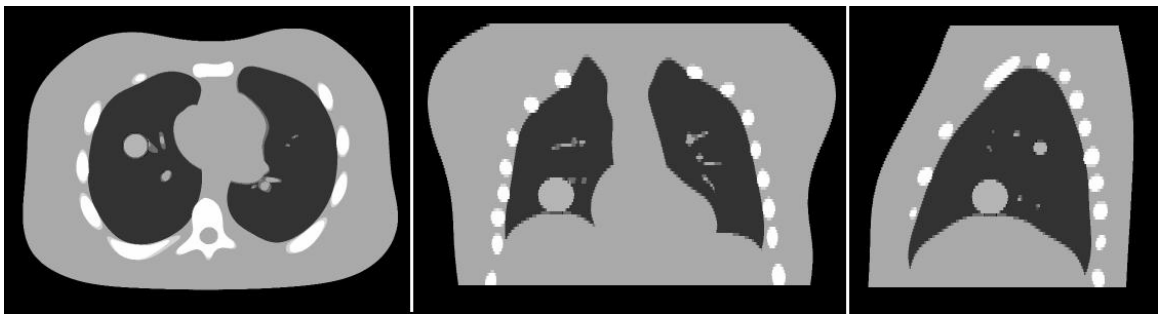

Figure 2.13: These images show the NCAT phantom with tumor present. The transverse, coronal, and sagittal views are shown through the tumor center.

The NCAT phantom image resolution was set to 1 mm in the transverse (x,y) dimensions and 3 mm in the superior-inferior (z) dimension. The lung tumor in the phantoms was placed immediately above the diaphragm to allow maximal movement. The tumor moved with the surrounding tissue; the displacement of tissue elements between the exhalation and inhalation 3D image sets were provided by NCAT for comparison as illustrated in Figure 2.13.

2.5.4.2 Motion Estimation

The 3D OFM was applied to calculate the displacement field for each of the series of phantoms created. The resulting displacement field was compared with the known displacements provided by the NCAT software and the resulting errors were

calculated.

2.5.4.3 Results

The orthogonal images through the NCAT phantom are shown in Figure 3.2. The tumor modulation for each of the phantom sets created is shown in Figure 3.3 and its modulation was kept to 4 percent on our initial series of calculations. The displacement errors for the 3D OFM calculated displacement are shown in Table 2.2 and shown the RMS error for the entire tumor volume.

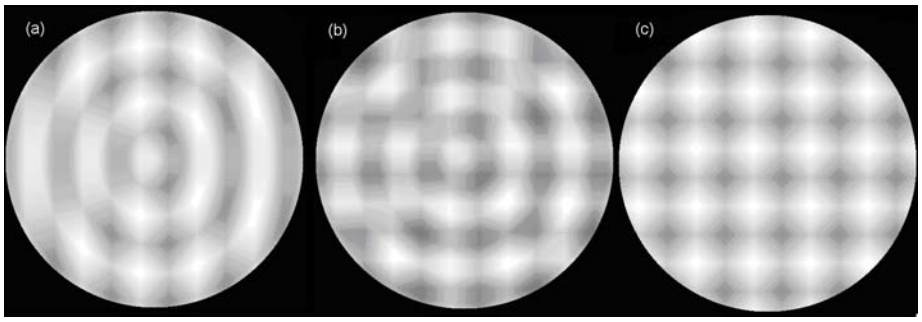

Figure 2.14: Intensity modulations in the sphere lung tumor created by NCAT: (a) radius + lateral; (b) radius +anterior-posterior + lateral; (c) anterior-posterior + lateral + superior-inferior.

Table 2.2: Indicates the tumor modulation direction utilized in each phantom generated (Figure2.14).

	Radial	A-P	Lateral	Sup-Inf
a	+		+	
b	+	+	+	
c		+	+	+

Table 2.3: The RMS Errors of optical flow estimation with tumor displacement versus intensity modulations (Figure 2.14)

Modulation	a	b	c
X error (mm)	0. 16 ± 0.01	0.12 ± 0.02	0.16 ± 0.01
Y error (mm)	0.10 ± 0.01	0.09 ± 0.02	0.11 ± 0.02
Z error (mm)	0.11 ± 0.01	0.10 ± 0.01	0.11 ± 0.01

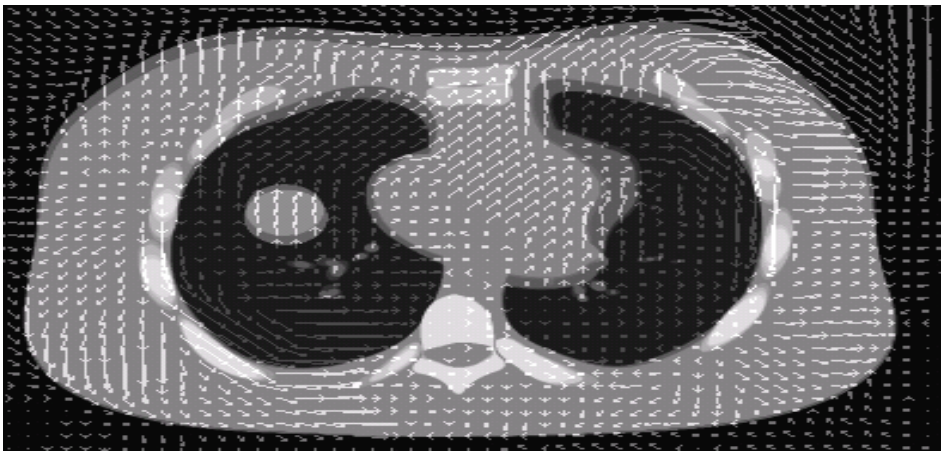

Figure 2.15: (a) NCAT phantom with displacement vector shown in transverse view;

(b) phantom with displacement vector shown in coronal view;

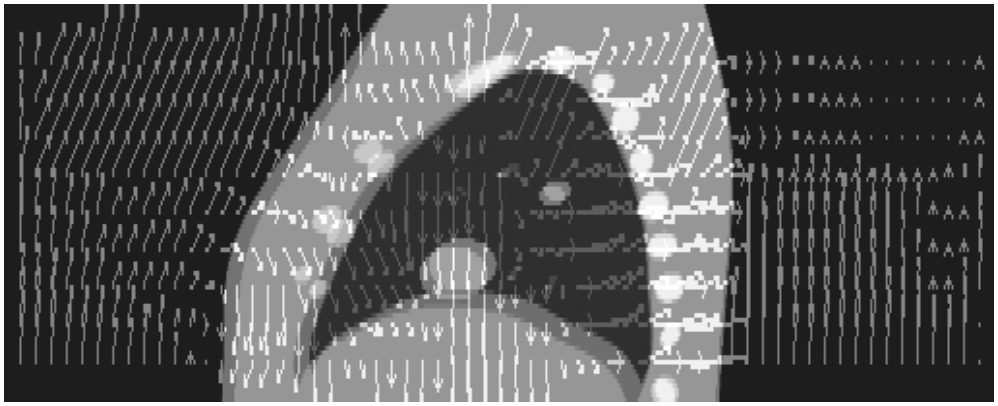

(c) phantom with displacement vector shown in saggital view.

A modified NCAT phantom with small modulations can be utilized to test and develop 3D OFM for 4D dosimetry and tumor motion studies. Both 3D OFM and the modified NCAT phantom will provide good tools in developing clinical applications that use voxel-to-voxel mapping.

3. Elastic Image Mapping for 4-D Dose Estimation Thoracic Radiotherapy

3.1 Introduction

Respiratory motion introduces uncertainty in the radiation treatment of thoracic malignancies and has the potential to significantly reduce the dose delivered to the tumor. Current treatment planning systems do not explicitly account for the respiratory motion in radiation dose calculations. The uncertainty due to respiratory motion requires an extra margin of normal tissue to be included in the radiation portal. The effect of respiratory motion on the delivered radiation dose is the subject of ongoing investigations [20-28]. Four-dimensional (4-D) computed tomography (CT) imaging allows respiratory motion measurements as an integral component of the radiation treatment planning session [29] and has been proposed for use in both dose calculation and inverse planning [30]. A 4-D CT thoracic data set consists of multiple full 3-D CT thoracic image volumes, perhaps eight or more, sampling the entire respiratory cycle. Using a 4-D CT data set, the radiation dose is calculated separately for a typical radiotherapy plan on each of the component 3-D image volumes. Various ways to integrate these data sets have been proposed. In this study, we introduce an elastic image mapping algorithm to allow path integration of the radiation dose across the respiratory cycle for each tissue element, providing an estimate of the radiation dose to each organ or tumor that includes the effect of respiratory motion.

3.2 Materials and Methods

3.2.1 4-D NCAT Phantoms

The 4-D NCAT digital phantom software package [16] was modified to allow the insertion of tumors within the phantom that move with the surrounding tissue. A spherical tumor 3.5 cm in diameter was placed within the phantom with its motion characteristics made to follow those of the underlying normal tissue. The NCAT phantom software was also modified to provide a map of the displacement vector for every tissue element between the component 3-D image sets and the end expiratory 3-D image set when generating the phantom 4-D image set. The respiratory motion was determined by setting the thoracic volume change equal to an average normal tidal volume.

3.2.2 Radiotherapy treatment planning

A 3-D conformal treatment plan was designed using the maximum expiratory image volume from the 4-D phantom with the Pinnacle version 6.2b treatment planning system (Pinnacle3; Phillips Radiation Oncology Systems, Milpitas, CA). Clinical target volumes (CTVs) [31, 32] were generated using 5 mm margins on the gross tumor volumes (GTVs) [4]. The treatment plan isocentre was placed at the tumor centre on the maximum expiratory image set. No margin was added in the superior–inferior direction (z axis) to aid with illustrating the effect of motion on the resulting radiation dose distributions. The collapsed cone convolution dose algorithm was used for all dose calculations [33]. The isodose distributions resulting from the treatment plans are shown in Figures 3.1 and 3.2. The prescription dose was designed to provide coverage for 95 percent of the CTV and was set to 60 Gy.

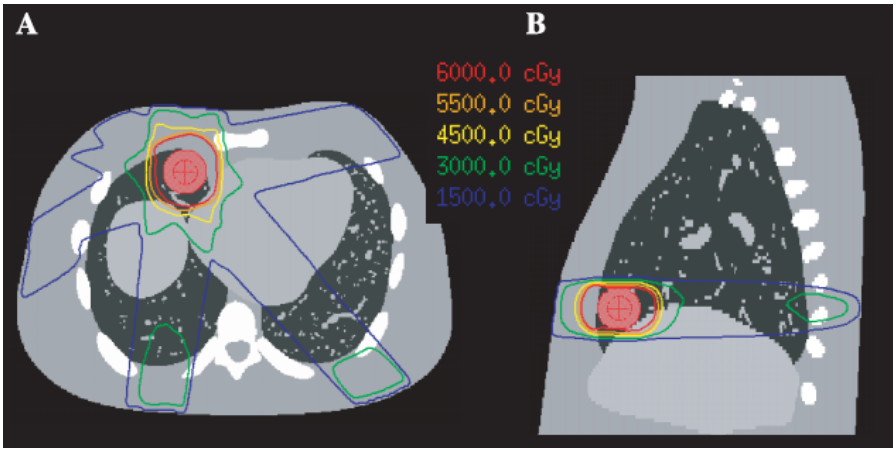

Figure 3.1: The simulated CT images from the 4-D NCAT phantom with a lung tumor 3.5 cm in diameter located in the right anterior lower lobe adjacent to the diaphragm are shown. The end expiration image volume is shown with the 3-D radiotherapy treatment plan isodose distribution superimposed in (A) a transaxial view through the tumor centre and (B) a sagittal view through the tumor centre. The 60, 55, 45, 30, and 15 Gy isodose lines are shown.

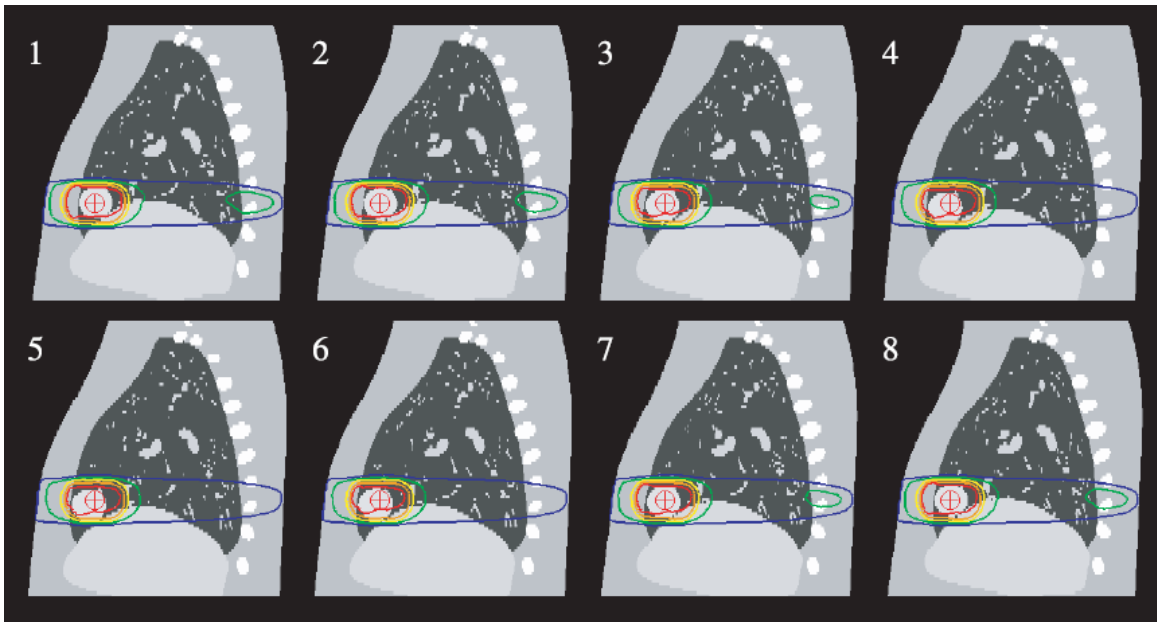

Figure 3.2: A series of eight 3-D snapshot CT image volumes was created with equal time sampling across the respiratory cycle as a measure of respiratory motion. A sagittal view of the isodose distribution is shown for all eight phases of the lung tumor case. A significant challenge in 4-D dosimetry involves summation of the multiple component dose distributions to obtain an estimated tissue dose.

The treatment plans from image volume 1, the maximum expiratory image set, were transposed onto the other 7 image volumes without modification for both the

lung and esophagus tumor cases. The resulting set of eight dose distributions, shown in Figure 3.2, represented a 4-D dose distribution that included the effect of respiratory motion on the original treatment plan (Figure 3.1).

3.2.3 3-D optical flow method deformable registration

The 3-D OFM is applied to each of the component images with reference to the end expiration image (Figure 3.3). The 3-D OFM yields a displacement vector map for every voxel, allowing the location of each tissue element in the maximum expiratory image volume to be traced through the entire respiratory cycle, represented by the eight image volumes making up the 4-D phantom data set.

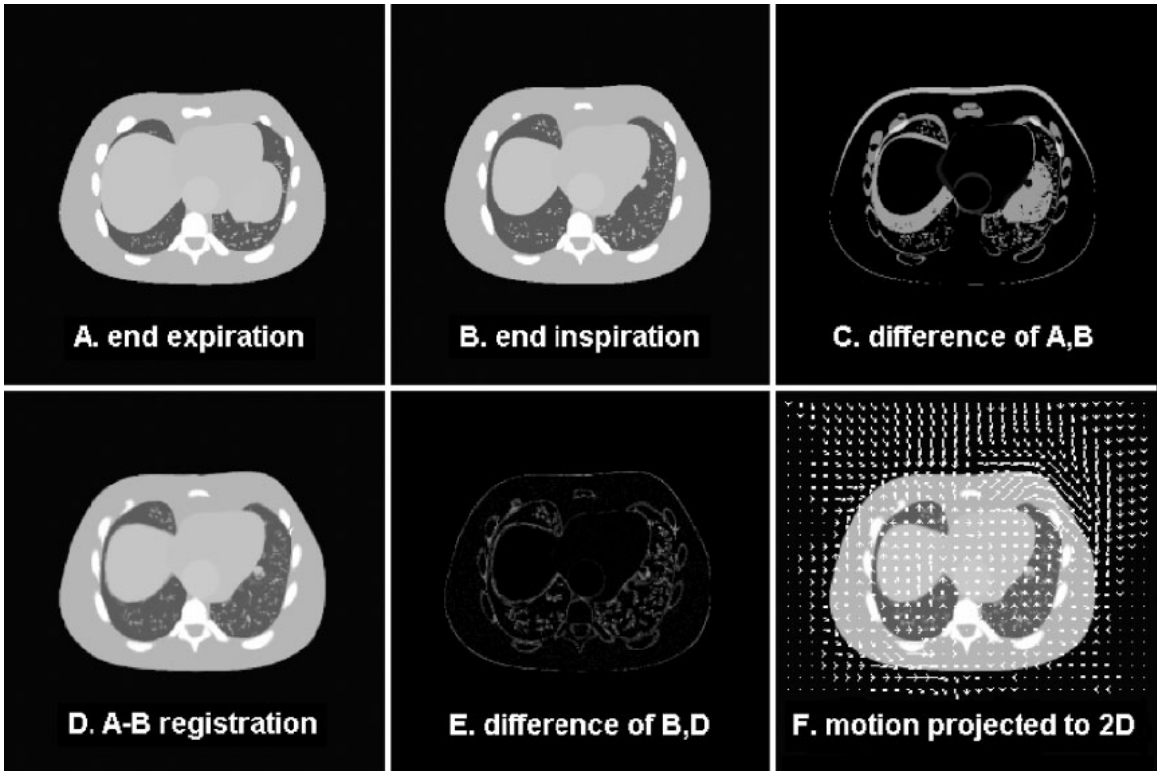

Figure 3.3: This figure demonstrates deformable image registration using the 3-D optical flow method (OFM) algorithm. (A) A transverse view of the end expiration CT volume; (B) the corresponding slice to the location of the slice in A at end inspiration; and (C) the difference between (A) and (B). The 3-D OFM algorithm is applied to register the image volume at end expiration (source) to the volume at end inspiration (target) is depicted in (D). A slice from the resulting registered image is shown in (E), and depicts the difference between the estimated image (D) and the target image (B). Finally, (F) depicts a

projection of the 3-D displacement vectors obtained from the 3-D OFM algorithm projected onto the image in (A).

3.2.4 Numerical path integration

The tissue dose distribution, Dtissue(x,y,z), which represents the dose that each tissue element will receive, is obtained from the path integration of each tissue element through the entire 4-D dose distribution, Dtissue(x, y, z, t), for each tissue element.

$$D_{tissue}(x,y,z) = \int_{\vec{v}(\vec{x},t)} (x,y,z,t)dt$$

, where t is taken over the entire respiratory cycle.

This calculation was performed numerically using the displacement vector field, $\vec{v}$, for each tissue element. The integrated dose distributions were reinserted into the Pinnacle treatment planning system for subsequent analysis.

3.3 Results

A simulated 4-D CT data set of a thorax with a lung tumor 3.5 cm in diameter located in the right anterior lower thorax above the diaphragm was generated with the 4-D NCAT phantom software. Axial and sagittal views of the phantom at the maximum expiratory phase are shown in Figure 3.1. A sagittal view of the isodose distribution is shown (Figure 3.2) for all eight phases of this lung tumor case. The isodose lines drifted off the lung tumor target as a result of respiration induced tumor motion, as illustrated in Figure 3.2. As inspiration increased, the tumor moved inferiorly, and the inferior tumor segment received a lower dose. This effect was not symmetric, and the region of dose loss was determined by the tumor trajectory. The lung tumor moved 0.7 cm inferiorly and 0.7 cm anteriorly from maximum expiration

to maximum inspiration. The diaphragm and dome of the liver moved into the treatment field changing the radiological depth which distorted the isodose line shapes. The CTV coverages at 100 percent and 95 percent were obtained from the DVH of each of the component treatment plans and are listed in Table 3.1.

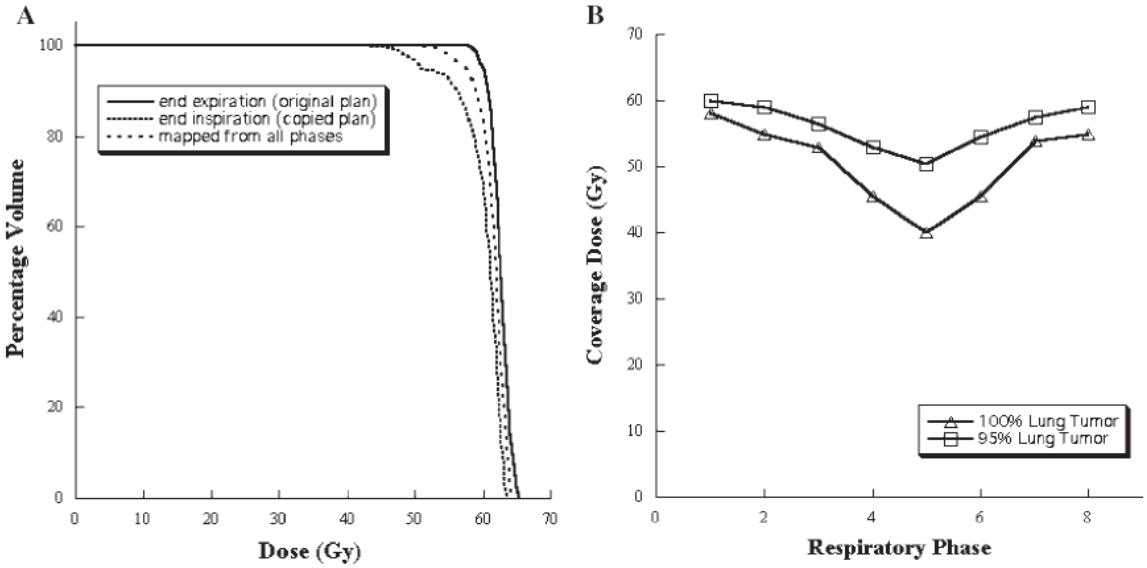

Figure 3.4: (A) The dose volume histogram plots for the lung tumor with the treatment plan created using an expansion margin for the GTV-to-CTV expansion of 5 mm. The static plan is shown with a solid line; the end inspiration plan is shown in dotted lines; and the path integrated plan is shown in dashed lines. (B) The 100 percent and 95 percent coverage doses for the CTV vs. the respiratory cycle phase. In the figure, the numerical respiration phases on the horizontal axis correspond to the names of the respiration phases in Table 3.1.

The coverage doses are shown graphically in Figure 3.4B. The eight individual dose distributions were then combined. The 3-D OFM algorithm was applied to each of the 3-D snapshot CT image volumes to perform elastic (or deformable) image registration with the end expiratory 3-D CT image volume as the reference image. The tumor displacement between maximum inspiration and maximum expiration as determined by 3-D OFM was compared with the known 4-D NCAT displacement, as shown in Table 3.2. The error was less than the voxel dimension; the error for tumor displacement was 0.57 mm. A numerical path integral was performed, giving equal

fractional weighting of one-eighth to each of the component doses. The resulting tissue dose distribution, Dtissue(x, y, z), which includes the effect of tumor motion, is shown in Figure 3.5. A DVH plot of the lung tumor's CTV is shown in Figure 3.4A for the static tumor, the path- integrated tumor and the end inspiration tumor. The end inspiration tumor DVH had the lowest CTV coverage doses of 40.0 Gy for 100 percent coverage and 50.5 Gy for 95 percent coverage. In contrast, the path integrated tumor DVH provided 51.0 Gy for 100 percent coverage and 57.5 Gy for 95 percent coverage.

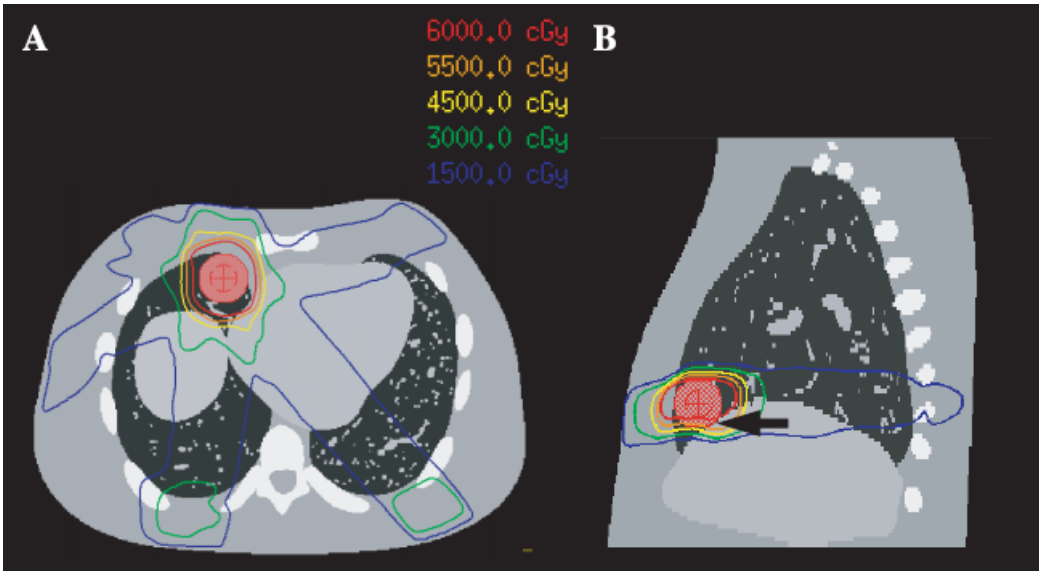

Figure 3.5: The tissue isodose distribution is shown in axial and sagittal sections through the tumor center. Both views show asymmetric loss of dose to the inferior portions of the tumor. The isodose lines sag with a downward curved trajectory as they extend from the tumor to the anterior skin. The 4-D dose distribution for the lung tumor case is shown, consisting of a 3-D distribution for each of the eight respiratory phases. A numerical path integration was performed using the 3-D OFM displacements to determine the path for each pixel volume. The resulting summed 3-D dose distribution is shown (A) in an axial section and (B) in a sagittal section. An arrow indicates an area of significant loss of the coverage dose.

Table 3.1: The 95 percent and 100 percent coverage doses for the clinical target volume formed from the gross tumor volume and a margin of 5 mm.

	100% Coverage (Gy)	95% Coverage (Gy)
1. End expiration	58.0	60.0
2. Early inspiration	55.0	59.0
3. Mid-inspiration	53.0	56.5
4. Late inspiration	45.5	53.0
5. End inspiration	40.0	50.5
6. Early expiration	45.5	54.5
7. Mid-expiration	54.0	57.5
8. Late expiration	55.0	59.0
Elastically summed	51.0	57.5

Table 3.2: Tumor displacement comparison between the 4-D NCAT known displacement and the 3-D OFM calculated displacement.

Tumour	4-D NCAT	3-D OFM	
	Displacement (mm)	Displacement (mm)	Error (mm)
Lung	9.95	9.38	0.57

3.4 Discussions

In this study, a deformable 3-D image registration algorithm, 3-D OFM, was used to map the trajectory of a potentially deformable moving target. The algorithm gave excellent results when compared with the known displacement of the computerized thoracic phantom. Path integration was performed for each tissue voxel from the reference image volume across the 4-D dose distribution data set. The resulting dose distribution was deformed in an asymmetric manner reflecting the motion trajectory. This finding is in contrast to the method proposed by Lujan et al [27]. Lujan proposed the performance of a convolution to account for the effect of respiratory motion on a static dose distribution, resulting in a blurred dose distribution. In this study the dose distribution was found to change as a result of patient motion

and the subsequent changing radiological paths. A loss of tumor coverage was the most significant effect for the lung tumors in the treatment plan studied. Finally, in this study, the 3-D OFM algorithm was used to determine the tumor trajectory from a 4-D CT data set. The measured error associated with this algorithm has been described previously as less smaller than the voxel dimension. In this study, agreement was found with the previously described accuracy, and the tumor displacement estimate derived from the 3-D OFM was in agreement with the known 4-D NCAT displacement.

3.5 Conclusions

The loss of complete (100 percent) CTV coverage was the predominant effect of respiratory motion observed in this study. Elastic image mapping made it possible to combine the component 3-D dose distributions generated from a 4-D CT data set into a single 3-D tissue dose estimate. The 3-D OFM method yielded an error smaller than the voxel dimensions in this study.

4. Validation of 4D Dose Calculations with 4D Phantom Measurements

4.1 Introduction

In the treatment of thoracic tumors, respiratory motion may cause a discrepancy between the planned dose and the delivered dose [34]. A previous 4D dosimetry study using the 3D OF program showed that respiratory motion could also cause loss of coverage to the tumors. Currently, although tumor coverage is improved by using different techniques such as gating [35], active breath control [36], the use of immobilization devices [37], and expanded PTV or ITV in planning [31], such techniques present undesirable consequences. Patient comfort may be compromised and/or increased toxicity may occur, as the fractional doses to the moving target are still calculated and/or accumulated based on static plans, neglecting the matter of tumor motion in dosimetry.

Motion and volume changes in respiration cycles are usually elastic, therefore, linear transformation is insufficient in 4D dose integration. To precisely estimate the delivered dose to an elastically moving and changing target, a point-to-point correspondence for the volume of interest among the 4D image set is needed to map the dose from each respiratory phase of multi-frames to a single frame, a process known as path integration.

Many algorithms have been applied to map dose distributions, including finite element modeling [38, 39], viscous fluid registration [40], contour-driven thin-plate spline, and intensity gradient-based optical flow. For many of these algorithms, validation of image registration was either poor or was not pursued in previous studies.

By contrast, the contour-driven TPS and the intensity gradient-based OF were validated with known displacement image sets and demonstrated accuracy in image registration [41]. However, the dose mapping and accumulation was not included in the validation for all techniques. Although the accuracy of dose mapping is mostly determined by the accuracy of the image registration, this further step from image registration should be validated since it also involves 3D linear interpolation calculations when the dose grid size is different from the image voxel size.

Measurement is always the gold standard in validation of dose calculations. In addition, dose calculation validation by measurement provides additional convincing validation for the image registration algorithm applied in the dose mapping. In the experiments discussed in this paper, dose distributions and point doses were calculated using the 3D OF program for different 4D setups with phantoms. The same 4D setups were used in measurements using ion chambers and films. The calculated 4D doses were compared with static plans and measurements.

Compared to other geometry based deformable image registration algorithms, such as TPS [15], the intensity-gradient based 3D OF program confers several advantages (e.g., user-friendly, no control points needed for registration, accuracy). Because OF registration is automatic and does not require any control point selection, thus no human interference, OF registration quality is consistent. Table 4.1 compares OF and other deformable image registration algorithms. In the table, MI is the mutual information algorithm [43] that is widely used in non-deformable image registration, and BM (block match or feature match) is a feature matching deformable registration algorithm [44]. The BM algorithm usually registers high frequency points precisely, such as edges and corners, but gives relatively large errors to low frequency points (i.e., slow or non-changing volumes) which usually make up the majority of an image.

At the initial stage of the study, a motion table built at The University of Texas

MD Anderson Cancer Center was used. This was later replaced by a motion table built with CT compatible materials for this 4D dosimetry study. A 4D dose path integration was performed on a moving thoracic phantom and a Capintec phantom using the 3D OF program.

A 3D linear interpolation computer program was written in C programming language to transfer dose grid data into the CT image voxel frame so that the displacement matrixes from OF calculations could be used to map dose distributions from one image set to another. The OF calculated relative dose distributions and absolute point-doses were compared with measurements.

4.2 Materials and Methods

4.2.1 Optical Flow Method

The optical flow method with iterative amendment and multi-resolution features were applied to image registration on different phases of phantom CT images.

4.2.2 Motion Tables

An easy way to simulate respiration motion with a phantom is to move the phantom reciprocally. A motion table that moves in one dimension is good enough to carry out the simulated motion (Figure 4.1). The platform of the table where the phantom set was built with all CT compatible materials. The table required pre-programming to generate command lines. These were sent to the motion controller via the hyper terminal, which is a built-in RS232 interface that exists on every personal computer (PC). A user-friendly computer interface program was developed for the motion table (Figure 4.2). A few parameters were required to be input to the interface, such as speed, acceleration / deceleration rates, motion range, *etc*. Since people tend to hold their breath for a little time at the end of expiration, the

control interface is programmed to reflect this behavior. Pre-programming was not needed when changing the motion profile. The Windows based computer program communicated with the motion controller via the RS232 interface. The motion range was 0-15 cm maximum; the range for respiratory motions was typically 0-2 cm. The first table had the advantage of being programmed for very complicated motion profiles, whereas the advantage conferred by the new table was overall ease of operation.

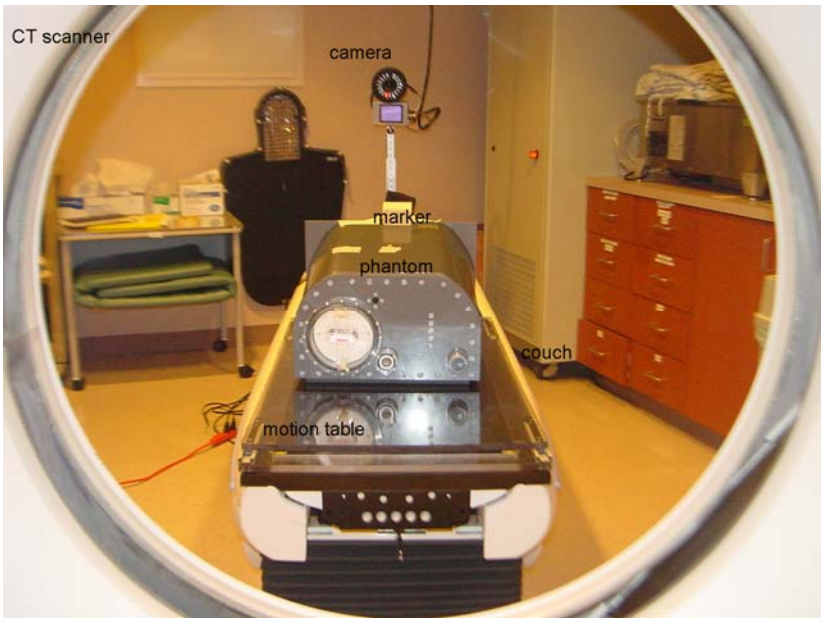

Figure 4.1: 4D CT scanning for the RPC thoracic phantom. While being scanned, the phantom moved at 18 cycles per minute, 2 cm travel distance in the SI direction. The same setup was used in dose delivery with the same motion pattern.

In this study, the frequency of the respiration motion was set at 18 cycles per minute, which is a typical human respiration frequency. The motion range was set at 2cm.

Figure 4.2: Table and phantom setup for the 4D dose delivery. The table and phantom in this figure are different from those in Figure 1. This setup was used in point-dose verification. Treatment plans were delivered when the phantom was moving with the motion table in the superior-inferior direction with the same pattern when the 4D CT was taken. An ion-chamber and a Capintec phantom were used to measure the point-doses.

4.2.3 Phantoms

Different phantoms were used in the dose distribution and point dose measurements. The Radiological Physics Center's (RPC) thoracic phantom [17] (Figure 4.3) was used in the dose distribution measurement. A Capintec phantom (Capintec, Inc., Ramsey, NJ) was used in the point-dose measurement (Figure 4.2).

The RPC thoracic phantom has an ellipsoidal tumor insertion inside the left lung where TLD and film can be inserted for dose measurement. For the dose distribution measurement in this study, film was inserted in the tumor in all 3 orthogonal views.

In the point-dose measurement, a Capintec phantom with a Wellhofer cc13 ion chamber (Scanditronix Wellhofer, Bartlett, TN) was utilized. This setup was often used in the IMRT QA point-dose measurements at Southwestern Medical Center.

Figure 4.3: The RPC thoracic phantom. The insertions include the lungs, heart, and spinal cord. In the left lung, there is an ellipsoidal tumor insertion where the films are located. The phantom is filled with water when scanned or treated.

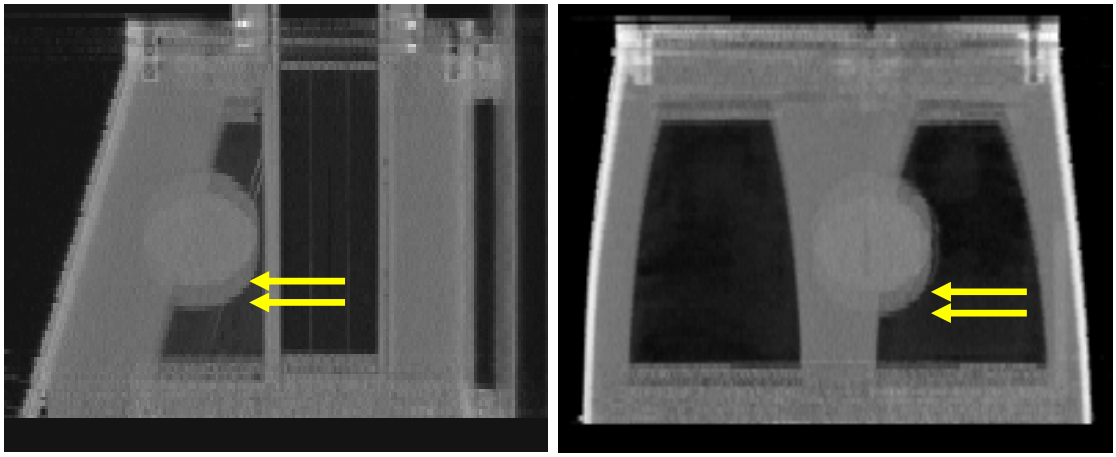

Figure 4.4: The sagittal view of the thoracic phantom with a reciprocal motion in the SI direction. The arrows indicate the displacement of the heart. No shape change was involved. The motion was single dimensional.

A one-shot phantom was built using polystyrene, originally for IMRT QA. The composite point dose and dose distribution were measured using a Wellhofer cc13 ion chamber and EDR2 film pack in the same dose delivery. This phantom was used in 4D dose measurements.

4.2.4 4D CT Data

The RPC thoracic phantom was placed on a programmable motion table to simulate respiratory motion. 4D CT imaging was performed on a multi-slice CT scanner (Philips Medical Systems, Andover, MA). Figure 4.1 shows the 4D CT imaging setup. The reciprocal motion was in superior-inferior (SI) direction. In this study, no elastic volume change was involved. The whole phantom moved together rigidly. The CT data was binned into eight phases in equal time intervals. Figure 4.4 shows the overlap sagittal views of the end inspiration and end expiration CT data.

4.2.5 Treatment Planning

The 4D CT images were sent to a Pinnacle workstation (version 6.2b, Phillips Medical Systems, Andover, MA) where a treatment plan was designed on the end expiration image set. The treatment plan was transposed onto the other respiratory phases and a 4D dose data set was thus generated.

For the RPC thoracic phantom dose distribution case, an AP, PA 2-field plan was generated on the phantom. For the Capintec phantom point-dose cases, a 7-field lung cancer IMRT plan and a single beam 3D plan were copied to the Capintec phantom. Point-doses to the tumor center (the center chamber slot on the Capintec phantom) and to a point close to the tumor edge (the chamber slot next to the center one) were calculated in the plans (Figure 4.5). The point dose to the center of the tumor was calculated in static and 4D. The dose distribution at the film plane was also calculated for each of the respiratory phases.

4.2.6 Dose Delivery

In the dose distribution measurement, the end expiration plan was delivered using a Varian 2100 linear accelerator (Varian Medical System, Palo Alto, CA) to the

RPC phantom while it was moving with the same motion pattern as it was scanned in the 4D CT imaging. The dose delivered to the RPC thoracic phantom was recorded using radiographic film.

Similar to the IMRT QA procedure, in the point-dose measurements, the measurement system (a Capintec phantom with a Wellhofer ion chamber) was calibrated with right and left lateral beams of known dose to the center chamber position. The plans then were delivered, and the point-doses were measured using the calibration factor and the chamber readings. For the IMRT plan, the composite point-doses were recorded. This measurement was designed primarily for the edge point dose measurement, since a Capintec phantom had 25 options to select a point dose location of interest which allowed a typical edge point to be studied. A point dose at the tumor center was also studied for comparison.

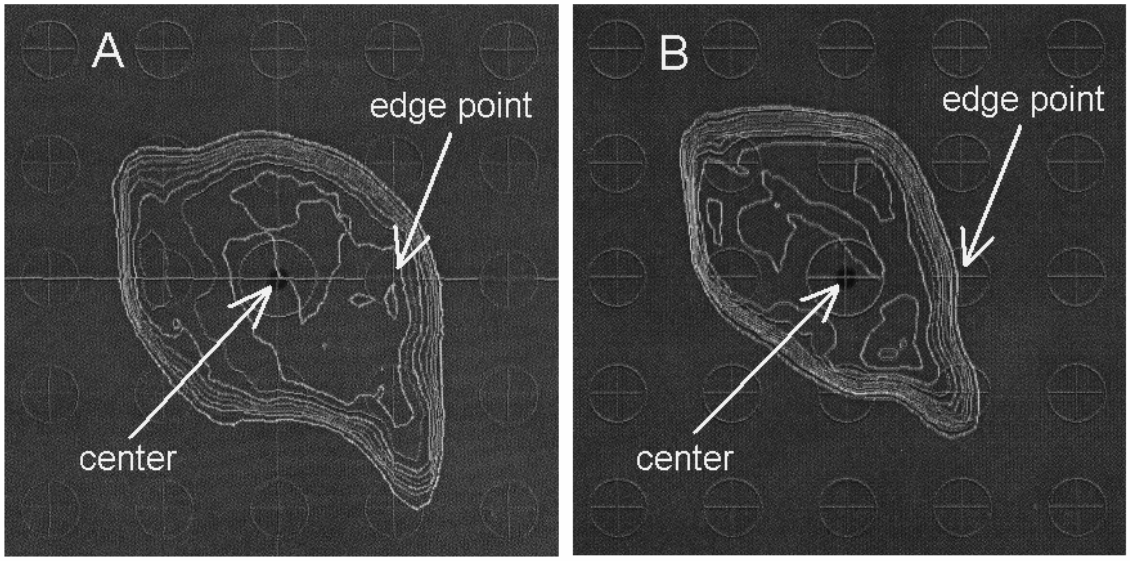

Figure 4.5: Transverse view of the composite dose distribution of the IMRT plan calculated by Pinnacle planning system. The circles represent the available chamber positions on the Capintec phantom. (A) The distribution of one end-position of the phantom where the tumor center overlapped with the beams' isocenter. (B) The distribution of the other end-position where the tumor center was off the beams' isocenter by 2 cm. The outer isodose line is the 70% line. The tumor center dose changed less than the edge point dose. The displacement matrixes calculated by OF were used to map the point doses from these distributions and summed with equal weight.

4.2.7 4D Dose Calculations

Since the voxel size in CT data is usually different from the size of a dose grid unit, a 3D linear interpolation computer program was developed to interpolate the dose distribution from dose grid system over to the image voxels, and interpolate the summed total dose back from image voxels to dose grid cells for further analysis by the Pinnacle planning system. Because of the unit size difference between the two frames, one image voxel is likely covered by parts of more than one neighboring dose grid cells, and one dose grid cell is covered by parts of more than one image voxels. Linear interpolation was used to transfer the dose data between the two frames. Data were weighted by the volume sizes of the frame units overlapping with the frame unit of interest.

The 3D OF was used to calculate the deformation fields between the CT data of the respiratory phases. The deformation fields were used to map the dose distributions of the multiple respiratory phases calculated by the Pinnacle planning system onto the end expiration phase. In calculating expanding volumes, occasionally one voxel in a phase became larger than a corresponding voxel in a subsequent phase. In this instance, the same dose was used for all of the expanded voxels. When calculating shrinking volumes, occasionally multiple voxels in one phase were represented as one voxel in a subsequent phase. In this instance, the dose for the resulting voxel was matched to the dose for the voxels in the former phase.

Performing numerical path integration, the resulting dose distributions were summed with equal weighting since the respiratory phases were in equal time intervals. The path integrated dose distribution was compared with the measured dose distribution and the static plan. The deformation matrixes of the Capintec phantom were used to select point doses from dose distributions of all of the phases calculated by the Pinnacle planning system and summed in equal weighting.

4.3 Results and Discussion

4.3.1 Dose Distribution

Figure 4.6 illustrates the dose distributions of the RPC phantom measurement and the corresponding calculation. A coronal section through the static treatment plan is shown in figure 4.6A. The 3D OF algorithm was applied and numerical path integration performed on the 4D dose distribution data resulting in a single 3D dose distribution. The corresponding coronal section is shown in Figure 4.6B. A coronal section through the measured dose distribution, which was recorded on two separate films, is shown in Figure 4.6C. The comparison between the dose profiles is shown in Figure 4.7. The delivered dose distribution had a peak width at 90 percent maximum of 38.5mm. The corresponding value for the path integrated 4D plan and the end expiration static plan were 42.6mm and 47.0mm. The 50 percent isodose line was displaced 0.5mm when compared to the path integrated 4D plan, and was displaced 8.6mm when compared to the end expiration static plan.

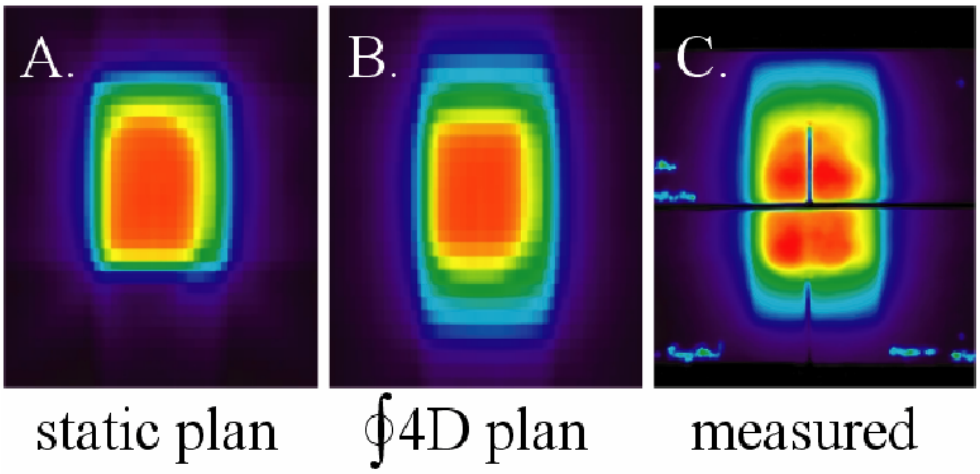

Figure 4.6: Coronal views of the dose distributions A) the static plan on the end expiration phase; B) the OF path integrated dose over the 4D image set; and C) the measured dose. It is expected that the dose distribution from the static plan covers a range shorter than the 4D dose in the SI direction. The path integrated dose is very close to the measurement in the coverage range in the SI direction. The measurement dose distribution was recorded by two separate films. The gap between the films is represented as a horizontal black line through Figure C. The thin vertical lines within the figure represent slices made to fit other films orthogonally in the tumor insertion.

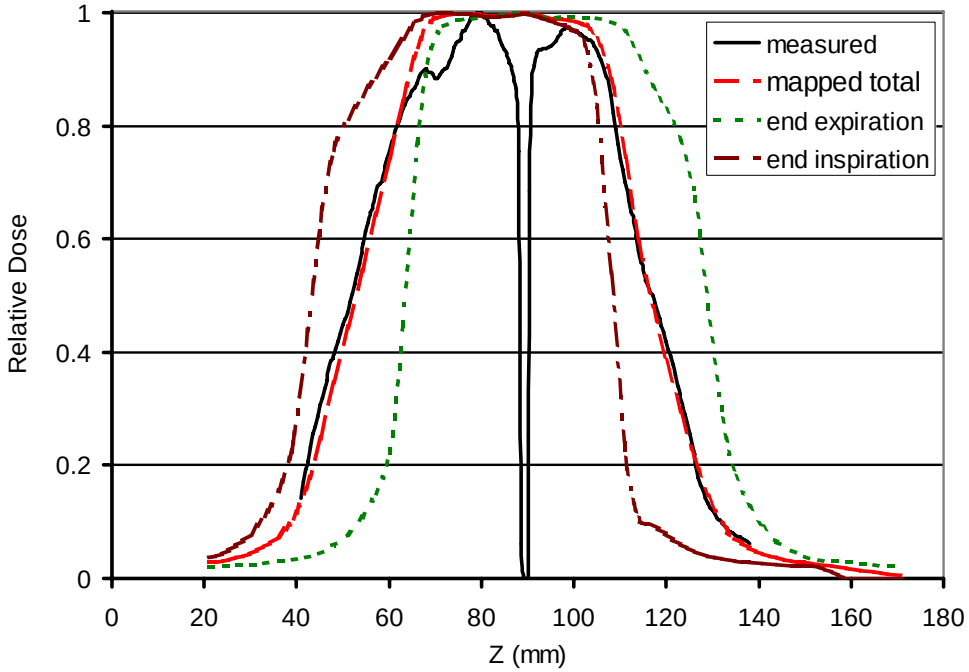

Figure 4.7: The comparison of the dose profiles across the central line of the tumor insertion in the superior-inferior direction. The OF calculated and the measured dose profiles matched very well, only 0.5mm off at 50% isodose line. As expected, the end expiration and end inspiration profiles are noticeably off the central line. The deep dip on the measured profile is introduced by the gap between the two pieces of films (see Figure 4.6C).

Comparison of the dose distribution recorded by the saggital view film and the static and calculated 4D dose distributions yielded similar results. The relative dose distribution recorded by the film of the transverse view did not reflect a significant difference between the 4D estimation and the static plan (Figure 4.8), as that film was always inside the beams and was well covered when the dose was delivered.

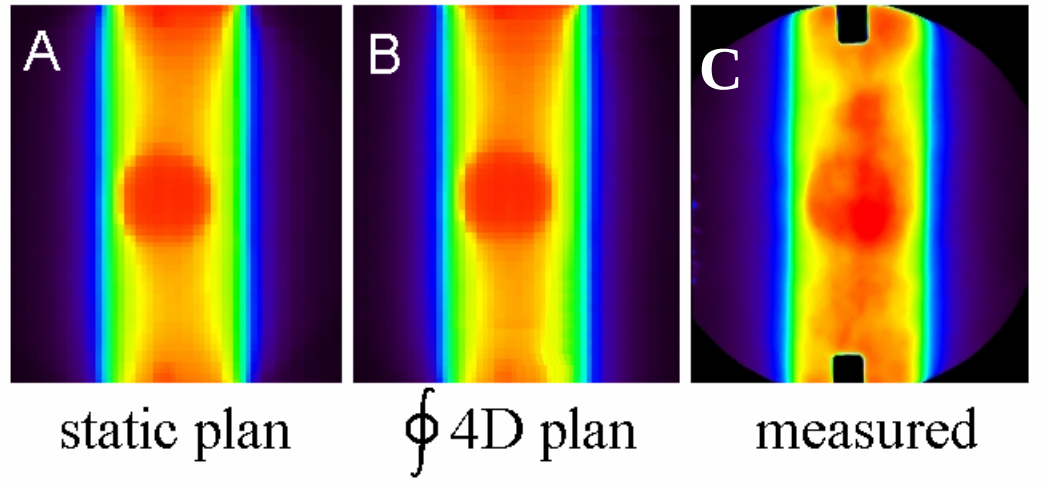

Figure 4.8: Transverse views of the dose distributions of A) the static plan on the end expiration phase; B) the OF path integrated dose over the 4D image set; and C) the measured. The film was parallel to the direction of the beams and was inserted at the middle plane of the ellipsoidal tumor insertion, thus was well within the fields even with the motion of 2cm in range. The relative dose distributions were not significantly different.

When a Capintec phantom was used, the calculated IMRT composite point-dose with motion was 6 percent lower than that of the static plan for the isocenter, while measurement showed it to be 4 percent lower. Calculated with motion, it was 8.6 percent lower for the point closer to the tumor edge, while measurement showed it to be 12.5 percent lower. The discrepancies between calculations and measurements were most possibly due to setup errors and the fact that the IMRT doses were not equally distributed over all phases. The setup errors were obviously shown in the edge point dose measurement: both static plan and OF calculation gave a higher dose than that of the center point, while the measurement gave an opposite result due to the fact that the edge point was located at a relatively sharp dose gradient volume (Figure 4.5, Table 4.2). A few 3D plans of various field sizes were studied. For the worst case in 3D plans, the agreement between measurements and calculations was within 1.5 percent. Table 4.2 summarizes the point-dose comparison.

The current study has only dealt with 1D motion so far. And the phantom itself

did not change in shape or volume, but moved rigidly with the motion table. The results from this 4D dosimetry validation study are promising. Further studies, especially the validation in cases of elastic volume change, which are closer to real respiration cycles, are in the future work plan. However, due to the nature of the OF algorithm it is fair to claim that the conclusions from this study can be extended to the elastic volume change cases. A deformable thoracic phantom with TLD insertion capability is planned to be built for the further studies.

Table 4.1. Comparison between various image registration algorithms

Algorithm	**Deformable**	**Control points**	**Content based**	**Quality**
MI	No	No	Yes	Good
TPS	Yes	Yes	No	Good
BM	Yes	No	Yes	Poor
OF	Yes	No	Yes	Good

Table 4.2. Comparison of point-doses between measurements and calculations

Point	**Static plan**	**OF calculated**	**Measured**	**% diff. plan-msr.**	**% diff OF-msr**	**% diff plan-OF**
IMRT center	193.9 cGy	183.0 cGy	186.7 cGy	3.86	-1.97	5.95
IMRT edge	199.1 cGy	183.3 cGy	176.9 cGy	12.5	3.63	8.59
3D center	258.5 cGy	251.4 cGy	247.7 cGy	4.40	1.49	2.86

4.4 Conclusions

The 3D OF algorithm provides the displacement field necessary for numerical path integration to map a 4D dose distribution data set into a single 3D dose distribution accurately. The resulting dose distribution and point doses were found to more closely represent the delivered dose. Therefore, we conclude that the 3D OF algorithm confers a substantial advantage over the static plan for a moving phantom.

5. Dose Mapping for Radiotherapy Follow-Up Evaluation

5.1 Introduction

Two methods of post-treatment evaluation are used to investigate thoracic radiotherapy treatment complications. The first method involves utilizing a global parameter (e.g., the diffusion length for carbon monoxide [DLCO]) to determine, through statistical means and correlation with the dose-volume histogram (DVH), the dose distribution pattern that corresponds with the measured impairment [44-47]. This method results in parameters derived from the DVH that are statistically linked to radiation injury. For example, Lee [44] states that postoperative pulmonary complications occur more frequently in patients who receive more than 10 Gy radiation to 40 percent or more of the lung tissue. Gopal et al [48] used a similar technique with pulmonary function testing (PFT) as the post-treatment assessment in lung cancer patients. That study coupled changes in PFT with an empirical mathematical model for lung injury. A limitation of this approach is that the link between radiation dose and radiographic complication effect is computed through statistical measures. The second method used radiographic evidence of local injury and attempts to correlate local injury with delivered dose. In this approach, the injury is identified through global studies, and the focus of these studies is finding the relationship between the radiation dose and the injury. Correlation of the radiation doses with the uptake volume imaging studies used to assess injury is an important method of determining injury from dose.

In studies that relate post-radiation radiographic injury with the radiation dose, a few methods of data correlation are commonly used (Table 5.1). The first method is to manually choose regions of uniform dose on the treatment-planning or radiation

therapy (XRT) computed tomography (CT) images and corresponding regions on the post-radiation images [50, 51]. The radiation dose is obtained for the entire region of interest (ROI) and it is correlated with the radiographic findings for a similar region that is drawn on the post-treatment CT or single photon emission computer tomography (SPECT) imaging. The correlation or image registration is based on the investigator's personal interpretation. Geara [51] examined the effect of radiation dose on the development of lung fibrosis one year after completion of radiotherapy. In that study, the XRT CT images were visually aligned with the CT images acquired 1 year after completion of radiotherapy. The radiation dose was obtained from the treatment plan, and the degree of radiographic injury was obtained from the post-treatment CT images. In this manual selection method, the goodness of the image registration remains uncertain. Levinson et al [50] performed a similar study, correlating the degree of lung perfusion loss, as measured on SPECT imaging following radiation therapy with radiation dose. This technique is limited to radiation-dose distributions where there are homogeneous regions, which may limit its use with intensity-modulated radiotherapy (IMRT). In Levinson's study, the manual method was found to produce results that agreed with an automated method described below; however, the absolute error remains uncertain.

The automated method, performs a six degree-of-freedom rigid-body registration between the XRT CT image volume and the pre-treatment and post-treatment radiographic images using visual criteria [52]. In studies by Marks and colleagues [52-57], visual registration between pretreatment XRT CT imaging and post-treatment SPECT images was used. The registration of post-radiation SPECT imaging data with XRT CT based on visual criteria is subjective and has much potential for introducing uncertainties into the analysis. However, this technique was found to agree with the manual method previously mentioned [50].

The third method includes the combination of three methods: 1) utilizes externally placed fiducial markers to align pretreatment imaging studies; 2) the XRT CT imaging study, hence dose distribution; 3) post-treatment imaging studies. [53, 56]. Although the criteria for alignment of fiducials may be objective, the correlation between external fiducials and internal anatomy remains uncertain and may change over time. This uncertainty limits the accuracy of the correlation.

The fourth method utilizes a six degree-of-freedom rigid-body registration between lung- surface contours [58, 59]. In this method, it is assumed that regions of the lung remain in the same location relative to the radiation-dose distribution between the XRT CT imaging session and the post-treatment imaging session. It is also assumed that identical patient immobilization and set-up techniques are used. Anatomic shifts, tumor shrinkage or growth, the patient's breathing patterns, variations in equipment set-up, and other changes in the scanner couches may occur between the two imaging sessions. These changes become sources of added uncertainty and limit the potential accuracy of rigid-body registration.

Deformable image registration offers the potential to overcome the limitations imposed by rigid-body registration, allowing set-up differences and anatomic shifts to be accurately accounted for. Deformable image registration has been utilized previously to map CT images to positron emission tomography (PET) images obtained on different scanner couches and/or different patient positions for the purpose of PET attenuation correction [60]. The ideal registration method requires no control-point selection or user intervention in the registration process. The method should have a solid mathematical foundation with consideration of the underlying assumptions of its use, and must be validated for the type of studies utilized. The optical flow method (OFM) is one of the methods used in deformable image registration. This method registers images based on the image content properties and

outputs a voxel-to-voxel displacement vector field called the “velocity matrix.” Unlike the thin-plate spline (TPS) technique, another widely used deformable image registration method described by Bookstein [15] and Tsai [13], the three-dimensional (3D) OFM does not require control points or user intervention. 3D OFM has been shown to be an accurate method calculate measured motion between CT imaging frames, such as cardiac-wall motion [61, 62]. The OFM algorithm is based on an assumption that the difference between two image volumes is the result of non-uniform displacement. The iterative solution is robust, and when the algorithm is performed in multiple steps of increasing resolution, it can tolerate moderate differences between the two image volumes. The root-mean-square (RMS) error for spatial accuracy was determined to be less than 0.2 pixels in a study of the spatial accuracy of our implementation using image sets with known displacements.

Whole-body FDG-PET imaging was developed to provide oncologic information for use, primarily, in evaluating the extent of primary disease and metastases [63-66]. In post-treatment PET imaging, the standard uptake value (SUV) in the residual tumor has been found to correlate with the risk for residual disease [67]. In the study by Inoue et al [68] of 38 patients with suspicion of recurrent non-small-cell lung cancer (NSCLC), the sensitivity and specificity of FDG-PET in detecting recurrent disease were 100 percent (26/26) and 61.5 percent (8/13) [68]. For the 25 patients assessed, the difference in mean SUV between recurrent and benign lesions was statistically significant (1.2 +/- 5.7 vs. 3.5 +/- 1.8, respectively; $p < 0.0001$). FDG-PET may also have potential in the diagnosis and evaluation of the response of malignant mesothelioma to treatment [69]. Hypermetabolic activity has been observed in irradiated tissues, including those with radiographic pneumonitis on imaging with PET [70-72]. In post-treatment evaluation of thoracic malignancies, PET/CT imaging is beneficial because it provides clinical information in both PET and CT as well as

anatomic information for CT image registration. With post-treatment PET/CT imaging, evidence of persistent disease and radiation pneumonitis can be obtained simultaneously. Accurate correlation between the radiation dose and post-treatment imaging is necessary.

The purpose of the present study is to demonstrate proof-of-concept for use of deformable image registration to correlate the radiotherapy treatment planning dose distribution with the post-treatment PET/CT image volume, which will facilitate investigations of treatment complications, disease persistence, and disease recurrence. Three clinical cases of thoracic malignancy are presented to illustrate the type of information this new technique will produce, representing a synergy of cross-discipline data registration. In this study, we replaced visual and rigid-body registration of post-treatment PET/CT to XRT-CT with an unsupervised 3D optical flow algorithm, a deformable image-registration technique.

5.2 Materials and Methods

5.2.1 Optical Flow

The 3D optical flow program (OFM) has been validated against images of known displacements, and the errors were found to be smaller than the voxel sizes. The displacement matrix calculated by OFM between two images is employed to deform the dose distribution.

5.2.2 Patient Data

Three patients, each treated for a thoracic malignancy, were selected for this study. Each patient had a treatment-planning session in which CT images of the entire thorax and upper-abdomen, including the entire liver and both kidneys, obtained at 3-mm slice spacing on an AcQsim treatment-planning CT scanner (Philips Medical

Systems, Cleveland, OH) under normal breathing conditions. A Vac-lock bag (Medtec, Orange City, IA) and T-bar (Medtec, Orange City, IA) were utilized for custom immobilization. The patients' arms were place above their heads, and a flat radiotherapy table was utilized. After radiotherapy was complete, PET/CT imaging was conducted for all patients approximately 3 months after the XRT-CT imaging session. PET/CT imaging was performed on a General Electric Discovery ST (DST) PET/CT scanner (GE Medical Systems, Waukesha, WI) with a 70-cm bore, which allowed patients to be scanned in a position similar to the treatment position. The patients were scanned with their arms over their heads as they had on the diagnostic scanner table.

Patient One was treated for esophageal carcinoma with preoperative concurrent chemotherapy and radiation therapy [73]. The prescribed dose of radiation was 50.4 Gy. Patient Two was treated for NSCLC with concurrent chemotherapy and radiation therapy (prescribed dose of 63 Gy). Patients One and Two were both treated with 3D conformal radiation therapy. The Pinnacle system (version 6.2b; Philips Medical Systems) was used as the treatment-planning system. The collapsed cone convolution algorithm, which accurately accounts for tissue heterogeneity, was used to calculate radiation dose [74]. Patient Three was treated for malignant mesothelioma with post-operative radiation therapy using IMRT at a prescribed radiation dose of 50 Gy [75]. For each of the patients, a flat radiation therapy table was used for the XRT-CT and a curved diagnostic table was used for the follow-up PET/CT. The XRT- CT was obtained using 120-kVp x-rays, and it was reconstructed with 0.97mm x 0.97mm x 3.0mm pixels. The follow-up PET/CT was obtained using 140 kVp x-rays, and it was reconstructed with 1.07mm x 1.07mm x 3.3mm pixels. The variation in pixel sizes was accounted for in the calculations.

5.2.3 Image Registration and Analysis

In this study, for each patient case, three sets of image volumes are involved. The first image set is the radiotherapy treatment planning CT (XRT-CT), for which the pixel size is 0.97mm x 0.97mm and a single image is composed of 512 x 512 pixels. The slice thickness and axial sampling is typically 3mm. The second set is the post-treatment CT (PET/CT) image obtained from the General Electric PET/CT scanner, which also has a pixel size of 1.07mm x 1.07mm and is composed of 512 x 512 pixels. The slice thickness and axial sampling is 3.3mm. The third image set is the post-treatment PET, which is also obtained using the General Electric PET/CT. The PET image has poorer resolution than the CT image because it is composed of smaller-size pixels (5.5mm x 5.5mm) in a lower density (128x128 pixels). The slice thickness is 3.3mm, the same as that of the post-treatment CT image. To register the three image sets, the XRT-CT and the PET-CT are sub-sampled to a coarser resolution at a density of 256 x 256 pixels in a transverse slice, and the PET image is interpolated to 256 x 256 linearly. The registration between the PET-CT and PET images is assumed to be accurate because these images are acquired at approximately the same time using the same machine in a single patient setting. The 3D OFM is used to register the XRT-CT and the PET-CT.

Table 5.2 lists each patient's primary malignancy and the clinical findings demonstrated on the PET/CT image. For each patient, the XRT-CT image volume was registered with the PET-CT image volume using the 3D OFM. The PET/CT image set was truncated to cover the same axial range as the XRT-CT image set. The 3D OFM is applied with the XRT-CT as the source image volume and the PET-CT as the target image volume. No user intervention was required to process the 3D optical flow algorithm. A displacement matrix was calculated using the 3D OFM, relating each pixel in the XRT-CT to a corresponding location in the PET-CT.

Because the radiation treatment dose grid is based on the XRT-CT geometry, the dose is registered with the follow-up PET/CT using 100 iterations and four levels of hierarchical resolution.

Each PET/CT image set contains ROIs, either pneumonitis or foci suspicious for disease persistence. Contours were drawn using the Pinnacle treatment-planning system on the PET or CT from the follow-up PET/CT image set. The radiation dose was mapped to the follow-up PET/CT using the displacement matrix previously calculated using the 3D OFM. The corresponding dose in the ROIs was obtained on a pixel-by-pixel basis using the mapped radiation dose distribution. Fusion images were generated showing the radiation dose overlaying the PET or CT image from the follow-up image set.

The rms error was calculated with the PET-CT image volume as the known target. Calculations were performed for all voxels using the XRT-CT and the mapped CT images as estimates. The rms error was calculated using the following equation:

$$rms\ error = \sqrt{\frac{\sum_{i=0}^{N}\left(p_i^{PET-CT} - p_i^{XRT-CT}\right)^2}{N}}$$

where p_i^{PET-CT} represents the intensity of the ith voxel within the PET-CT image volume and p_i^{XRT-CT} represents the intensity of the ith voxel within the XRT-CT image volume. The rms error of the 3D optical flow calculation is estimated by replacing the XRT-CT data in the equation with the mapped CT data (from XRT-CT to PET-CT).

5.3 Results

5.3.1 Case One

The 3D optical flow algorithm applied to this case is compared with visual alignment in Figure 5.1. The XRT-CT and the follow-up PET-CT image volumes were manually aligned with the most superior image containing nearly identical vertebral body structures. The image superior-inferior spacing was 3.0mm for the XRT-CT and 3.3mm for the PET-CT. An XRT-CT and a PET-CT from the same axial slice number in the middle of the image volume are shown in Figure 5.1. The images are overlain, illustrating the mismatch between the images. The displacement matrix obtained from 3D OFM is applied to the XRT-CT image volume mapping it to the PET-CT image volume and is shown in the lower half of the figure. Figure 5.2 summarizes this result for two orthogonal planes through the image center. Figures 5.2A and 5.2B are coronal and sagittal slices through the XRT-CT image volume, which was obtained during free-breathing. Figures 5.2C and 5.2D are coronal and sagittal slices through the PET-CT image volume, obtained at mid-inspiration breathhold. The 3D OFM displacement matrix is applied to the XRT-CT (Figures 5.2A and 5.2B) in order to map the image volume to the PET-CT (Figures 5.2C and 5.2D). The resulting coronal and sagittal pair is shown in Figures 5.2E and 5.2F. The difference between the 3D OFM registered XRT-CT and the PET-CT were calculated and the corresponding sagittal and coronal images are shown in Figures 5.2G and 5.2H. There are only a few areas of difference, mostly in high gradient regions. The lungs and mediastinum appeared to map without significant errors. The rms is given in Table 5.3 for the entire image volumes calculated for the original PET-CT and the mapped PET-CT with respect to the XRT-CT. The rms error is reduced by a factor of 4.7 following the 3D OFM mapping.

A set of ROIs was drawn on both the CT and PET from the follow-up PET/CT

over the region shown in Figure 5.3 representing radiographic pneumonitis (see arrows) on the CT and inflammation on the PET. The corresponding dose mapped using the displacement matrix onto the images is shown in Figures 5.3E and 5.3F. The arrows are identically located to depict the region of radiographic pneumonitis on the PET and CT of the PET/CT images in Figure 5.3. A histogram of the radiation dose delivered to the CT-drawn ROI and to the PET-drawn ROI is shown in Figure 5.4. Of note, there was more uncertainty in defining the edge of the pneumonitis on the CT than on the PET images. The PET ROI has a broad dose peak between 30 and 44 Gy with a low dose tail extending to 0 Gy. The prescription dose was to 50.4 Gy, with the 95 percent isodose line providing coverage of the planning target volume (PTV). The CT ROI has a peak between 0 and 6 Gy and second broad peak between 25 and 44 Gy. The second broad peak from the CT ROI histogram overlaps the PET ROI histogram peak. The main difference between the two histogram curves, at the low dose range, may result from the uncertainty in delineating the region of pneumonitis on the CT images.

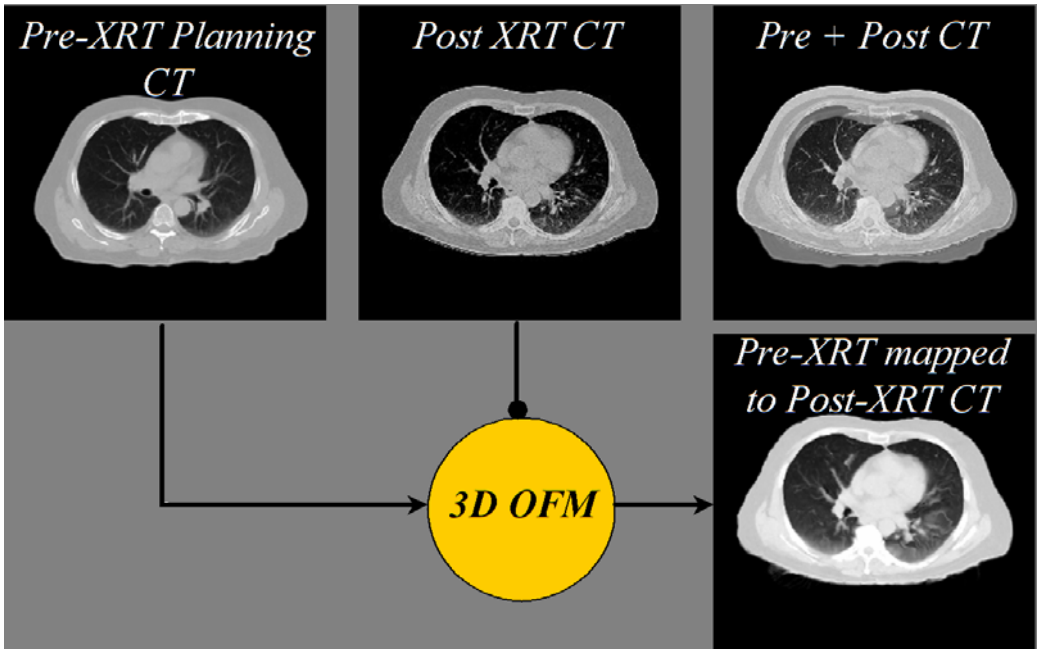

Figure 5.1: Flow diagram of the deformable image registration process used in this study. The pre-XRT treatment planning CT scan is the source image volume and the post-XRT CT, from the PET/CT, is the target. 3D OFM algorithm is applied to generate the displacement vectors between the source and target. A mapped image volume, where each pixel has been displaced is calculated.

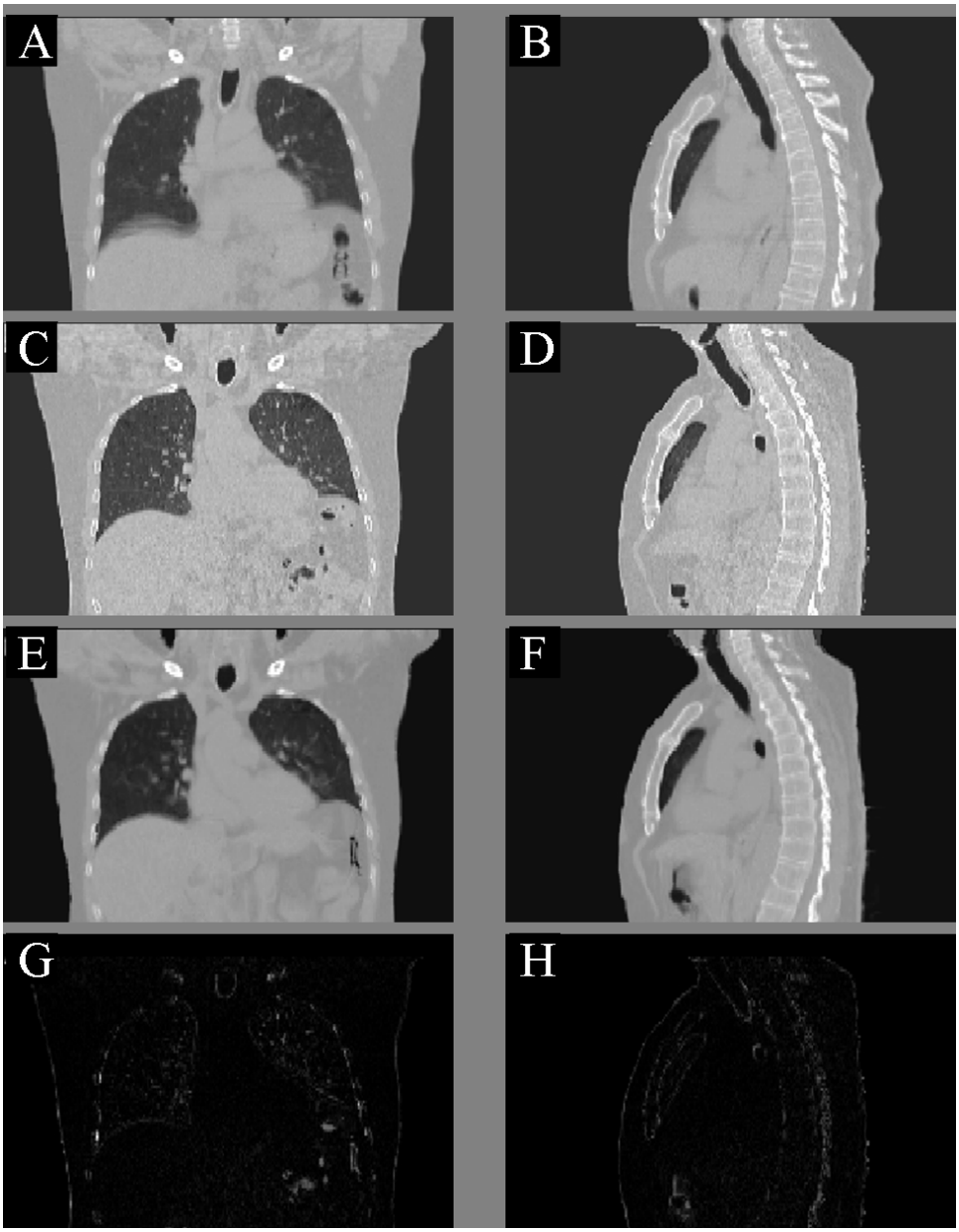

Figure5.2: The top image pair (A, B)is from the radiotherapy planning CT. The second image pair (C, D) is from the post-treatment PET/CT CT. The third image pair (E, F) is the result of applying 3D OFM to register the first to the second pair. The fourth image pair (G, H) is the difference between the 3D OFM registered image volume and the PET/CT CT volume.

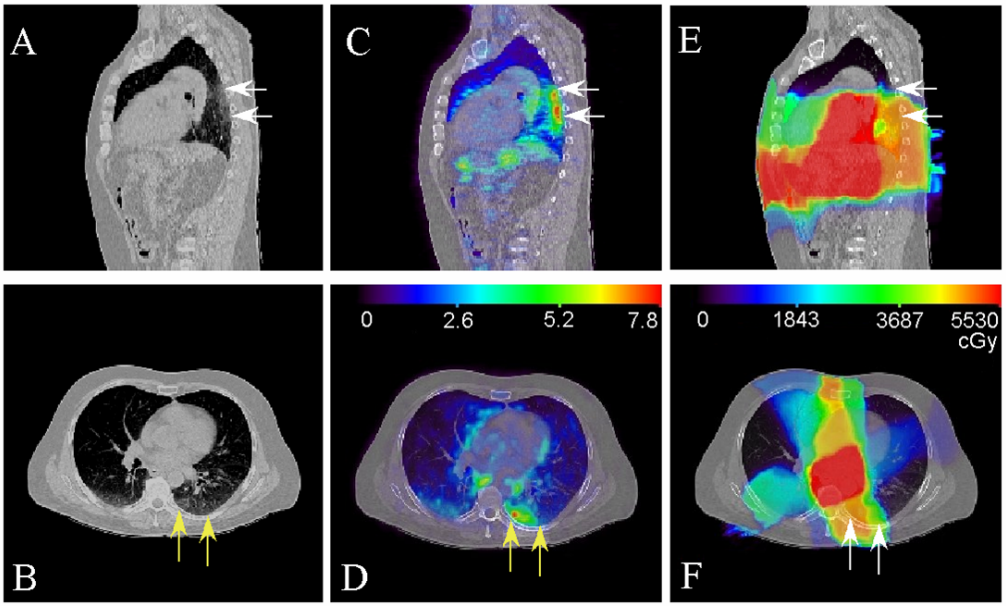

Figure 5.3: Case 2 shows the CT image volume acquired during the PET/CT image session one month following completion of radiotherapy. Arrows are placed to correspond to a region of radiographic pneumonitis. The FDG PET scan is overlain with the CT in the middle images (C, D). The radiotherapy dose is warped to the post-treatment PET/CT and overlain with the CT on the right (E, F).

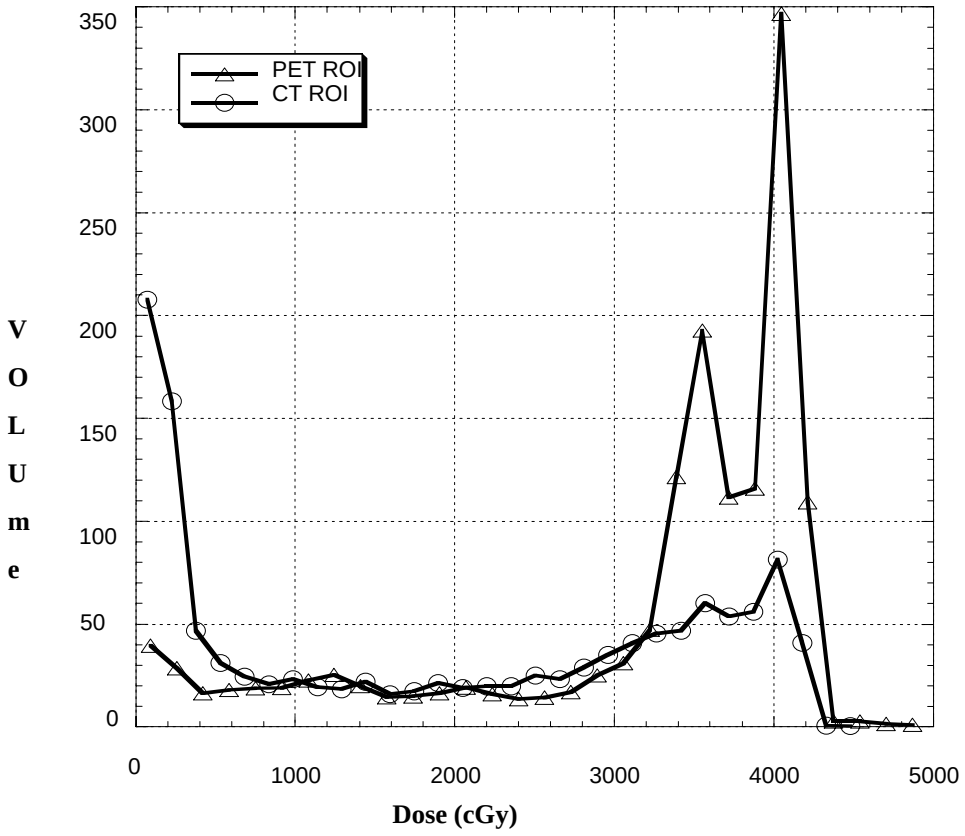

Figure 5.4: This figure shows graph of dose versus volume for the pneumonitis ROI drawn from the PET (triangles) and from the CT (circles).

5.3.2 Case Two

This patient received concurrent chemotherapy and radiation therapy for stage IIIA NSCLC. A PET/CT image was obtained one month after completion of treatment. Though asymptomatic, a large region with radiographic pneumonitis was found on the CT portion of the study (Figure 5.5A). The 3D OFM algorithm was applied to this case, and a transaxial image set is shown in Figure 5.5 with the post-treatment CT (A), PET/CT (B), and dose distribution mapped to the post-treatment CT images (C). The rms errors of the pre-mapped and mapped XRT-CT compared to the PET/CT CT are provided in Table 5.3. The 3D OFM reduces the rms error by a factor of 3.3, approximately one third of the original value. There were substantial differences between the two CT images, including a reduction in size of the primary tumor and the development of radiation pneumonitis at the inferior margin of the radiation field. Both of these changes were significant and might contribute to a residual difference between the mapped pre-treatment CT image and the PET/CT CT image sets.

The area of pneumonitis was identified on both the post-treatment CT and PET images. An ROI was drawn for each, and the corresponding radiation dose was obtained from the mapped radiation dose. As in Case One, the boundary of the pneumonitis ROI was more readily identified on the PET images than on the CT images, and the CT based ROIs were consistently larger. The radiation oncologist had more uncertainty in defining the CT-ROI versus the PET-ROI. A histogram of the radiation dose found in the CT-ROI and PET-ROI is shown in Figure 5.6. The CT-ROI resulted in a peak in the low-dose region, which might be due to the uncertainty in defining the edge of the effected area. The PET-ROI was more uniform, except for a low-dose peak between 35 and 45 Gy and a high dose peak. Both peaks were also present and more pronounced on the CT-ROI-derived histogram.

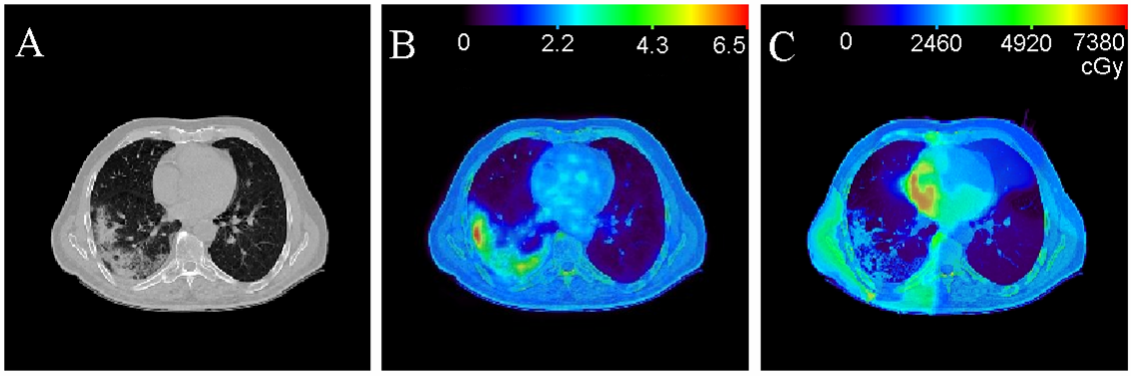

Figure 5.5: Image A shows a CT image below the level of the tumor from the post-treatment PET/CT image set with radiographic pneumonitis. Image B shows the corresponding PET overlaid on the CT image. Image C illustrates the warped dose distribution overlaid on the same CT image.

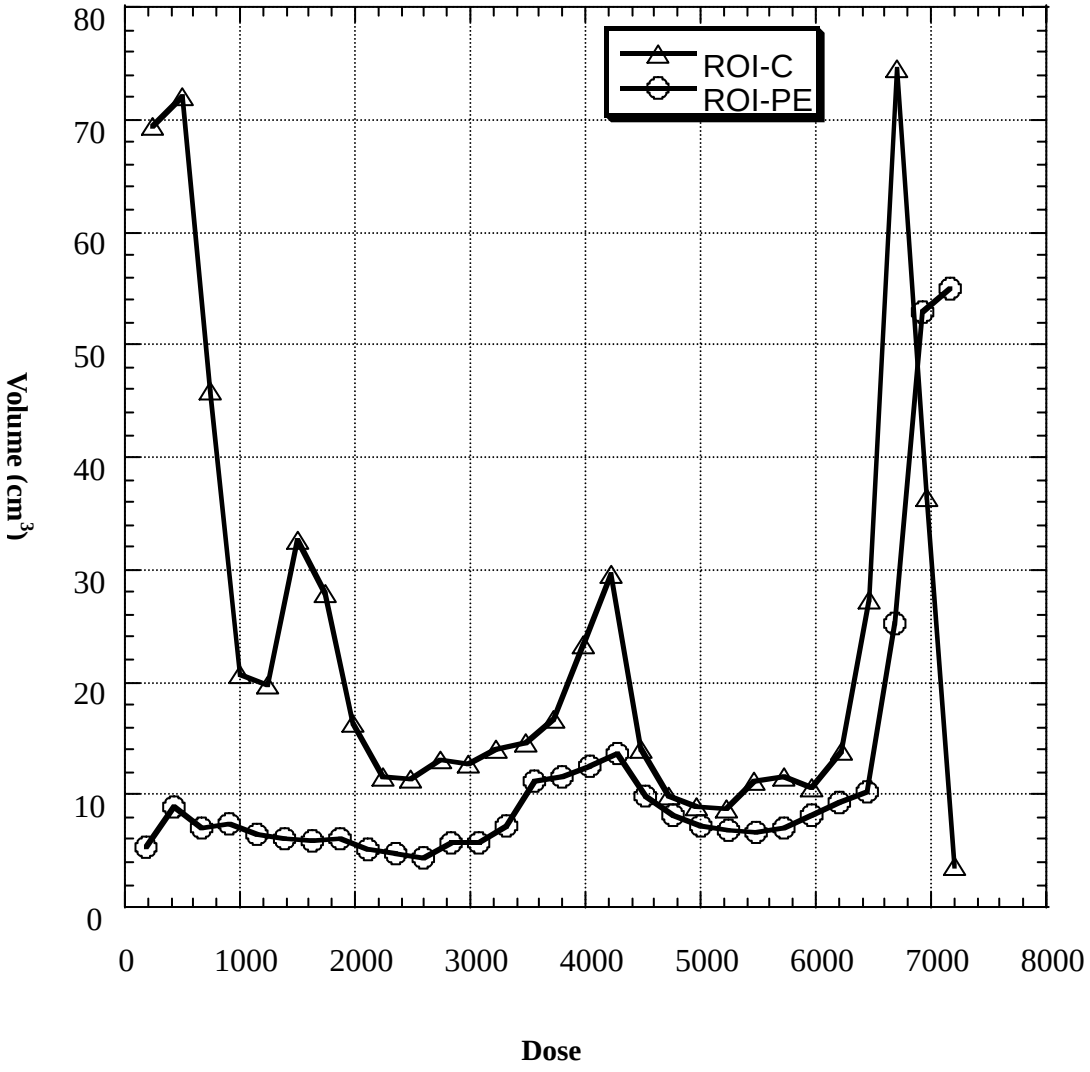

Figure 5.6: This figure shows a graph of the distribution of dose values contained within the region identified with radiographic pneumonitis on the post-XRT CT images for Case Two. The Y axis name, Volume, is diplayed unusually: can you flip it so that it is spelled in an upward direction rather than in a downward direction?

The difference between the PET-ROI and CT-ROI histogram curves might result from the uncertainty in delineating the region of pneumonitis on the CT images as well as differences in content of the ROIs. The PET-derived ROI reflected regions with hypermetabolic activity resulting from either inflammation or tumor persistence. This patient remains only mildly symptomatic from radiation pneumonitis with a dry cough.

5.3.3 Case Three

This patient received adjuvant IMRT to 50 Gy after extrapleural pneumonectomy. A suspicious mass was seen on follow-up CT imaging, and a PET/CT revealed suspicious hypermetabolic foci at six discrete locations. In this case, we sought to determine whether the suspicious regions received the full prescription dose of 50 Gy. The 3D optical flow algorithm was applied to register the PET/CT CT images, hence PET with the pre-treatment radiation therapy planning CT image. There were six regions suspicious for recurrence, identified in Figures 5.7A and 5.7B. The rms error values of the pre-mapped and mapped XRT-CT compared to the PET-CT are given in Table 5.3. There is a four-fold reduction in the RMS error for the mapped image versus the unmapped image volume when compared with the PET/CT CT image volume. The residual differences could be caused by differences in the CT acquisition properties, as the CT images were acquired on different CT scanners with different imaging parameters and patient couches. Alternatively, there are possible changes in the patient's anatomy in response to treatment.

The radiation therapy dose was mapped using the displacement matrix and is overlain on the CT image volume in Figures 5.7C and 5.7D. On review of the treatment plan without using image registration, it appears that all of the hypermetabolic regions on the PET images were contained in the high-dose regions.

A set of ROIs were drawn surrounding each of the suspicious regions from the PET images. With the mapped radiation dose and the drawn contours, a set of histograms representing the dose found at each of the recurrence sites is shown in Figure 5.8. Two of the most inferiorly located hypermetabolic regions were found to have low-dose regions; these are highlighted with arrows on Figure 5.8. The dose extends as low as 36 Gy for those two regions. All of the other regions, however, are found entirely above 50 Gy. Thus, recurrence from marginal miss will not explain all of these suspicious areas on the PET images.

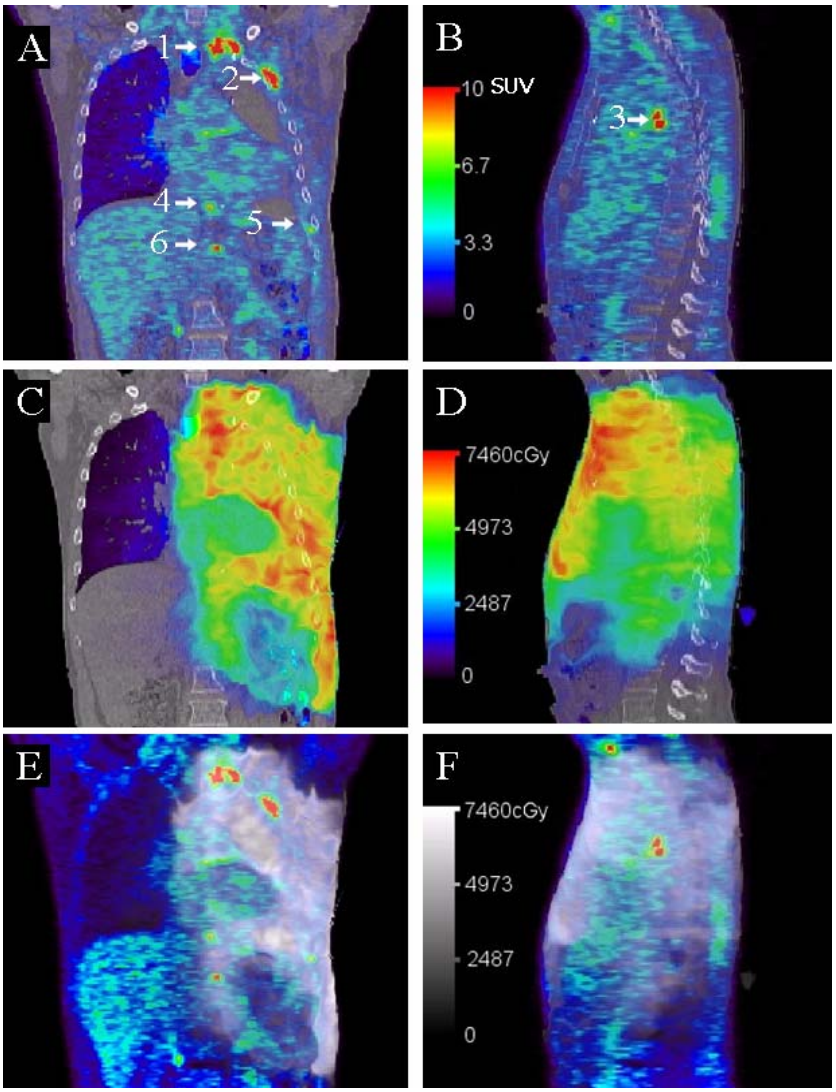

Figure 5.7: This figure shows recurrent mesothelioma. Image A shows the PET/CT with recurrence (regions 1, 2, 4, 5, and 6). Image B shows the recurrence (region 3). Images C and D show the planning

dose on pre-treatment XRT planning CT. Images E and F show the dose distribution warped with 3D OFM and superimposed on the post-treatment PET.

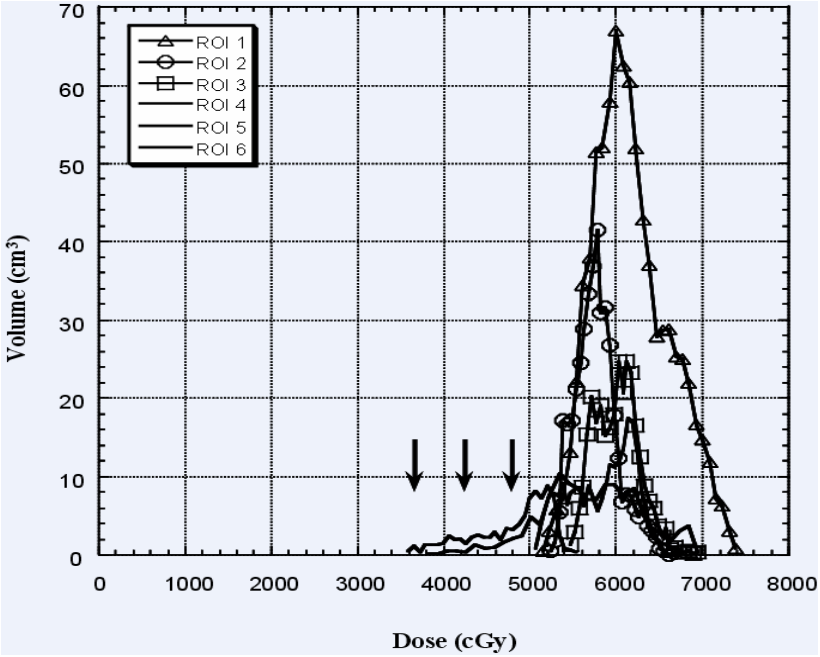

Figure 5.8: This figure shows a graph of the distribution of dose values contained within the regions identified as hypermetabolic and suspicious for local recurrence on the post-XRT PET images for case 5. Six areas suspicious for recurrence were contoured. On two of the regions there is a low dose component (see arrows) which received less than the prescribed dose of 50 Gy.

In summary, 3D OFM allowed the IMRT dose distribution to be mapped onto the post-treatment PET images in this case, where there were findings suspicious for marginal miss recurrence. A histogram analysis obtained for hypermetabolic regions on the PET images revealed that only two of the six regions had portions below the prescribed dose of 50 Gy. A biopsy for this patient is presently planned.

5.4 Discussions

Correlative studies of post-radiation therapy complications or disease recurrence may benefit from the use of the spatial information contained in post-treatment radiographic imaging studies, including PET/CT. The use of the spatial information requires an accurate spatial registration of the delivered dose with the post-treatment

imaging studies. Table 5.1 lists five spatial registration techniques described in the literature for correlative studies. Each of these methods requires meticulous intervention by the investigator to provide a best guess at image volume registration. Another difficulty in evaluating post-treatment imaging studies is that diagnostic and treatment imaging functions are performed in different clinical departments. The ideal scenario is utilization of an automated data registration process that will accurately register the multi-disciplinary data without user intervention from the involved disciplines. In this study, we demonstrated the use of deformable image registration in providing spatial registration between the post-treatment PET/CT and the radiation therapy dose. We are interested in determining the amount of radiation received by each voxel in the post-treatment images. No user intervention was required during either the imaging session or the registration process. The 3D optical flow algorithm provides a robust deformable image registration approach. An improvement in the rms error when utilizing the 3D OFM to correlate the images was observed and is provided in Table 5.3.

The rms error of image intensity may under estimate the error or improvement in image alignment, especially when there are large areas of close intensity values. For example, suppose a voxel of a CT value of 500 is mis-aligned by 5mm, and the corresponding location has the same CT number. The contribution of this mis-aligned voxel to the rms error calculated using equation is zero. This underestimation of error is less significant as the registration approaches perfect alignment. Thus, the comparison in Table 5.3 may undervalue the improvement of image registration provided by 3D OFM. A better way to evaluate the 3D OFM registration is to calculate the rms errors of displacement rather than image intensity. However, this calculation requires a priori knowledge of the displacement for each voxel. The 3D OFM used in this study has previously been evaluated by calculating rms errors of

displacement against known displacements provided by the 4D Nurbs-based cardiac-torso (NCAT) digital phantom.

One drawback when applying deformable image registration to obtain objective numerical estimations is the uncertainty regarding the error of registration when evaluating a clinical case. We have found there are situations in which the errors of registration may be larger than anticipated from the rms error. An example of this kind of error is the counterfeit structure artifact. This type of error occurs when there are large structural changes between the source and target image (e.g., due to surgery or biologic processes such as passage of stool). The artifact can be prevented by a pre-processing step that removes any new extraneous structures. We are attempting to characterize and categorize these potential sources of uncertainty. We envision a process similar to one developed for dose calculations in the thorax, in which error correction terms were introduced and algorithms were refined over many years. For the majority of cases that we have investigated, the degree of alignment is similar to the cases described in this paper. In cases that were specifically created with a known displacement, the average rms error was less than 0.2mm and the maximum error was less than 2mm. We are also searching for a parameter that may provide a numerical index of the goodness of registration without requiring a prior knowledge of the displacement between images.

The potential improved signal-to-noise ratio with a more accurate image registration may improve the sensitivity of studies to reach statistical significance. For example, Fans' study [53], in which statistical significance was almost achieved, may benefit from a more accurate registration technique. We are applying this new technique to investigate radiographic pneumonitis and disease persistence observed on post-treatment PET/CT. We intend to extend this technique to other radiological imaging modalities as well.

5.5 Conclusions

The 3D optical flow algorithm has been applied successfully to investigate radiographic pneumonitis as determined on CT and PET imaging, relating local injury with radiation dose. We have successfully determined the dose distributions in regions of local recurrence identified by post-treatment PET/CT imaging following IMRT treatment for mesothelioma. In these cases, mapping the treatment-plan dose distribution to the follow-up imaging studies provides a link between local radiographic injury and radiation dose.

Table 5.1

Method	Technique	Aligned	Criteria	Limitation	Reference
1	Manual correlation	Regional	Visual	Subjective	[6, 7]
2	6-degree of freedom, rigid body	Whole image, user defined	Visual	Subjective, distortions in anatomy	[8-13]
3	6-degree of freedom, rigid body	Fiducials	Visual or objective	Relation between inside and outside not constant, fiducials placed	[9, 12]
4	6-degree of freedom, rigid body	Lung surface	Visual	Changes in lung anatomy not accounted for	[14, 15]
5	Deformable	Whole image	Mathematical	Verification	-

Table 5.1: This table compares methods of image registration used in correlating post-treatment radiographic studies with radiation dose.

Table 5.2

Patient Number	Primary Malignancy	Clinical Finding
1	Esophagus cancer	Pneumonitis
2	Non-small cell lung cancer	Pneumonitis
3	Malignant Mesothelioma	Recurrence

Table 5.2: The three clinical cases used to illustrate deformable image registration in this study are described.

Table 5.3

Patient Number	RMS Error Before Mapping	RMS Error After Mapping
1	0.465	0.0996
2	0.235	0.0705
3	0.332	0.0864

Table 5.3: The RMS error obtained between the pre-treatment CT images and the post-treatment CT images before and after mapping the pre-treatment CT images with the displacement matrix calculated using 3D optical flow.

6. 2D Semi-Automated CT Segmentation

6.1 Introduction

The outlining of anatomic structures from computed tomography (CT) images, as part of the process of radiation treatment planning has become an issue with the advent of 3D conformal radiotherapy (RT) and intensity modulated radiotherapy (IMRT). Manual CT image segmentation of both tumor and normal anatomy has become an essential component of treatment planning. In both three-dimensional (3D) conformal treatment planning and IMRT treatment planning, anatomic structures need to be visualized in order to assist the treatment planner in determining beam geometries and treatment portals that provide target coverage while minimizing the irradiation of the normal anatomic structure. Normally, anatomic structures surrounded by tissue of similar density cannot be visualized on projection radiographs. However, these anatomic structures may be outlined on CT images, because the contrast afforded on CT images better delineates the features of the structures. Once segmented on the CT images anatomic structures are projected onto a digitally reconstructed radiograph (DRR). The delineated boundaries are also used to formulate dose-volume histograms (DVH), an important measure by which radiation treatment plans are evaluated.

6.2 Background

A major problem with outlining anatomic structures on CT images is that the procedure is done manually and is repetitive, tedious, and time-consuming. Outlines are drawn on a slice-by-slice basis, and a skilled dosimetrist may spend an hour or

longer on each case. Efficient algorithms are needed to automate this task. Although current commercial radiation treatment planning systems offer auto-contouring options and contour interpolation between slices, these tools have significant limitations. The auto-contouring algorithms used are typically based on histogram segmentation, which is also referred to as thresholding of CT voxel values. In one such algorithm, the treatment planner selects a pair of threshold CT voxel values that form boundaries for the CT values that comprise the region of interest. A point is found on the boundary of the region of interest where the threshold is crossed, and the boundary is traced all the way back to the initial point. This approach works well for anatomic structures that have CT numbers that are significantly different from the CT numbers of their surroundings and are completely surrounded by CT numbers outside of the threshold values. Examples of such structures are lungs, bones, and the exterior contour of the patient, although each of these structures may have regions for which this approach to image segmentation does not work well. This approach however does not work well for structures bordered by tissue of similar density with similar CT numbers. Contour interpolation techniques assume a similarity between the contours drawn at the bounding end images and the images between them and make no use of image content information. What is needed for the practical clinical cases is an accurate and robust automatic method of delineating soft-tissue anatomy on CT images.

6.3 Design Considerations

The purpose of this study is to demonstrate proof-of-concept for a semi-automated method of delineating regions of interest based on the techniques applied in deformable image registration. The new approach recognizes that the axial CT images used in radiation treatment planning are acquired at small intervals in the

superior-inferior direction, typically 3 to 5 mm. The patient's anatomical features do not vary in large amounts over these distances. An anatomic structure delineated on one axial CT image has a similar relationship with surrounding organs to the same anatomic structure on an adjacent slice. Consequently, a deformable image registration matrix can be generated to describe the registration of one axial CT image with the adjacent image. The elements of this matrix are two-dimensional vectors with relatively small magnitudes relating the computed displacement or flow of pixels from one image to the next.

Once this deformation matrix has been determined, the matrix can be applied to a contour of an anatomic structure delineated on one axial slice to deform the contour to an adjacent slice. This procedure can be repeated for the entire CT image data set to generate a complete set of contours for radiation treatment planning.

For the original contour, the Fourier interpolation (FI) technique is used to make this task easier and faster. Only a few critical points are needed instead of tracing the whole boundary of the region of interest.

6.4 Materials and Methods

6.4.1 Image Data Sets

Twelve different patient 3D CT data sets of entire body or pelvis, thoracic region with either 3- or 5-mm slice spacing are used for several segmentation experiments to generate lung, esophagus, heart, kidney, spinal cord, prostate, rectum, bladder, and gross tumor volumes (GTV).

6.4.2 Fourier interpolation

FI [75, 76] is used in the first contour delineation. Instead of drawing the whole contour of a structure of interest on an axial CT slice, the user needs to pick only a

few critical points that usually have high curvature along the boundary of the anatomical structure.

Figure 6.1 gives examples of Fourier interpolation using the critical sampling method. The left column of figures in Figure 6.1 shows the original shapes of the regions that need to contour, while the middle column shows the critical points selected (for Figure 6.1b, N=16; 1e, N=4; 1h, N=8), and the right column gives interpolated 32 (1c), 128 (1f), 128 (1i) points from Fourier interpolation.

Experiments on anatomical structure contouring were performed for heart, kidney and spinal cord by choosing 8, 8, and 4 critical points respectively (figure 6.1).

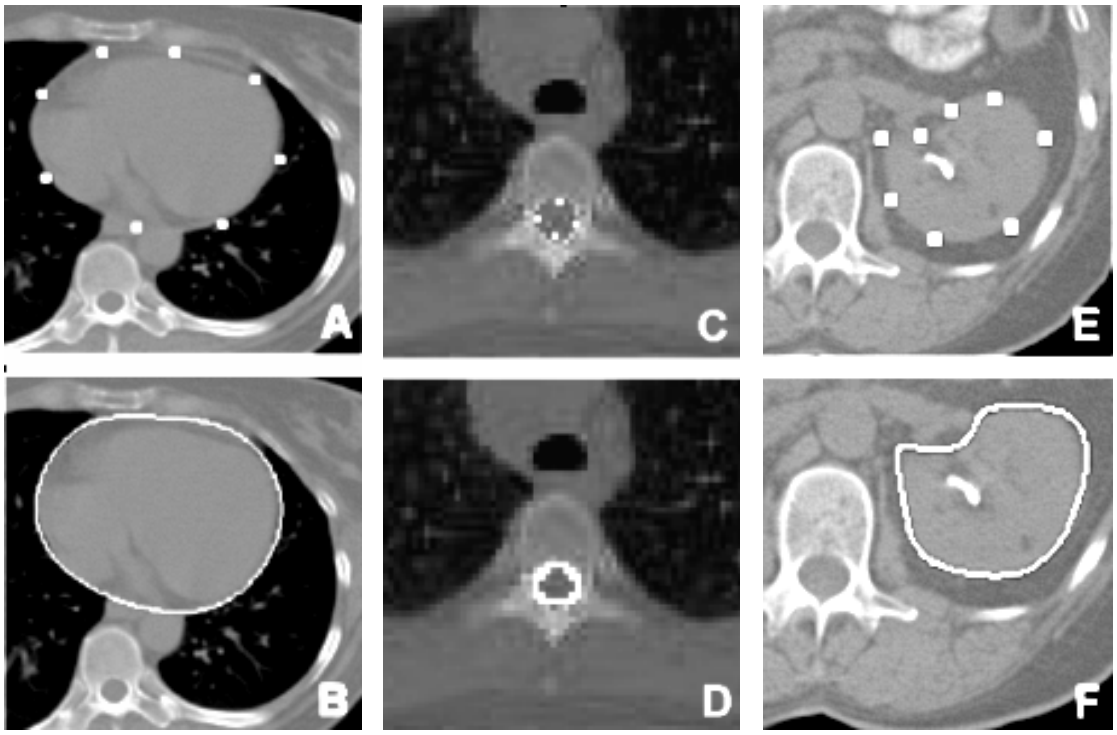

Figure 6.1: Examples of the use of the FI for contours of various anatomical structures: the left column is an example of the application for heart contouring, while the middle for spinal cord and the right for kidney. Contrast has been enhanced in images (E) and (F) to permit visualization of the edges of the organ of interest.

6.4.3 Optical Flow

The present study uses a deformable image registration algorithm based on the optical flow (OF) method. A gradient-based method was chosen from a variety of optical flow algorithms [19]. This method implicitly requires small displacements. To apply the optical flow formalism to evolve structure contours, the transition from one axial CT image, which we will refer to as the “source image,” to an adjacent image, the “target image,” is viewed as an evolution over time.

6.4.4 Image Registration and Contour Mapping

An original contour was delineated by selecting some initial critical points and employing the Fourier interpolation method. Next, the images from adjacent slices in each image volume were registered utilizing the 2-D optical flow software creating a pixel-by-pixel displacement vector field for each adjacent image. The registration requires a source image and a target image with the same numbers of pixels in both the x and y directions. As the source image was registered to the target image, a pixel-by-pixel velocity matrix was created based on the registration between two adjacent slices. This velocity matrix was used to deform the contour of the anatomic structure of interest on the source image to the target image. The contour points were re-sampled to provide equal spacing of the points around the contour set at one point per three pixels. Figure 6.2 illustrates the flow diagram required to transform contour points from a source 2-D CT image to the adjacent target image. The deformed contour was then used as the source contour for the next round of registration to the next adjacent image, which became the new target image. This procedure was repeated for as many slices as long as no topological limitations were reached. Figure 6.3 demonstrates an example of OF image registration, where figure 6.3(a) was the source image, 6.3(b) target image, 6.3(c) gives the difference between the source and

the target images, 6.3(d) displays a velocity matrix from the source image to the target, 6.3(e) was the deformed image applied by velocity matrix and 6.3(f) shows the difference between estimated image and the target image.

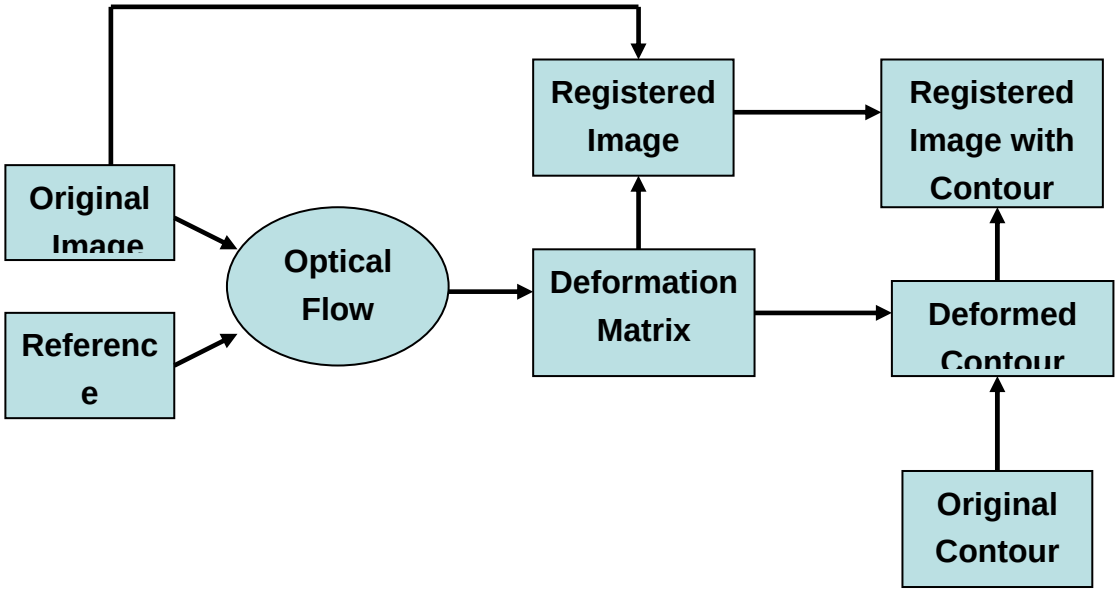

Figure 6.2: Flow diagram illustrating contour deformation from one image to an adjacent image using optical flow.

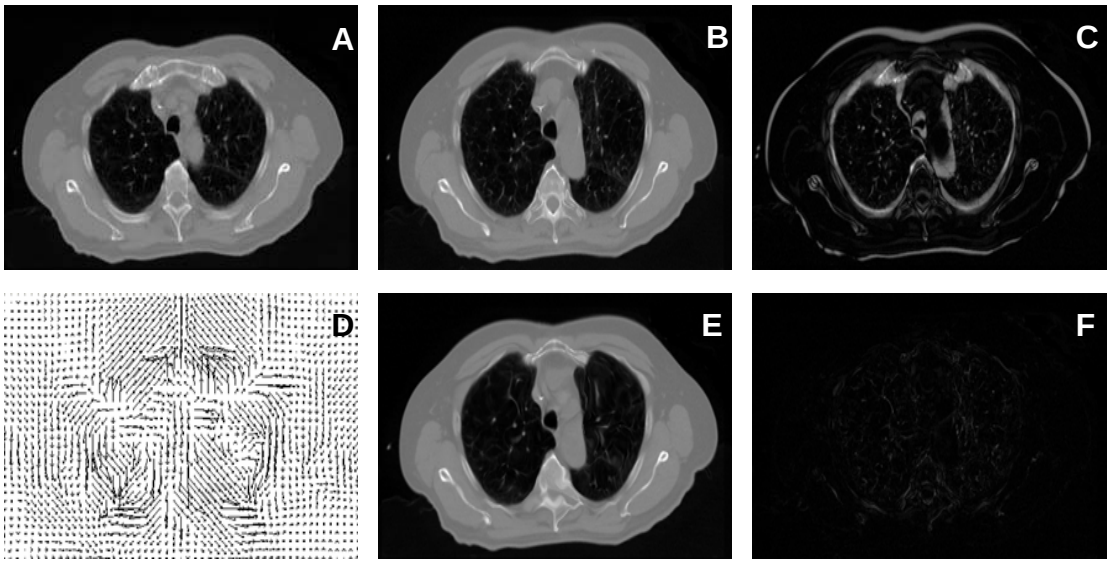

Figure 6.3: Example of image registration from (A) original image to (B) reference image. The original image and the reference image are adjacent slices from a CT scan. The thickness of the slice is about 3mm. The difference between the original and the reference images is shown in (C). The deformation matrix is shown in (D). The registered image is shown in (E). The difference between the registered image and the reference image is shown in (C), which shows little difference in the anatomy structures.

6.4.5 Multi-Resolution

Originally, one limitation of the optical flow method was that large variations in images on adjacent slices would cause problems in the deformable image registration. As a consequence, the separation of the CT slices used in the registration could not be too large. For the thoracic CT image data sets with a standard slice separation of 3 mm, slice-by-slice registration usually does not encounter problems of large image changes between adjacent slices. However, multi-resolution is the solution to larger displacement problems. If the image size is subsampled to a twofold lower resolution in one dimension, a two-pixel displacement in that dimension becomes one pixel. Optical flow can thus start from a much lower resolution image subsampled from the original and continue the registration with increasing resolution until the original image resolution is reached. In this way, large displacements are no longer an insurmountable problem. This feature is useful when the CT data sets have a large slice separation. The implementation of multi-resolution in the optical flow program that we use for the 2D contouring project has not only improved the quality of the registration, and thus the contour mapping, but has also yielded a new method of contour propagation.

Without multi-resolution, to avoid the problem of large displacements, the contour is propagated slice by slice in the way that the mapped contour from the previous slice becomes the original contour for next slice mapping. Although the difference between the registered image and the reference image is usually very small, as shown in Figure 6.3, the accumulated error of the velocity matrices occasionally becomes large after a few slices. As a result the mapped contour appears off the boundary of the anatomy structure of interest.

With multi-resolution, one can register a slice to another slice of the image volume that is far apart. In this manner, the contour can be mapped directly to a

distant slice. This implies that a drawn contour can be directly mapped to many slices that are not adjacent to the one containing the original contour. For example, if the original contour is on the 60^{th} slice, it can be mapped directly to the 70^{th} slice. The same original contour on the 60^{th} slice is also mapped to all the intervening slices. In all these mappings, only the drawn contour is used as the original contour. Figure 6.4 shows an example of a left lung contour directly mapped to a slice that is 15 slices apart from the slice that is with the original contour. In this example, the slice thickness is 3 mm. This direct mapping technique has the advantage of minimizing the accumulated error and maintaining the contour on the boundary of anatomic interest. The quality of the mapping depends only on a single calculation and not an accumulation of previous calculations.

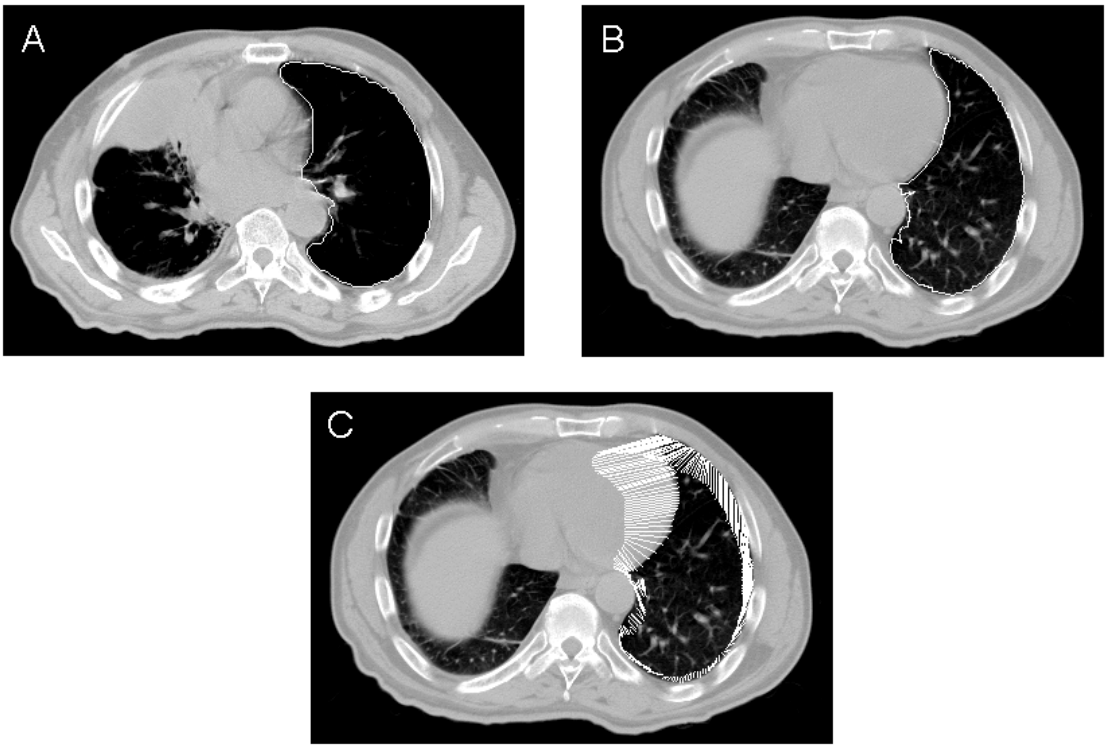

Figure 6.4: An example of the deformable image registration moving the contour of the left lung from an original axial slice (A) to the slice that is 15 slices apart from the original slice (B). (C) illustrates the deformation vectors.

The multi-resolution feature in the 2D optical flow program starts the mapping from a user-selected resolution level that is 2^n fold of the original resolution. For example, for a CT image with 512 × 512 resolution, one can start from a 64 × 64 resolution. The program sub-samples the 512 × 512 original and reference images to 64 × 64 images by averaging every 8 × 8 region to a single pixel. After the 64 × 64 mapping, the program then expands the resulting 64 × 64 velocity matrix to a 128 × 128 matrix with either linearly interpolated or equal value replication. Next, the enlarged velocity matrix is applied to the 128 × 128 image subsampled from the original 512 × 512 to make a deformed 128 × 128 image as the original image. Finally, the new deformed image is registered to the 128 × 128 subsampled reference image. The process is repeated until the original 512 × 512 resolution is reached. We found no significant difference between using linear interpolation versus equal-valued replication as the expansion technique for the velocity matrix.

6.5 Evaluation

The maximum distance between the generated and manually drawn contours in units of pixels is calculated as follows: First, calculate the distances in units of pixels between each generated contour point and all the manually drawn points and then search for the minimum distance. This minimum represents the distance between that point and the closest point on the manually drawn contour. The maximum value of the minimum distances for all the generated contour points is then used as a measure of the maximum distance between the two contours.

The relative volume error is defined as the ratio of the non-overlap volume of the two contours to the volume of the union of the two contours. Thus the extreme values of the relative volume error are 0 if the two contour sets are identical and 100% if there is no overlap at all. This is stricter than the straight volume ratio of the two

contoured volumes since the relative volume error takes into account any special offset between the two volumes while the straight volume ratio does not.

6.5.1 Automatic Contour Mapping

The optical flow program has been used to register contours for different anatomical structures and tumor volumes, including lung, esophagus, heart, spinal cord, carina, kidney, prostate, bladder, rectum, and a liver tumor. The liver tumor was chosen because of its difficulty for other automatic contouring methods due to the low density contrast between the tumor and the normal liver tissue. Figure 6.4 displays an example of the contour mapping using deformable image registration for the left lung from an original axial slice (A) to the slice that is 15 slices apart from the original (B), and 6.4(C) illustrates the deformation vectors.

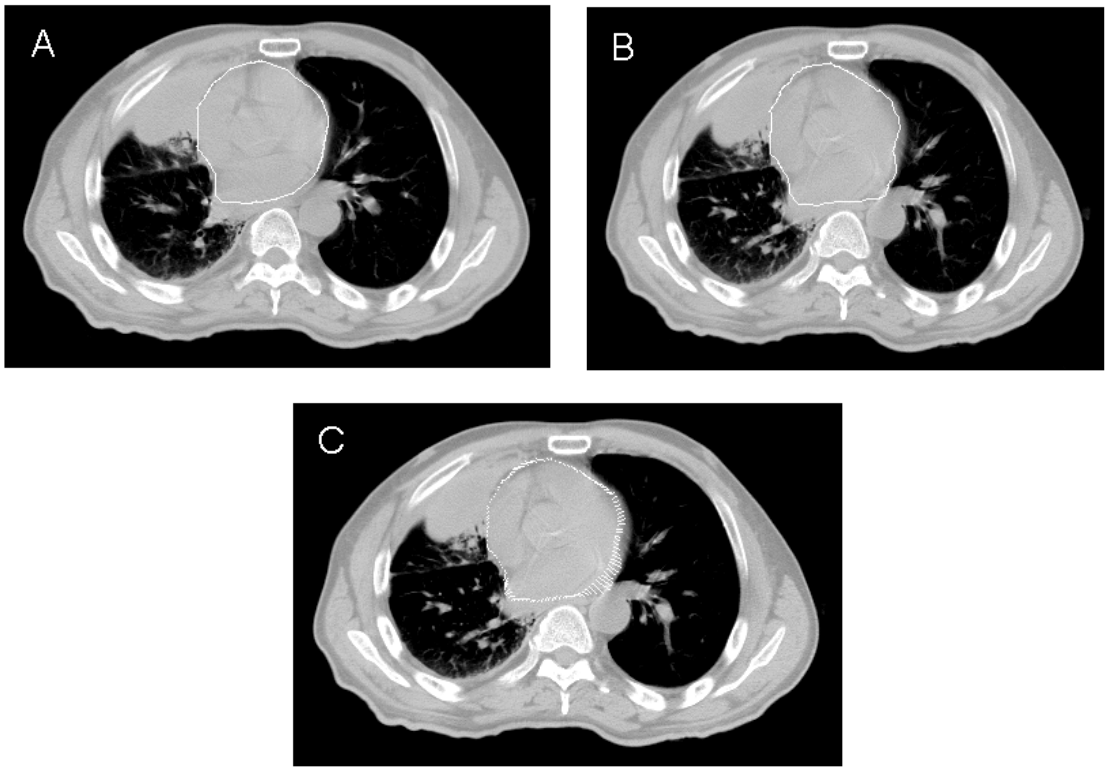

Figure 6.5: An example of the deformable image registration moving the contour of the heart from an original axial slice (A) to the adjacent slice (B). Fig .(C) illustrates the deformation vectors.

Figure 6.5 shows an example of heart contour registration on a patient's CT data set. Qualitative review of the contour in Figure 6.5(B) indicates a good fit of the contour to the CT image of the heart. It is noticeable that the contour change in figure 6.5 is much smaller than that in figure 6.4. In figure 6.5, the heart contour is mapped to an adjacent CT slice while in figure 6.4 the left lung contour is mapped to a slice that is 15 slices apart. Figure 6.6 illustrates a set of esophagus images with contours propagated. All the images are parts of a set of 512 × 512 CT images. A relatively large number of slices that a single original contour is propagated through are displayed in this figure to show the robustness of the optical flow registration. Usually, esophagus auto-contouring is a very difficult, if not impossible.

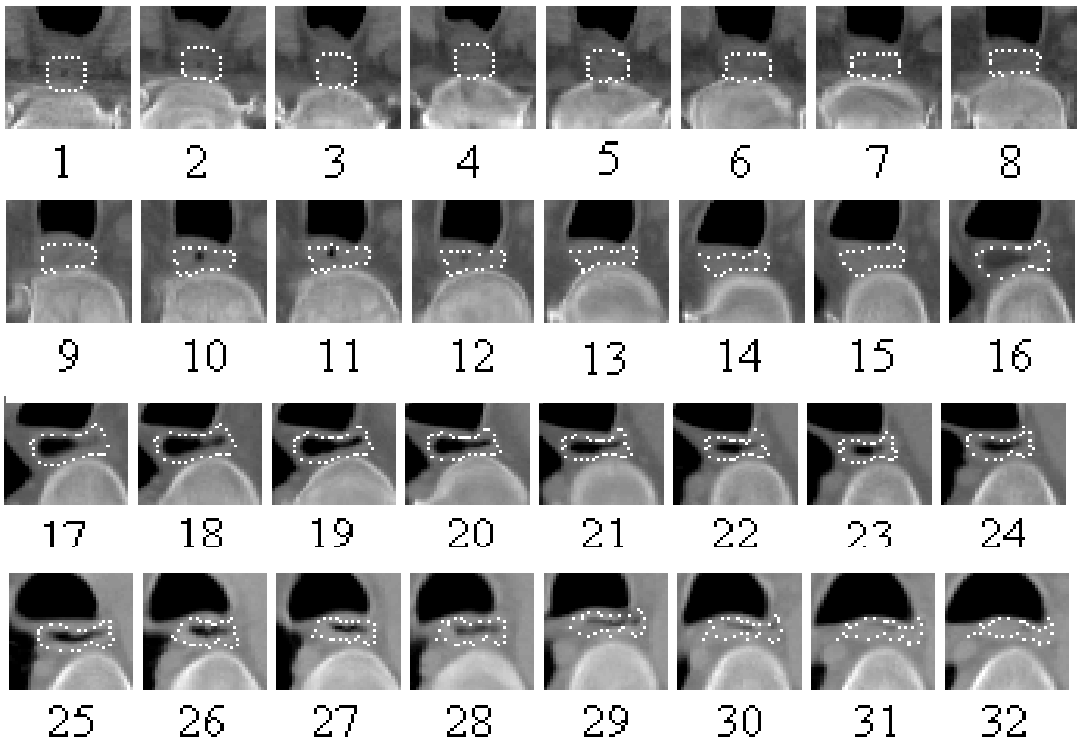

Figure 6.6: Esophagus contours propagated through 32 axial CT images by deformable registration using the OF. The contour on the 1st slice is the only contour delineated manually. Contrast has been enhanced in these images to permit visualization of the edges of the organ of interest.

6.5.2 Comparison with Manual Contouring

The contours generated by the program were recognized and accepted by physicians and dosimetrists. Experiments were designed to compare the program generated contours with manually drawn contours. A skilled dosimetrist and a physician drew contours of different anatomic structures and tumors. The mapped contours were then compared with the drawn contours. Figure 6.7 and figure 6.8 shows the results of the comparison of two cases, right kidney and liver tumor respectively, in which the dotted lines were contours delineated by the dosimetrist (the kidney case) and the physician (the liver tumor case) and the solid lines mapped by the program, starting with Fourier interpolation of 4 critical points in slice 1.

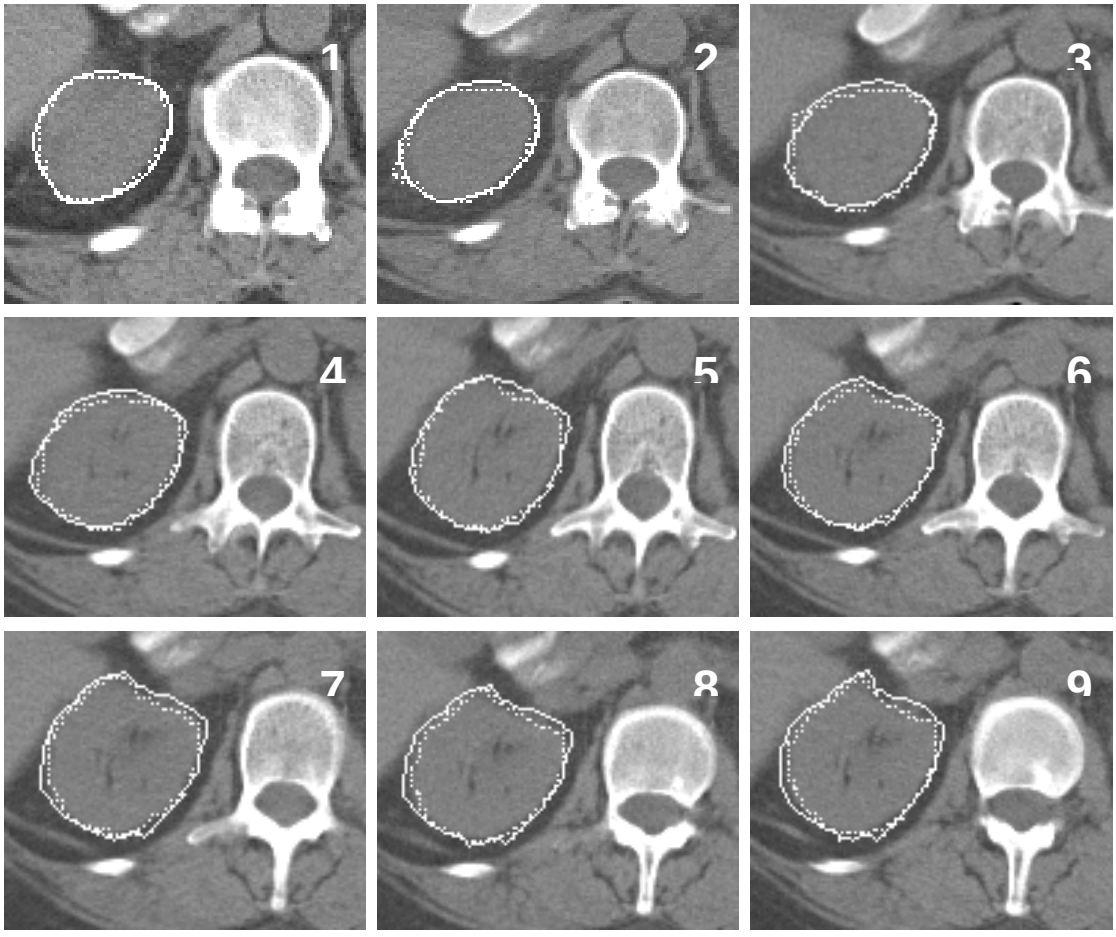

Figure 6.7: The comparison between contours of the right kidney drawn by a skilled dosimetrist (dotted lines) and contours generated by the program (solid lines). The maximum difference between

the drawn and generated contours for 10 slices of propagation was 5 pixels, or 5 mm. Contrast has been enhanced in these images to permit visualization of the edges of the organ of interest. Contrast has been enhanced in these images to permit visualization of the edges of the organ of interest.

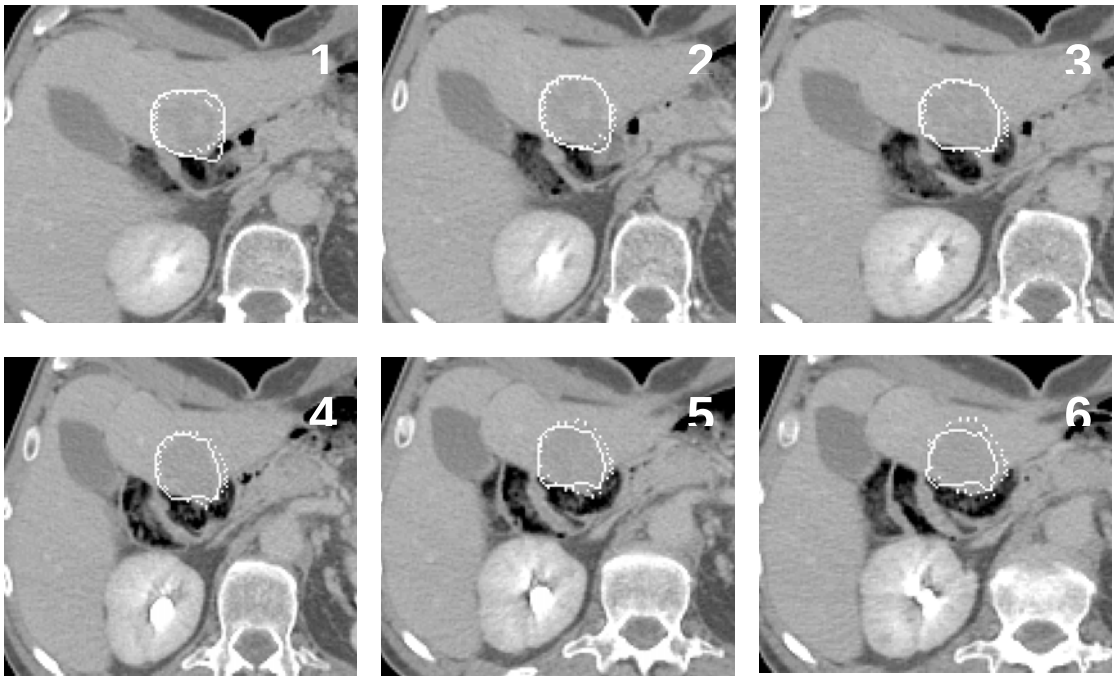

Figure 6.8: In this liver gross tumor volume (GTV) case, the maximum difference between the drawn contours by a physician (dotted lines) and the generated contours by the program (solid lines) was 6 pixels, or 6mm, after 6 slices of mapping. Liver tumor GTV is usually difficult to automatically contour because of the low density contrast between the GTV and the surrounding normal liver tissue. Contrast has been enhanced in these images to permit visualization of the edges of the organ of interest.

In these two cases, the maximum differences between the drawn and the generated contours were 5 and 6 pixels respectively, which are typical differences one would see between contours drawn by different physicians / dosimetrists. Contours of other anatomic structures, such as prostate, rectum, bladder, were also tested. The relative volume errors were 2.6% in the liver tumor case, 7.5 % in a prostate case, and 8.5% in a rectum case. As a reference, the relative volume errors for the prostate and rectum cases were also calculated on two contour sets drawn by different dosimetrists. The errors were 18.6 % for the prostate case and 16.1% rectum.

6.6 Discussion

The technique for contour propagation described in this paper appears to work successfully, provided the contour in the target slice is similar in compositions as the image in the source slice. However, if a contour is bifurcated, the topology of the contour changes at the point of bifurcation, and correct contour propagation is not possible. Figure 6.9 shows an example of this kind of failure. The original contour of the carina is delineated on Slice 1, and the contour has been propagated through Slice 4 without a problem. A problem occurs at Slice 5, where bifurcation takes place. The bifurcation of the carina is not reflected in the target contour. This kind of propagation failure also happens on slices where the anatomy of the structure of interest ends. Gas in the rectum also causes this kind of failure if an image with gas in the rectum to an image without gas, but this issue is outside the scope of this paper.

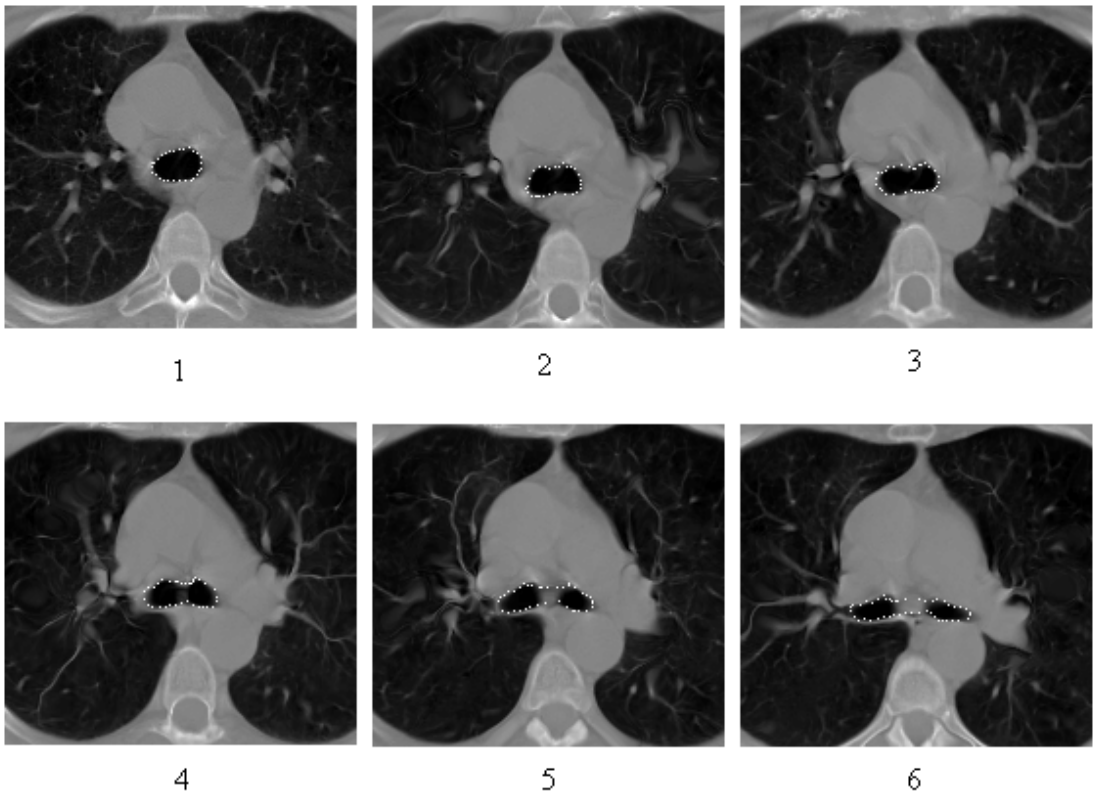

Figure 6.9: Example of a contour propagation failure where topological changes in the anatomic structure occur. In this example, the bifurcation of the carina occurring between Slice 4 and Slice 5 is

not accurately represented in the propagation.

To avoid this kind of registration failure, it is suggested that the contours be manually delineated on a few slices throughout the anatomy of the structure of interest. The program then propagates the contours on both directions to fill the remaining slices. If a topological change occurs between the manually delineated contours, the program still can propagate the contours from opposite directions and meet where the change takes place. In this way, it is not necessary to select the slices where topological changes occur to manually delineate the contours in order to avoid registration failure. Manual delineation of contours on a sparse subset of CT images is also a good method to use to avoid error accumulation due to propagation of errors in the deformation matrix that may magnify any error of the original contours delineated manually. The method of sparse manual contouring combined with bi-directional propagation is illustrated in figure 6.10. Alternatively, one could use the program to generate a series of contours. Upon review of the automatically generated contours, one could delete those contours that were generated after the topological change, enter one such contour manually, and then rerun the program from the point of topological change.

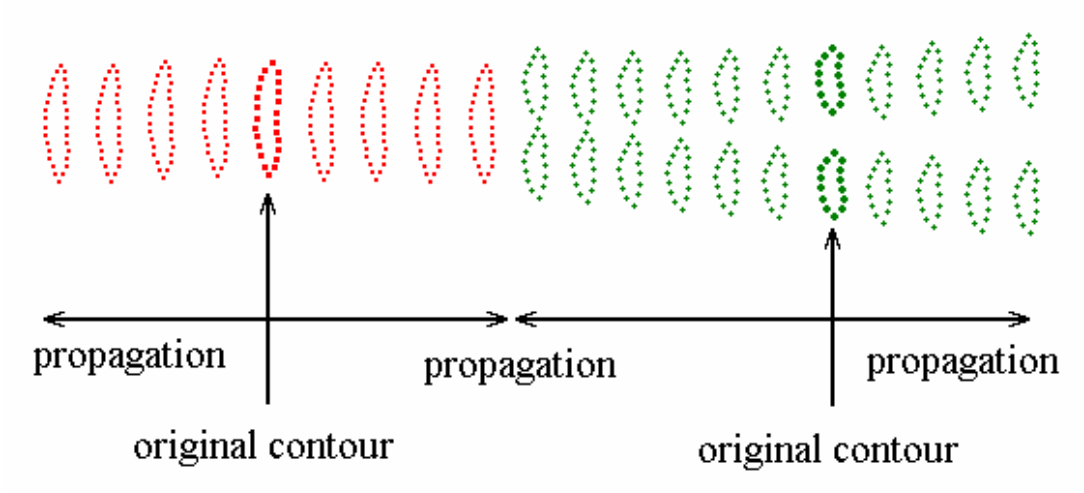

Figure 6.10: In order to resolve the problem of topological changes in contour propagation, contours

are delineated manually in a sparse subset of slices and then propagated in both directions using the OF. If a topological change occurs somewhere between the original manually delineated contours, the propagation stops before the change takes place

Although directly mapping contours between slices that are far apart is usually more accurate than slice-by-slice propagation, this approach is more likely to encounter the problem of topological change. It finds its best application in lung contouring, simply because the lung is such a large region of large density difference from its surroundings that the program can hardly be confused by small topological changes in other parts. For other small structures, especially esophagus, in which some slices have gas and some do not, slice-by-slice propagation is still the best approach.

An automatic segmentation method is only practical and worthwhile implementing if it generates contours comparable with those generated manually. Previous studies have demonstrated some variation in manually generated contours, especially for situations where decisions have to be made by the individual performing the contouring. Whereas the lung-soft tissue boundary is relatively unambiguous, for soft tissue anatomic structures surrounded by soft tissue, there may be some variation among various individuals as to the exact nature of the boundary of the anatomic structure [10]. The method described in this paper usually propagates the contours with loyalty to the original contours. If the original contours delineated manually contain errors, which are very likely in cases of soft tissue structures surrounded by soft tissue, the errors are carried on and could be magnified in a few slices of propagation. In this sense, the contour mapping quality still somehow depends on how accurate the original contours are delineated.

6.7 Future Plans

The use of the FI and OF to generate deformable image registrations has been shown to aid in the automatic delineation of contours of anatomic structures. This technique has been shown to be particularly useful for the delineation of soft tissue structures surrounded by soft tissue, a situation that has been difficult to segment by other methods [77]. There is one limitation that makes the application of the present method difficult to be completely automatic: contours must be topologically similar to each other for accurate progression from CT slice to CT slice. Currently the solution to bifurcated contours is to map in both directions. To eliminate this problem and make this technique completely automatic, a new version of the software that can handle such topological change between slices is in the future plan.

7. 3D Optical Flow Method Implementation for Mapping of 3D Anatomical Structure Contours across 4D CT Data

7.1 Introduction

Tumors in thorax, such as lung, esophagus and liver cancers, move as patient breaths. Due to respiratory motion, the dose delivered to the tumors in radiotherapy treatments may not be the same as planned [33]. Although many techniques are currently used clinically to reduce the effect of respiratory motion on the dose delivery accuracy, such as gating [35], active breathing control [36], the problem is not satisfactorily solved with respect to dose accuracy and patient comfort during treatments. 4D treatment planning and dose delivering has been proposed to overcome the tumor motion problem resulting from respiratory motion [78]. A treatment plan would include multi-phase sub-plans (e.g.,) that are based on a patient's CT scans of different respiratory levels. A tracking system would detect the patient's respiratory phase during treatment. And the treatment system would determine which sub-plan to use based on the tracking system's feedback. To realize 4D treatment planning and dose delivering, 4D CT scans would be acquired [79].

In 3D conformal radiotherapy or intensity modulated radiotherapy (IMRT) planning, contouring normal anatomical structures is needed to define treatment fields and calculate dose distributions. In conventional 3D treatment planning, normal anatomical structures only need to be contoured once. In 4D treatment planning, which essentially consists of multi-phase 3D planning, many sets of CT scan data are involved. Since, like tumors in thorax, normal anatomical structures also change with respiratory motion, one set of the contours of the anatomical structures would not fit

all of the involved images. Time to manually contour these structures for 4D treatment planning is far more consuming than for traditional 3D treatment planning. To save physician's time, we propose the use of a deformable image registration algorithm based on an optical flow method to assist in the contouring process.

7.2 Materials and Methods

7.2.1 3D Optical Flow

An optical flow calculation requires input of a source image and a target image. The output from the calculation includes the 3D velocity matrix data file equal to each voxel's displacement and an estimated image to assemble the target image.

7.2.2 4D Image Data

Two sets of 4D CT image data sets were used in this study. One set was acquired from a patient involved in an I.R.B.-approved clinical protocol, while the second set was acquired of a thoracic phantom, Radiological Physics Center (RPC) [17] placed on a table that allowed programmable 1D motion. The 1D motion was set in the superior-inferior (SI) direction at 18 cycles per minute with a motion distance of 17.5 mm to simulate respiratory motion. All data sets were acquired on a commercial multi-slice helical CT scanner (MX8000 IDT, Philips Medical Systems). A video camera monitored the marks attached to the patient's chest or the anterior top of the phantom to provide gating signals. The system reconstructed the CT data and binned the data into different respiratory phases according to the associated gating signals after the data acquisition was completed. Usually, 8 phases per respiratory cycle were reconstructed.

A physician contoured the anatomical structures on one of the 4D data sets, usually the set obtained at end expiration. The original contours were then elastically

mapped to all of the image sets of other respiratory levels, using the velocity matrices calculated from the image registration between the contoured imaging set to other sets using optical flow. Only the mapping between the extreme phases (end expiration and end inspiration) are shown and discussed in this paper. The displacements between the extreme phases are largest.

7.3 Results and Discussion

Optical flow was applied in structure contour mapping for the 4D gated CT scan data of the RPC thoracic phantom on a motion table that moved in one direction repetitively. In this case, only 1D translation was involved. Contours of lungs, heart and spinal cord were mapped from the contoured image to all other images. Figure 7.1 shows an example of heart contour mapping in coronal view. The contour follows the phantom motion precisely. The displacement of each voxel inside the contours was calculated using the velocity matrix. Figure 7.2 shows the histogram of the right lung displacement. The estimated RMS SI displacement of the contoured volume agrees with the known displacement very well. The estimated RMS SI displacement for the right lung was 16.8 mm while the SI displacement of the two CT scans was 17.5 mm. The RMS SI displacement was determined using the following equation:

$$Displacement(SI)_{RMS} = \sqrt{\frac{\sum_{i=0}^{N}\left(z_i^{original} - z_i^{mapped}\right)^2}{N}}$$

where N is the total number of voxels inside the contoured right lung, $z_i^{original}$ and z_i^{mapped} represents the z coordinate for the i^{th} voxel in the original image set and in the mapped image set respectively.

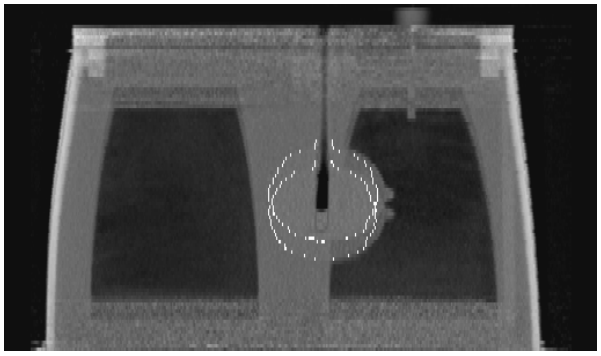

Figure 7.1: Overlaid coronal view of original and mapped heart contour images of the RPC phantom.

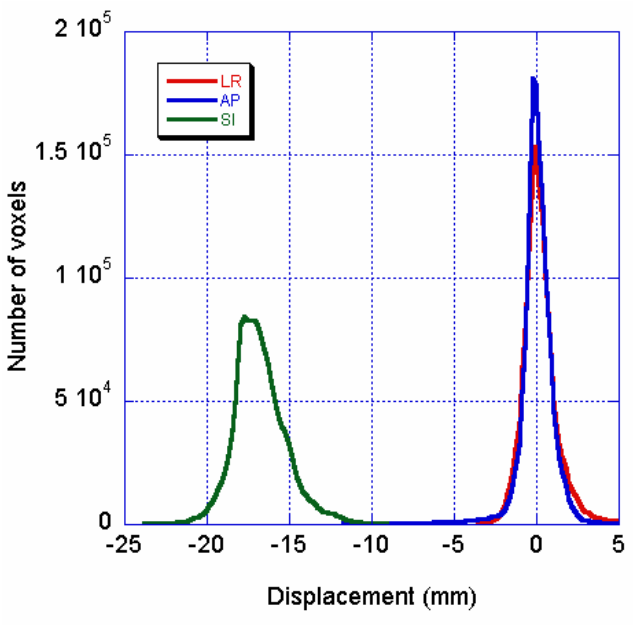

Figure 7.2: Histogram of calculated displacement in contoured right lung in the RPC phantom based on the 4D CT scans. The motion distance is 17.5 mm in SI direction.

To investigate contributions to the errors between the real and calculated displacements, another optical flow calculation was computed: one phantom image set of the motion phases was shifted by 8 slices in SI direction, thus making a displacement in SI direction of 24mm (no displacement in LR and AP directions). Optical flow was then used to register the original image to the shifted image; the resulting deformation matrix was used to map the contour of the right lung from the original image to the shifted image. The histogram of calculated displacement in the

contoured right lung is shown in Figure 7.3. The RMS SI displacement is 23.93 mm, while the shifted distance is 24.00 mm, a difference of 0.07 mm. The bases of the peaks were also much smaller than those in Figure 7.2. By comparing Figure 7.2 and 7.3, we can conclude that the errors in the 4D CT data mapping primarily resulted from the residual motion in the 4D CT scans and the shaking of the motion table during motion.

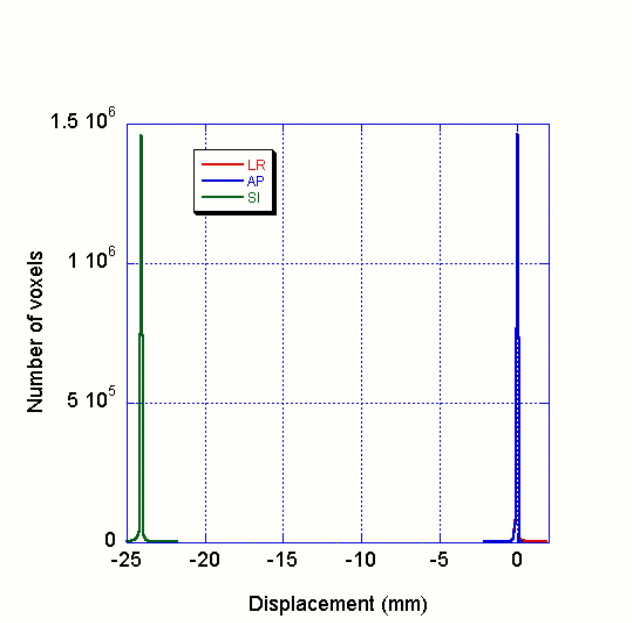

Figure 7.3: Histogram of calculated displacement in contoured right lung in the RPC phantom based on the shifted phantom images. The shifted distance is 24mm in SI direction.

Even with the errors that are not contributed by the optical flow calculation, the difference between the calculation and reality for the 4D CT scans (0.07mm) is quite reasonable considering that the CT slice thickness is 3mm.

Due to the lack of intensity variation inside the phantom lung, the aperture effect [19] introduces some displacement errors for some voxels. The difference between the calculated and the shifted motion distance is caused by the aperture effect.

A set of real patient data is also included in the study. Contours of lungs, esophagus and lung tumor are mapped from the end expiration image to the end

inspiration image. Figure 7.4 shows an example of the esophagus contour mapping, and Figure 7.5, the right lung. Note, in particular, the accuracy of the lung contour obtained without the use of thresholding methods. Figure 7.6 gives an example of lung tumor contour mapping.

A. original esophagus contour on end of expiration CT data

B. mapped esophagus contour on end of inspiration CT data

Figure 7.4: Esophagus contour mapping from end expiration to end inspiration CT images using optical flow. Both sets of the images shown in this figure are selected from the same location in the image coordinate system. They are not exactly the same anatomical location.

Although occlusion and transparency are problems for 2D optical flow calculation, which cause motion discontinuity, they are not problems in 3D optical flow calculations using CT images. However, there are other sources that cause motion discontinuity in calculations using 3D CT images. For example, in registering daily CT images for prostate cancer patients, if there is gas in the rectum in one image set while there is no gas in another image set, the registration could yield an incorrect

result for that region. Although this is not an issue in 4D CT registration as discussed in this paper, it is a problem in other applications. A possible solution to this problem

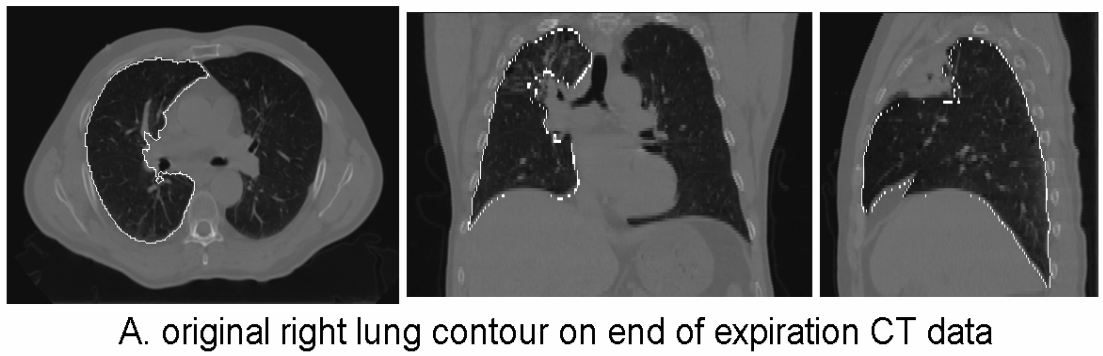

A. original right lung contour on end of expiration CT data

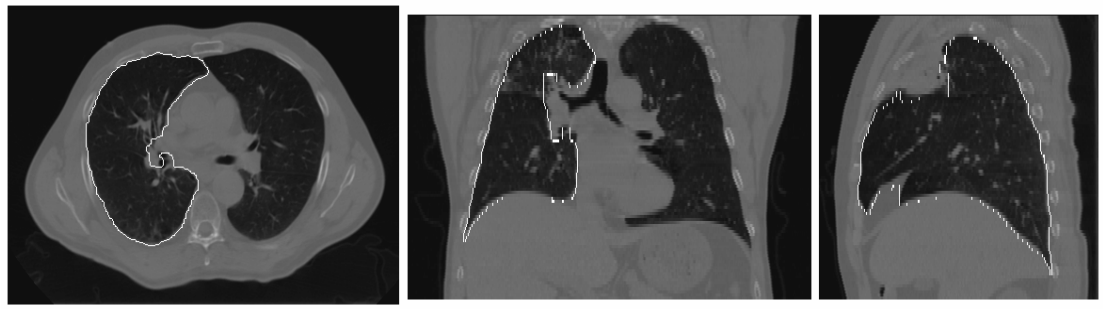

B. mapped right lung contour on end of inspiration CT data

Figure 7.5: Right lung contour mapping from end expiration to end inspiration CT images using optical flow. The image sets shown in this figure are at the same location in the image coordinate system, but are not exactly the same anatomical location.

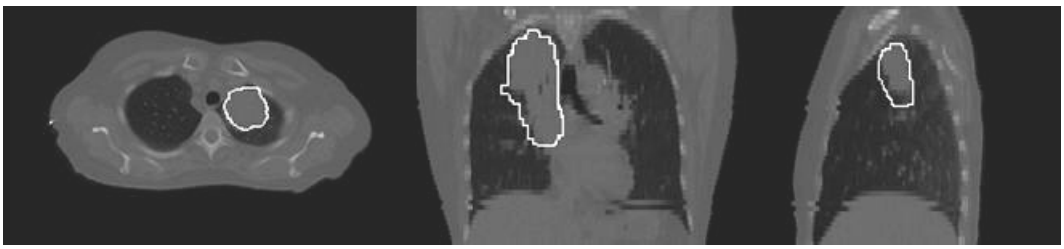

A. Original lung tumor contour on end of expiration CT data

B. Mapped lung tumor contour on end of inspiration CT data

Figure 7.6: Lung cancer GTV contour mapping from end expiration to end inspiration CT images using optical flow. The image sets shown in this figure are at the same location in the image coordinate system, but are not exactly the same anatomical location.

is to implement the multiple motion methods of the 3D optical flow program, which have been successfully implemented in 2D optical flow programs (see the discussion in Chapter 3).

The aperture effect in optical flow algorithms introduces errors in the local volume due to a lack of intensity variation. Although this is rarely a serious problem in 3D contour mapping, since the contours are typically sitting on the edges where intensity changes more significantly than surrounding volumes, the aperture effect decreases accuracy when applying optical flow calculation to map an interested volume in which there are local flat intensity regions. It has been demonstrated that the aperture problem can be resolved by introducing the 2^{nd} or even higher order intensity derivatives into the optical flow constraint equations. The 3D optical flow program applied in this study only uses the first order intensity derivatives in the optical flow equations. There is room to improve the accuracy by using higher order intensity derivatives when it is necessary. This approach would slow down the calculation as a trade off.

7.4 Conclusions

A deformable image registration matrix describing the deformation of a 3D CT image data set from one phase of the respiratory cycle to the other, obtained by use of an optical flow algorithm, can be used to generate a set of contours of normal anatomic structures in all phases of a 4D CT image data set.

8. Intrathoracic Tumor Motion Estimation from CT Imaging

8.1 Introduction

Measuring intrathoracic tumor motion via imaging techniques has become a new focus of study. In each of the methods described in these studies, thoracic tumors are manually delineated on all images to provide an estimate of the tumor boundaries and their range of motion during normal respiration. The change in shape of the manually delineated tumor boundary determines the tumor motion estimate.

The motion is reported as either the change in position of the center of mass, centroid location, or the boundaries of a bounding box. Alternatively, a radio-opaque fiducial marker implanted in close proximity to the tumor may be used to represent the tumor motion [5, 7]. The fiducial can be localized using image analysis techniques and tracked during treatment. Four dimensional (4D) CT imaging will generate eight or more CT image volumes to represent the tumor throughout the respiratory cycle. Manual delineation of each of these CT image volumes is laborious and a source of error. Significant interobserver and intraobserver variations in tumour CT segmentation have been observed when manual segmentation is applied repeatedly to the same subject CT image set. Finally, tumour-surface delineation does not provide a point-to-point correspondence between tumour volume elements at expiration and at inspiration.

The optical flow method (OFM) has previously been applied to intrathoracic motion. Song and Leahy used OFM to measure motion between CT imaging frames for cardiac wall motion analysis [61, 62]. Klein and Huesman (2002) utilized OFM to add the 3D component PET images from a 4D acquired PET study into a single

composite 3D image set. With OFM, the image content properties are used to generate a displacement vector between each voxel in the reference image to the target image. The displacement vector map obtained for each voxel in a CT image volume is used to map a delineated tumour from one CT image volume to the next on a point-by-point basis. The boundary of the mapped tumour volumes represents the new tumour contour on the target CT images or alternatively the surface points can be mapped. This paradigm can be applied to pairs of breath-hold (BH) CT image volumes or potentially to a complete 4D CT image sets equally well. The tumour target is manually or otherwise delineated on a reference CT image volume, and both the surface and contained volume are mapped to the additional CT volumes. The collection of displacement vectors for the surface or volume represents the motion of the tumor. We developed and validated a 3D OFM to measure intrathoracic tumour motion from inspiration/expiration BH CT image sets. Here, we describe how this technique is applied to two clinical cases.

8.2 Materials and Methods

8.2.1 Patient CT Data

The treatment planning CT images from patients for whom breath-hold CT image sets at inspiration and expiration were obtained as part of their radiotherapy planning were utilized following an Institutional Review Board approved retrospective protocol. One esophageal cancer case and one non-small cell lung cancer case were selected. The radiation oncologist delineated the gross tumor volume contour for each case.

8.2.2 Motion Estimation Method

One esophageal cancer case and one lung cancer case consisting of expiration and inspiration breath-hold CT image sets obtained as part of the radiotherapy treatment planning were evaluated. A radiation oncologist outlined the gross tumor volume for each case on the expiration CT images. 3D OFM was utilized to obtain the displacement field from the expiration to the inspiration CT image sets. The contour and contour contents were mapped from the expiration CT image set to the inspiration CT image set. Histograms of the tumor surface displacement and the tumor volume displacement were created.

8.3 Tumor Motion

8.3.1 Esophageal Tumor Motion

An esophageal cancer case involving the gastro-esophageal (GE) junction was evaluated in this study. The tumor was delineated on the exhalation CT image volume (Figure 8.1(A)). The 3D OFM algorithm was applied between the exhalation and inhalation image volumes to calculate the displacement vectors. A projection of the displacement vectors on a midsagittal image is shown in figure 8.1(B). The points contained within the tumor outline on the exhalation image were mapped from the exhalation image to the inhalation image, and the resulting contour is shown in Figure 8.1(C). The mid-sagittal exhalation image with both sets of contours overlain is shown in Figure 8.1(D). This would constitute the range of tumor motion under normal respiration. A histogram of the displacement of the tumor volume is shown in Figure 8.2. The majority of the displacement occurs in the superior–inferior direction, with up to 1.4 cm of esophageal tumor surface motion observed near the distal end. The OFM displacement vectors are applied to the tumor contours drawn on the

exhalation CT images to produce tumor boundary estimation on the inhalation CT image volume. The derived tumor contour is shown in Figure 8.1(D) in dots superimposed on the exhalation CT sagittal image and physician-contoured exhalation tumor outline (solid).

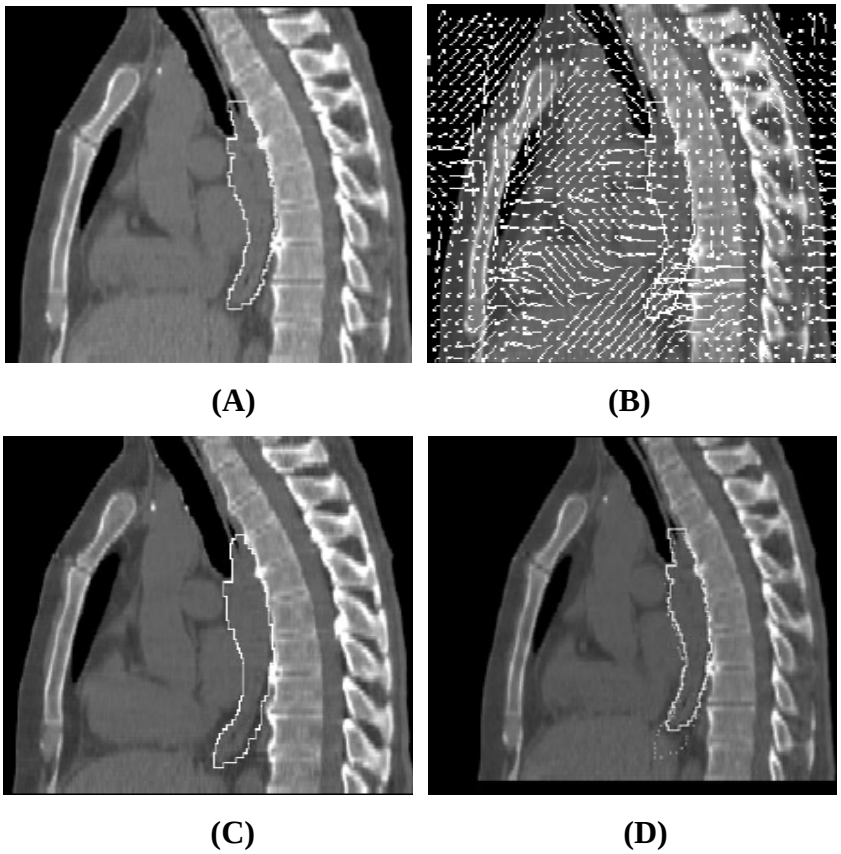

Figure 8.1: (A) Mid-sagittal section through end-expiration BH CT volume of an esophageal tumor. The physician-contoured tumor outline (solid line) is shown. (B) Same mid-sagittal section as in (A) with the 3D OFM displacement vectors superimposed. (C) Mid-sagittal section through end-inspiration BH CT volume with the tumor volume from (A) mapped using the displacement vectors in (B). (D) Same mid-sagittal section as in (A) with the physician-contoured (expiration) tumor outline (solid line) and the 3D OFM mapped (inspiration) tumor contour from (C) (dotted line).

Interestingly, the superior aspect of the tumor does not appear to move to the same degree as the inferior tumor aspect. The average tumor displacement at each *z*-location is shown in Figure 8.3; the non-uniform displacement of the tumor is apparent. The tumor volume and surface displacements have similar minima and

maxima. The tumor volume displacement histogram is smoother than the tumor surface displacement histogram which results from the number of voxels in each, respectively.

8.3.2 Lung Tumor Motion

A lung cancer case, in which a clinically acquired inhalation and exhalation BH CT image set had been previously obtained for clinical use in the patient's radiation therapy treatment planning, was chosen for this study. A sagittal view CT image through the tumor center, with the patient at expiration, and the physician-contoured tumor boundary are shown on the left panel in Figure 8.4.

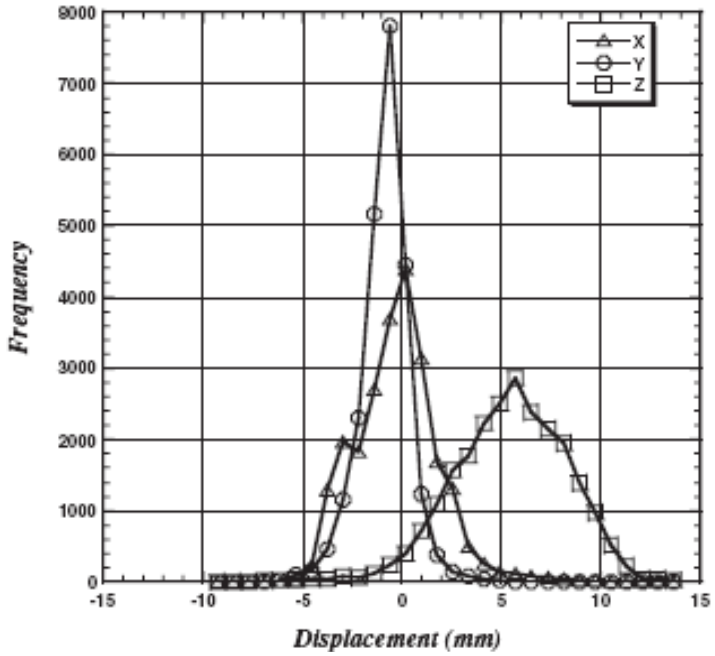

Figure 8.2: Histogram of esophageal tumor displacement for each component of motion (x = right to left, y = anterior to posterior, z = superior to inferior) obtained for the entire image volume.

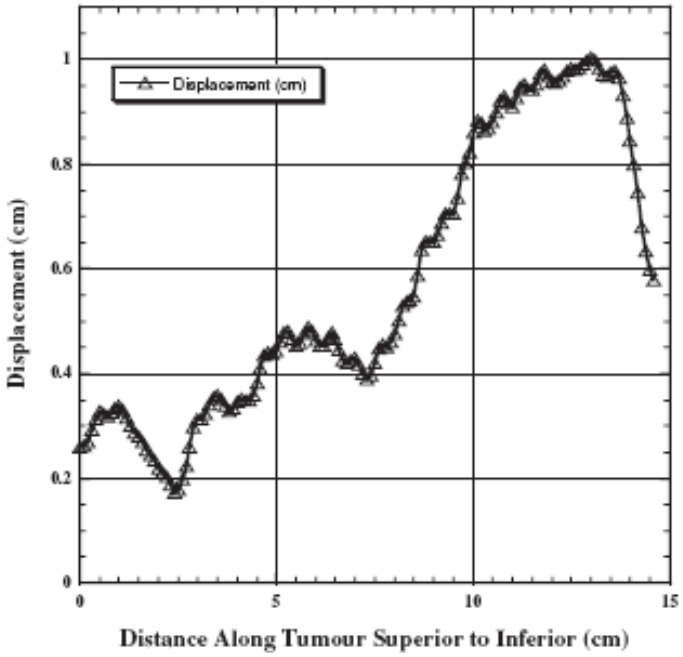

Figure 8.3: Graph of the average esophageal tumor displacement magnitude versus position along the tumor from superior to inferior.

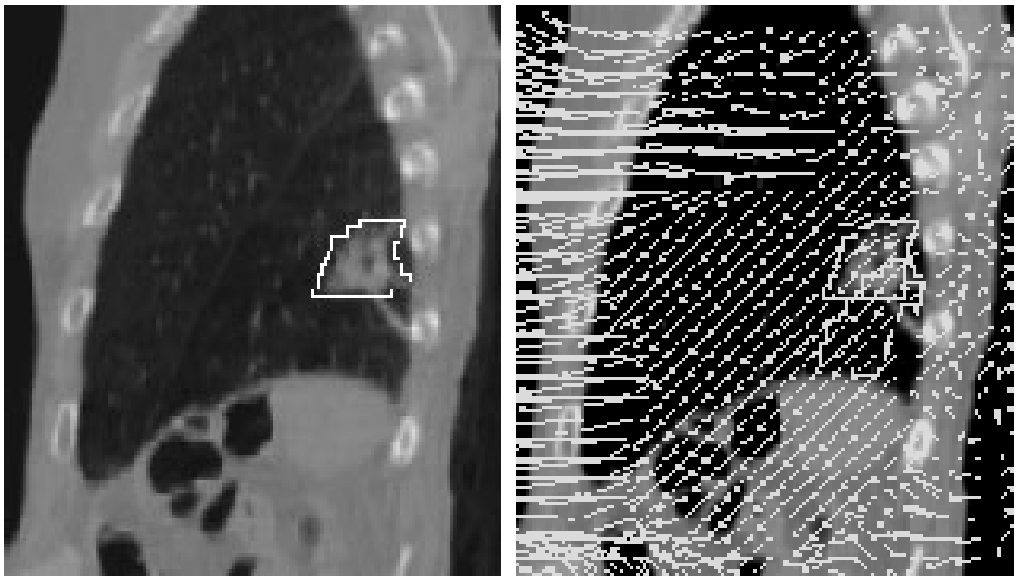

(A) **(B)**

Figure 8.4: (A) An expiration BH CT sagittal image of a lung tumor with the physician-contoured tumour outline (solid line). (B) The same expiration CT image with the tumour contours and the 3D OFM displacement vectors superimposed.

The 3D OFM algorithm was applied to the image volume data to perform registration of the inhalation BH CT images with the expiration BH CT images. The resulting displacement vectors, from the exhalation and inhalation images, are shown

in projection in Figure 8.4(B). The displacement vectors are superimposed onto the expiration sagittal image and tumor surface contour. The tumor content was then mapped from the expiration CT volume to the inspiration CT volume using the displacement vectors. The resulting tumor boundary, equivalent to the contour, was automatically determined on the inspiration CT images. In Figure 8.5(B), the sagittal image is shown with the mapped tumor boundary superimposed. The internal target volume can be determined from the sum of the expiration and inspiration tumor boundaries, shown together in Figure 8.5(C) superimposed on the expiration CT image.

The displacement field, utilized to map the tumor content from the expiration CT image volume to the inspiration CT image volume, contains the tumor motion information in vector format. A histogram was formed from the displacement field of the tumor volume voxels versus displacement for each coordinate direction and is shown in Figure 8.6. The physician drawn contour for the lung tumor on the expiration CT images consists of 1266 points. A histogram of the displacement of these points was generated and is given in Figure 8.7. The smoother appearance of the lung tumor displacement histogram versus the lung contour (or surface) is likely due to the number of points involved. The tumor consists of 16422 voxels versus 1266 points for the tumor surface contour. The location of the tumor surface points, some within the tumor and some in adjacent tissue, may also have some effect. The lung tumor surface and volume moved up to 3.0 cm. The largest displacement occurred in the superior–inferior dimension. The tumour motion was non-uniform with significant tumor distortion apparent from the CT image.

8.4 Discussion

Respiratory induced tumor motion is the largest intrafractional target motion in

radiation therapy and has become an active area of research. Past studies of tumor motion have estimated the motion from manually drawn contours [6, 8, 31] reporting the changes of a bounding box enclosing the tumour boundary or the motion of the center of mass. These studies were limited by a lack of point-to-point correlation. Alternatively, fiducial-based tumor motion studies required that the patient undergo a procedure to implant a radio-opaque fiducial marker into the tumor [5, 7]. The number of points tracked was limited to the number of fiducials. In this study, a new paradigm for tumor motion analysis was introduced. A displacement vector map was calculated using 3D OFM and was used to map a delineated tumor from one CT image volume to the next.

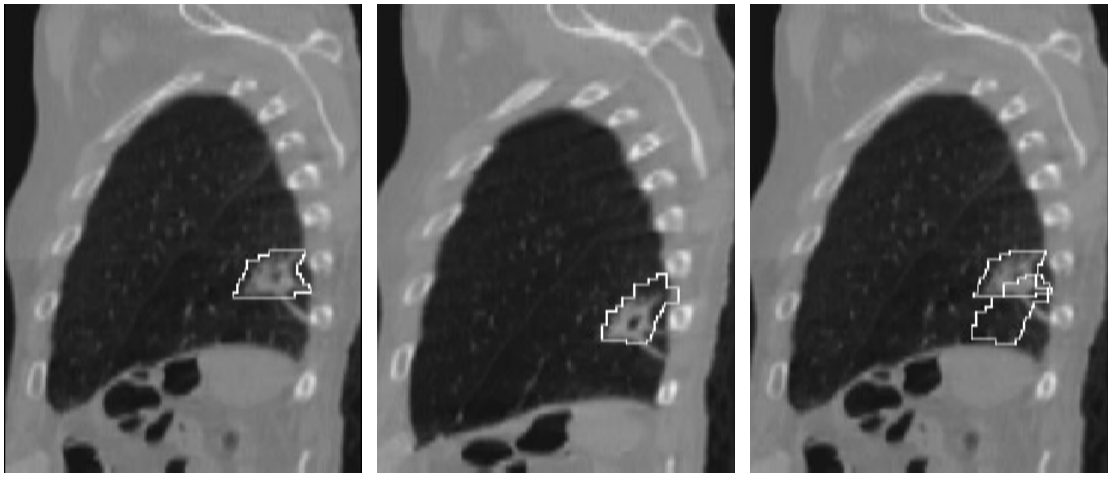

(A) **(B)** **(C)**

Figure 8.5: (A) The expiration BH sagittal CT lung tumor image with the physician-contoured tumor outline. (B) The inspiration BH sagittal CT image with superimposed 3D OFM mapped tumor contour. (C) The expiration BH sagittal CT image with both contours superimposed.

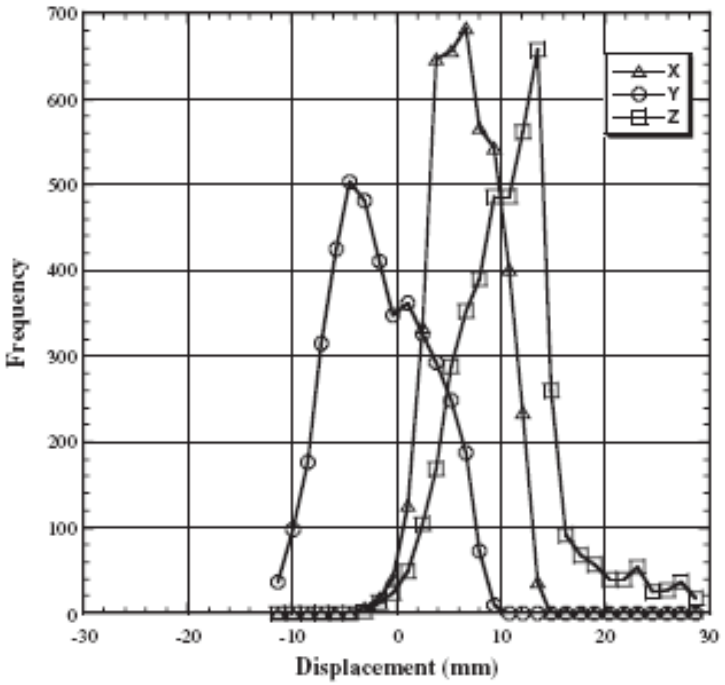

Figure 8.6: Histogram of lung tumor displacement vector components for each voxel contained in the physician-outlined tumor volume.

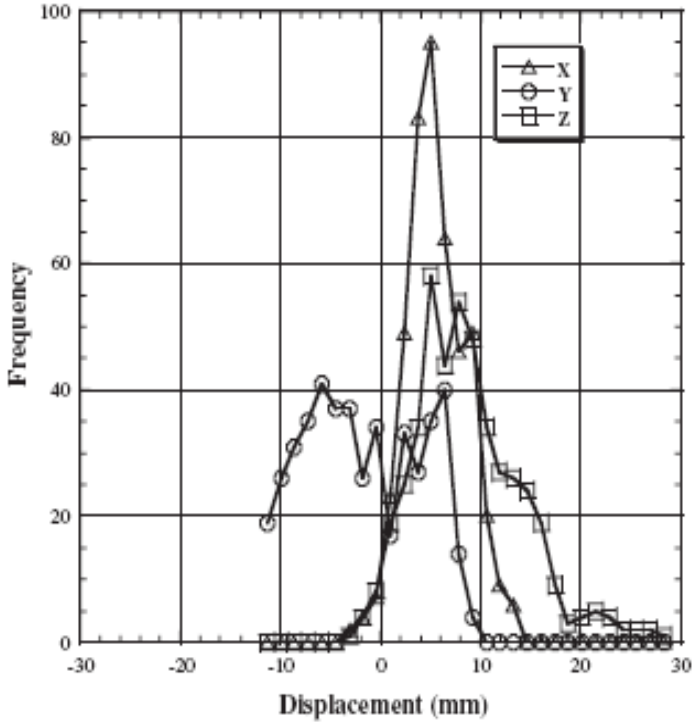

Figure 8.7: Histogram of lung tumor displacement vector components for each point from the physician-outlined contour. This is the tumor surface displacement histogram.

The 3D OFM algorithm performs the calculation based on image content, in

which no user intervention is required. This paradigm can be applied to pairs of BH CT image volumes or 4D CT image sets equally well. We have demonstrated, using the RPC thoracic phantom and simulated patient motion, that the spatial accuracy of the algorithm in the ideal setting is less than the voxel dimension. The error determined was much lower for the lung tumor case than for the esophagus tumor case. Note that the calculations of the displacement are based on the local image gradients, equation, hence the error is related to the local image gradient. The lung tumor boundary contained a much higher image gradient than the esophageal tumor, and the error observed was much lower for the lung tumor than for the esophageal tumor. In both cases the error was small. 3D OFM may have a significant role in both radiation therapy treatment planning and in tumor motion kinematic studies.

One method described to account for respiratory motion in radiation therapy treatment planning involves obtaining an accurate assessment of the tumor trajectory with BH CT imaging at end inspiration and at end expiration. In contrast, freebreathing (FB) CT imaging is presently used as the standard method for radiation therapy treatment planning. Using BH CT imaging to determine the ITV, the tumor location is identified on each scan by manual delineation performed by the radiation oncologist on each of the CT images volumes separately; the inspiration BH, expiration BH, fast FB and slow FB CT image volumes. Note that prior to combining the delineated gross tumor volumes, an 8mm expansion margin for microscopic extension of the tumor [4] is applied. The potential for error in repeated delineation of an identical target is well described [10]. In Guerrero *et al*'s [81] descriptions of this technique for internal target delineation, the resulting tumor motion is described on the basis of the displacement of the centroid or by a bounding box encompassing the tumor contours. With this methodology, there is no point-to-point correspondence between the tumor content between each CT image volume. The lack of correlation

with patient parameters may reflect an oversimplification of the tumor motion description using these techniques.

In this study, we demonstrated a true point-to-point deformable image registration process with the 3D OFM algorithm. The resulting displacement vectors, one for each voxel, relate the tumor location on expiration BH CT to the inspiration BH CT image volume. In addition, the automatic nature of the registration process reduced the physician workload from contouring multiple image volumes to only a single image volume. A limitation of using only the BH CT images to determine the target volume is that tumor trajectory motion often exhibits hysteresis, following two different paths during inhalation and exhalation [26, 82]. This concern is addressed by including a slowly acquired CT scan, for which each image is acquired over 4 seconds allowing the tumor to move through a complete respiratory cycle. 3D OFM can similarly be applied to map the tumor content from contours drawn on a single BH CT (e.g., end expiration), to the other BH CT and a slow CT. The 3D OFM algorithm can be applied to map the tumour boundary, providing tumor targeting information for BH CT images as shown in this study or across an entire 4D CT data set, which consists of ten or more 3D CT image volumes [9]. A study demonstrating the performance of the 3D OFM with measured 4D CT data is in progress. The advantage of 3D OFM is that this method characterizes tumor motion results from the completeness of the motion description when compared with present techniques. In addition to boundary delineation, the 3D OFM computes the resulting displacement vectors for each tumor voxel providing a complete kinematic description of the tumor motion.

This is the first report of esophageal tumor motion due to respiration in the radiation oncology literature. Esophageal motion due to respiration has been previously measured directly. Welch measured esophageal motion in 20 normal

volunteers and found 0.6 ± 0.2 cm axial motion in the abdominal portion and 0.4 ± 0.1 cm movement in the thoracic portion [83]. We found, in the one esophageal tumor studied, that the tumor moved significantly and nonuniformly with greater motion at the gastro-esophageal junction. The maximum displacement was 1.4 cm at the inferior portion of the tumor. Further investigation of esophageal motion and esophageal tumor motion is warranted.

8.5 Conclusions

In this study, a new paradigm for tumor motion analysis is introduced: the calculation of a displacement vector for each tumor voxel. 3D OFM was shown to provide an accurate estimation of intrathoracic tumor motion in phantom studies. Tumor surface and volume histograms reveal a nonuniform motion and suggest that tumor distortion occurs. The tumor surface histogram is more prone to noise related to the location of contour points and their fewer numbers. Surprisingly, esophageal tumor motion was large and nonuniform.

Bibliography

1. Bortfeld T and Chen G T, *Introduction: intrafractional organ motion and its management.* Seminars in Radiation Oncology, 2004. **14** 1.
2. Caldwell C B, Mah K, Skinner M and Danjoux C E, *Can PET provide the 3D extent of tumor motion for individualized internal target volumes? A phantom study of the limitations of CT and the promise of PET*. International Journal of Radiation Oncology, Biology, Physics**,** 2003. **55** 1381–93.
3. Chen Q S, Weinhous M S, Deibel F C, Ciezki J P and Macklis R M, *Fluoroscopic study of tumor motion due to breathing: facilitating precise radiation therapy for lung cancer patients*. Medical Physics, 2001. **28** 1850–6.
4. Giraud P., *Evaluation of microscopic tumor extension in non-small-cell lung cancer for three-dimensional conformal radiotherapy planning*. International Journal of Radiation Oncology, Biology, Physics, 2000. **48** 1015–24.
5. Seppenwoolde Y, Shirato H, Kitamura K, Shimizu S, van Herk M, Lebesque J V and Miyasaka K, *Precise and real-timemeasurement of 3Dtumor motion in lung due to breathing and heartbeat, measured during radiotherapy.* International Journal of Radiation Oncology, Biology, Physics, 2002. **53** 822–34.
6. Shirato H *et al*, *Four-dimensional treatment planning and fluoroscopic real-time tumor tracking radiotherapy for moving tumor*. International Journal of Radiation Oncology, Biology, Physics, 2000. **48** 435–42.
7. Stevens C W, Munden R F, Forster K M, Kelly J F, Liao Z, Starkschall G, Tucker S and Komaki R, *Respiratory-driven lung tumor motion is independent of tumor size, tumor location, and pulmonary function.* International Journal of Radiation Oncology, Biology, Physics, 2001. **51(1)** 62–8.
8. van Sornsen de Koste J R, Lagerwaard F J, Schuchhard-Schipper R H, Nijssen-Visser M R, Voet P W, Oei S S and Senan S, *Dosimetric consequences of tumor mobility in radiotherapy of stage I non-small cell lung cancer–an analysis of data generated using 'slow' CT scans*. Radiotherapy and Oncology 2001. **61(1)** 93–99.
9. Keall P J, Starkschall G, Shukla H, Forster K M, Ortiz V, Stevens C, Vedam S S, George R, Guerrero T M and Mohan R, *Acquiring 4D thoracic CT scans using a multislice helical method.* Physics in Medicine and Biology, 2004. **49** 2053–67.
10. Collier D C, Burnett S S, AminM, Bilton S, Brooks C, Ryan A, Roniger D, Tran D and Starkschall G, *Assessment of consistency in contouring of normal-tissue anatomic structures.* Journal of Applied Clinical Medical Physics, 2003.**4** 17–24.

11. Senan S, van Sornsen de Koste J, Samson M, Tankink H, Jansen P, Nowak P J, Krol A D, Schmitz P and Lagerwaard F J., *Evaluation of a target contouring protocol for 3D conformal radiotherapy in non-small cell lung cancer.* Radiotherapy and Oncology, 1999. **53**(3) 247–255.
12. Horn B K P and Schunck B G, *Determining optical flow*. Artif. Intel., 1981. **17** 185–203.
13. Tsai, Y.C., et al., *Thin-Plate Spline Technique for Medical Image Deformation.* Journal of Medical and Biological Engineering, 2000. **20**(4): p. 203-210.
14. Lin, K.P. and S.C. Huang. *Elastic Mapping Technique for Inter-subject Tomographic Image Registration.* The International Society for Optical Enginerring (SPIE), Visual Communication and Image Processing. 1995.
15. Bookstein, F.L., *Principal Warps: Thin-plate Splines and the Decomposition of Deformations.* IEEE Transactions on Pattern Analysis and Machine Intelligence, 1989. **11**(6): p. 567-585.
16. Segars, W.P. and B.M.W. Tsui, *Study of the efficacy of respiratory gating in myocardia SPECT using the new 4-D NCAT phantom.* IEEE Transactions on Nuclear Science, 2002. **49**(3 Part 1): p. 675-679.
17. Cherry C P D, Followill D S and HansonWF, *Design of a heterogeneous thorax phantom for remote verification of three-dimensional conformal radiotherapy*. Med. Phys., 2000, **27**.
18. Ullman, S., *The interpretation of visual motion*. 1979, Cambridge, MA: MIT Press.
19. Beauchemin, S.S. and J.L. Barron, *The computation of optical flow.* ACM Computing Surveys, 1995. **27**(5): p. 433 – 466.--78
20. Jiang, S. B., Pope, C., Al Jarrah, K. M., Kung, J. H., Bortfeld, T. and Chen, G. T. *An experimental investigation on intra-fractional organ motion effects in lung IMRT treatment*s. Phys. Med. Biol. 48(12), 1773–1784 (2003).
21. Bortfeld, T., Jokivarsi, K., Goitein, M., Kung, J. and Jiang, S. B., *Effects of intra-fraction motion on IMRT dose delivery: statistical analysis and simulation.* Phys. Med. Biol. 47(13), 2203–2220 (2002).
22. Giraud, P. et al., *Conformal radiotherapy (CRT) planning for lung cancer: analysis of intrathoracic organ motion during extreme phases of breathing.* Int. J. Radiat. Oncol. Biol. Phys. 51(4), 1081–1092 (2001).
23. Keall, P. J., Beckham, W. A., Booth, J. T., Zavgorodni, S. F. and Oppelaar, M., *A method to predict the effect of organ motion and set-up variations on treatment plans.* Australasian Phys. Eng. Sci. Med. 22(2), 48–52 (1999).
24. Killoran, J. H., Kooy, H. M., Gladstone, D. J., Welte, F. J. and Beard, C. J. *A numerical simulation of organ motion and daily setup uncertainties: implications*

for radiation therapy. Int. J. Radiat. Oncol. Biol. Phys. 37(1), 213–221 (1997).

25. Mageras, G. S., Kutcher, G. J., Leibel, S. A., Zelefsky, M. J., Melian, E., Mohan, R. and Fuks, Z. *A method of incorporating organ motion uncertainties into three-dimensional conformal treatment plans.* Int. J. Radiat. Oncol. Biol. Phys. 35(2), 333–342 (1996).
26. Shirato, H., Seppenwoolde, Y., Kitamura, K., Onimura, R. and Shimizu, S., *Intrafractional tumour motion: lung and liver.* Semin. Radiat. Oncol. 14(1), 10–18 (2004).
27. Lujan, A. E., Larsen, E. W., Balter, J. M. and Ten Haken, R. K., *A method for incorporating organ motion due to breathing into 3D dose calculations.* Med. Phys. 26(5), 715–720 (1999).
28. Bortfeld, T., van Herk, M., Jiang, S. B., Jokivarsi, K., Goitein, M. and Kung, J. *When should systematic patient positioning errors in radiotherapy be corrected? Effects of intra-fraction motion on IMRT dose delivery: statistical analysis and simulation.* Phys. Med. Biol. 47(23), 7 (2002).
29. Vedam, S. S., Keall, P. J., Kini, V. R., Mostafavi, H., Shukla, H. P. and Mohan, R., *Acquiring a fourdimensional computed tomography dataset using an external respiratory signal.* Phys. Med. Biol. 48(1), 45–62 (2003).
30. McShan, D. L., Lynn, K., Vineberg, K. and Fraass, B., *Radiotherapy plan optimization accounting for set-up and motion uncertainty using a multiple instance geometry approximation.* Med. Phys. 29:1257 (2002).
31. International Commission on Radiation Units and Measurements. *Prescribing, recording, and reporting photon beam therapy.* ICRU Report 50 (Washington, DC: ICRU) (1993).
32. International Commission on Radiation Units and Measurements. *Prescribing, recording, and reporting photon beam therapy.* ICRU Report 62 (Supplement to ICRU Report 50). (Washington, DC: ICRU) (1999).
33. Mackie, T. R., Scrimger, J. W. and Battista, J. J., *A convolution method of calculating dose for 15-MV x rays.* Med. Phys. 12(2), 188–196 (1985).
34. Yu, C.X., Jaffray, D.A., Wong, J.W., *The effects of intra-fraction organ motion on the delivery of dynamic intensity modulation.* Phys. Med. Bio., **43**, 91-104 1998.
35. Kubo, H.D., Hill, B.C., *Respiration gated radiotherapy treatment: A technical study.* Phys Med Biol, 1996. **41**, 83-91.
36. Wong, J.W., *et. al*., *The use of active breathing control (ABC) to reduce margin for breathing motion.* Int J Radiat Oncol Biol Phys, 1999. **44**, 911-919.
37. Karger CP, Jäkel O, Debus J, *et al. Three-dimensional accuracy and interfractional reproducibility of patient fixation and positioning using a*

stereotactic head mask system. Int J Radiat Oncol Biol Phys **49**, 1493-1504, 2001.

38. Yan, D., Jaffray D.A. and Wong J.W., *A model to accumulate fractionated dose in deforming organ.* Int J Radiat Oncol Biol Phys, 1999. **44**, 665-675.
39. Brock, K.K., *et. al*., *Inclusion of organ deformation in dose calculations*. Med Phys., 2003. **30** 290-295.
40. Christensen, G.E., *et. al*., *Image-based dose planning of intracavitary brachytherapy: registration of serial imaging studies using deformable anatomic templates.* Int J Radiat Oncol Biol Phys**,** 2001. **51**, 227-243.
41. Schaly, B., Bauman, G.S., Battista, J.J., Van Dyk, J., *Validation of contour-driven thin-plate splines for tracking fraction-to-fraction changes in anatomy and radiation therapy dose mapping.* Phys Med Biol, 2005. **50**, 459-475.
42. Maes F., Collignon A., Vandermeulen D., Marchal G. and Suetens P., *Multi-Modality Image Registration by Maximization of Mutual Information.* IEEE Proceeding of MMBIA, 1996. 14-22.
43. Gharavi H. and Mills M., *Block-matching motion estimation algorithms: New results.* IEEE Trans. Circ. And Syst., 1990. **37**, 649-651.
44. Lee, H.K., et al., *Postoperative pulmonary complications after preoperative chemoradiation for esophageal carcinoma: correlation with pulmonary dose-volume histogram parameters*1*. International Journal of Radiation Oncology Biology Physics, 2003. **57**: p. 1317-1322
45. Kwa, S.L., et al., *Radiation pneumonitis as a function of mean lung dose: an analysis of pooled data of 540 patients.* International Journal of Radiation Oncology, Biology, Physics, 1998. **42**(1): p. 1-9.
46. Graham, M.V., et al., *Clinical dose-volume histogram analysis for pneumonitis after 3D treatment for non-small cell lung cancer (NSCLC).* International Journal of Radiation Oncology, Biology, Physics, 1999. **45**(2): p. 323-9.
47. Tsujino, K., et al., *Predictive value of dose-volume histogram parameters for predicting radiation pneumonitis after concurrent chemoradiation for lung cancer.* International Journal of Radiation Oncology, Biology, Physics, 2003. **55**(1): p. 110-5.
48. Gopal, R., et al., *The relationship between local dose and loss of function for irradiated lung.* International Journal of Radiation Oncology, Biology, Physics, 2003. **56**(1): p. 106-13.
49. Levinson, B., et al., *Regional dose response to pulmonary irradiation using a manual method.* Radiotherapy & Oncology, 1998. **48**(1): p. 53-60.
50. Geara, F.B., et al., *Factors influencing the development of lung fibrosis after chemoradiation for small cell carcinoma of the lung: evidence for inherent*

interindividual variation. International Journal of Radiation Oncology, Biology, Physics, 1998. **41**(2): p. 279-86.

51. Marks, L.B., et al., *Quantification of radiation-induced regional lung injury with perfusion imaging.* International Journal of Radiation Oncology, Biology, Physics, 1997. **38**(2): p. 399-409.
52. Fan, M., et al., *Can we predict radiation-induced changes in pulmonary function based on the sum of predicted regional dysfunction?* Journal of Clinical Oncology, 2001. **19**(2): p. 543-50.
53. Garipagaoglu, M., et al., *The effect of patient-specific factors on radiation-induced regional lung injury.* International Journal of Radiation Oncology, Biology, Physics, 1999. **45**(2): p. 331-8.
54. Marks, L.B., et al., *Radiation-induced pulmonary injury: symptomatic versus subclinical endpoints.* International Journal of Radiation Biology, 2000. **76**(4): p. 469-75.
55. Marks, L.B., et al., *The utility of SPECT lung perfusion scans in minimizing and assessing the physiologic consequences of thoracic irradiation.* International Journal of Radiation Oncology, Biology, Physics, 1993. **26**(4): p. 659-68.
56. Marks, L.B., et al., *The role of three dimensional functional lung imaging in radiation treatment planning: the functional dose-volume histogram.* International Journal of Radiation Oncology, Biology, Physics, 1995. **33**(1): p. 65-75.
57. Kwa, S.L.S., et al., *Application of chamfer matching in three-dimensional correlation of CT-SPECT and CT-CT of the lungs.* Radiotherapy and Oncology, 1995. **37**(Supplement): p. S3-S67.
58. Theuwsa, J.C.M., et al., *Dose–effect relations for early local pulmonary injury after irradiation for malignant lymphoma and breast cancer.* Radiotherapy and Oncology, 1998. **48**(1): p. 33-43.
59. Tai, Y.C., et al., *Utilization of 3D Elastic Transformation in the Registration of Chest X-ray CT and Whole Body PET.* IEEE Transactions on Nuclear Science, 1997. **44**(4): p. 1555 - 1562.
60. Song, S.M. and R.M. Leahy, *Computation of 3-D velocity fields from 3-D cine CT images of a human heart.* IEEE Transaction on Medical Imaging, 1991. **10**(1): p. 295-306.
61. Gorce, J.M., D. Friboulet, and I.E. Magnin, *Estimation of three-dimensional cardiac velocity fields: assessment of a differential method and application to three-dimensional CT data.* Medical Image Analysis, 1997. **1**(3): p. 245-61.
62. Guerrero, T.M., et al., *Characterization of a Whole Body Imaging Technique for PET.* IEEE Transactions on Nuclear Science, 1990. **37**(2): p. 676 - 680.

63. Dahlbom, M., et al., *Whole-body positron emission tomography: Part I. Methods and performance characteristics.* J Nucl Med, 1992. **33**(6): p. 1191-9.
64. Hawkins, R.A., C.K. Hoh, and M. Dahlbom, *Whole-body PET finds promising clinical niche.* Diagn Imaging (San Franc), 1992. **14**(6): p. 88-91, 121.
65. Hoh, C.K., et al., *Cancer detection with whole-body PET using 2-[18F]fluoro-2-deoxy-D-glucose.* J Comput Assist Tomogr, 1993. **17**(4): p. 582-9.
66. Akhurst, T., et al., *An initial experience with FDG-PET in the imaging of residual disease after induction therapy for lung cancer.* Annals of Thoracic Surgery., 2002. **73**(1): p. 259-64; discussion 264-6.
67. Inoue, T., et al., *Detecting recurrent or residual lung cancer with FDG-PET.* Journal of Nuclear Medicine, 1995. **36**(5): p. 788-93.
68. Carretta, A., et al., *18-FDG positron emission tomography in the evaluation of malignant pleural diseases - a pilot study.* European Journal of Cardio-Thoracic Surgery, 2000. **17**(4): p. 377-83.
69. Cabrera Villegas, A., A. Canovas Fernandez, and J.C. Martin Urreta, *[Post-radiation pneumonitis in a case of Hodgkin's lymphoma assessed with PET-FDG by residual mediastinal mass].* Rev Esp Med Nucl, 2000. **19**(4): p. 288-92.
70. Lin, P., et al., *Fluorine-18 FDG dual-head gamma camera coincidence imaging of radiation pneumonitis.* Clin Nucl Med, 2000. **25**(11): p. 866-9.
71. Lowe, V.J., et al., *Serial Evaluation of Increased Chest Wall F-18 Fluorodeoxyglucose (FDG) Uptake Following Radiation Therapy in Patients With Bronchogenic Carcinoma.* Clin Positron Imaging, 1998. **1**(3): p. 185-191.
72. Ajani, J.A., et al., *A three-step strategy of induction chemotherapy then chemoradiation followed by surgery in patients with potentially resectable carcinoma of the esophagus or gastroesophageal junction.* Cancer, 2001. **92**(2): p. 279-86.
73. Mackie, T.R., J.W. Scrimger, and J.J. Battista, *A convolution method of calculating dose for 15-MV x rays.* Medical Physics, 1985. **12**(2): p. 188-96.---34
74. Ahamad, A., et al., *Intensity-modulated radiation therapy: a novel approach to the management of malignant pleural mesothelioma.* International Journal of Radiation Oncology, Biology, Physics, 2003. **55**(3): p. 768-75.
75. Pi-Chih Wang, *Fourier descriptor analysis and medical image application*, Thesis 1999, CYCU, Taipei.
76. C. Zahn and R. Roskies, *Fourier descriptors for plane closed curves*, IEEE Trans. Comput. Vol. 21, no. 3, 269-281, 1972
77. Burnett SSC, Starkschall G, Stevens CW, Liao Z., *A deformable-model approach*

to semi-automatic segmentation of CT images demonstrated by application to the spinal canal. Med Phys, 2004; 31:251-263.

78. Machie, T.R., *et. al*., *Image guidance for precise conformal radiotherapy.* Int J Radiat Oncol Biol Phys**,** 2003, **56**, 89-105.
79. Keall, P.J., Starkschall, G., Shukla, H., Forster, K.M., Ortiz, V., Stevens, C., Vedam, S.S., George, R., Guerrero, T., Mohan, R., *Acquiring 4D thoracic CT scans using a multislice helical method.* Phys Med Biol., 2003.
80. Armstrong, J.G., et al., *Three-dimensional conformal radiation therapy may improve the therapeutic ratio of high dose radiation therapy for lung cancer.* International Journal of Radiation Oncology, Biology, Physics, 1993. **26**(4): p. 685-9
81. Guerrero T M *et al*., *Target definition in non-small cell lung cancer*. Intensity Modulated Radiation Therapy: A Clinical Perspective ed A J Mundt and J C Roeske (Toronto, BC: Decker). 2004
82. Murphy M J., *Tracking moving organs in real time.* Semin. Radiat. Oncol., 2004. **14** 91–100
83. Welch R W and Gray J E., *Influence of respiration on recordings of lower oesophageal sphincter pressure in humans.* Gastroenterology, 1982. **83** 590–4

VITAE

Tzung-Chi Huang was born in Tainan, Taiwan, on June 19, 1979, the son of Wen-Kuang Huang and Fu-Mei Hsieh. After completing his study at Shahua High School, Tainan, Taiwan, he entered Chung Yuan University at Chung Li, Taiwan. From 1998-2002 he attended the Chung Yuan University. He received the degree of Bachelor of Science with a major in Electrical Engineering in June, 2002. He entered the Graduate School of Chung Yuan University and finished all required courses in June, 2003. During the following year he was recruited as a graduate exchange student at MD Anderson Cancer Center, Houston, Texas. In January, 2005 he entered the Graduate School of Biomedical Sciences at the University of Texas Southwestern Medical Center at Dallas. He was awarded the degree of Doctor of Philosophy in Science in May, 2007.

Permanent Address: No.464, Baosi, Anding Township, Tainan County 745, Taiwan

VITAE

Tzung-Chi Huang was born in Tainan, Taiwan, on June 19, 1979, the son of Wen-Kuang Huang and Fu-Mei Hsieh. After completing his study at Shahua High School, Tainan, Taiwan, he entered Chung Yuan University at Chung Li, Taiwan. From 1998-2002 he attended the Chung Yuan University. He received the degree of Bachelor of Science with a major in Electrical Engineering in June, 2002. He entered the Graduate School of Chung Yuan University and finished all required courses in June, 2003. During the following year he was recruited as a graduate exchange student at MD Anderson Cancer Center, Houston, Texas. In January, 2005 he entered the Graduate School of Biomedical Sciences at the University of Texas Southwestern Medical Center at Dallas. He was awarded the degree of Doctor of Philosophy in Science in May, 2007.

Permanent Address: No.464, Baosi, Anding Township, Tainan County 745, Taiwan